

University of Windsor

Scholarship at UWindor

Electronic Theses and Dissertations

Theses, Dissertations, and Major Papers

1-31-2023

Approaches for Improving Overall System Efficiency in Wound Field Synchronous Machine Drives used for EV Propulsion

Vamsi Krishna Kurramsetty
University of Windsor

Follow this and additional works at: <https://scholar.uwindsor.ca/etd>



Part of the [Electrical and Computer Engineering Commons](#), and the [Other Operations Research, Systems Engineering and Industrial Engineering Commons](#)

Recommended Citation

Kurramsetty, Vamsi Krishna, "Approaches for Improving Overall System Efficiency in Wound Field Synchronous Machine Drives used for EV Propulsion" (2023). *Electronic Theses and Dissertations*. 8968. <https://scholar.uwindsor.ca/etd/8968>

This online database contains the full-text of PhD dissertations and Masters' theses of University of Windsor students from 1954 forward. These documents are made available for personal study and research purposes only, in accordance with the Canadian Copyright Act and the Creative Commons license—CC BY-NC-ND (Attribution, Non-Commercial, No Derivative Works). Under this license, works must always be attributed to the copyright holder (original author), cannot be used for any commercial purposes, and may not be altered. Any other use would require the permission of the copyright holder. Students may inquire about withdrawing their dissertation and/or thesis from this database. For additional inquiries, please contact the repository administrator via email (scholarship@uwindsor.ca) or by telephone at 519-253-3000ext. 3208.

Approaches for Improving Overall System Efficiency in Wound Field Synchronous Machine Drives used for EV Propulsion

By

Vamsi Krishna Kurramsetty

A Thesis
Submitted to the Faculty of Graduate Studies
through the Department of Electrical and Computer Engineering
in Partial Fulfillment of the Requirements for
the Degree of Master of Applied Science
at the University of Windsor

Windsor, Ontario, Canada
© 2023, Vamsi Krishna Kurramsetty

Approaches for Improving Overall System Efficiency in Wound Field Synchronous Machine Drives used for EV Propulsion

by

Vamsi Krishna Kurramsetty

APPROVED BY:

M. Etemadi
Department of Mechanical, Automotive & Materials Engineering

B. Balasingam
Department of Electrical and Computer Engineering

K. L. V. Iyer, Co-Advisor
Department of Electrical and Computer Engineering

N. C. Kar, Co-Advisor
Department of Electrical and Computer Engineering

January 13, 2023

DECLARATION OF CO–AUTHORSHIP/PREVIOUS PUBLICATIONS

I. Co–Authorship

I hereby declare that this thesis incorporates material that is the result of joint research, as follows: This thesis includes the outcome of publications which also have co-authors who are/were graduate students or post-doctoral fellows supervised by Dr. Narayan Kar. In all cases, only the primary contributions of the author towards these publications are included in this thesis. The contribution of co–authors was primarily through the provision of assistance in experimentation and analysis.

I am aware of the University of Windsor Senate Policy on Authorship, and I certify that I have properly acknowledged the contribution of other researchers on my thesis and have obtained written permission from each of the co–author(s) to include the above material(s) in my thesis. I certify that, with the above qualification, this thesis, and the research to which it refers, is the product of my own work.

II. Previous Publications

This thesis includes selected sections and extended work of research that have been published/submitted for publication in peer-reviewed IEEE International Conferences, as follows:

| Thesis Chapter | Publication Title/Full Citation | Publication Status |
|-----------------------|--|---|
| <i>Chapter</i> 5 | V. K. Kurramsetty , P. Korta, K. L. V. Iyer, N. C. Kar, and S. Mukundan, “Doubly Excited Synchronous Machine System with Variable Torque-Speed Efficiency Characteristics,” U.S Provisional Patent Application No. 63/423,175, November 2022. | <i>Filed U.S Provisional Patent</i> |

I certify that I have obtained written permission from the copyright owners to include the above published materials in my thesis. I certify that the above material describes work completed during my registration as a graduate student at the University of Windsor.

III. General

I declare that, to the best of my knowledge, my thesis does not infringe upon anyone's copyright nor violate any proprietary rights and that any ideas, techniques, quotations, or any other material from the work of other people included in my thesis, published or otherwise, are fully acknowledged in accordance with the standard referencing practices. Furthermore, to the extent that I have included copyrighted material that surpasses the bounds of fair dealing within the meaning of the Canada Copyright Act and has included copies of such copyright clearances to the appendix of this thesis.

I declare that this is a true copy of my thesis, including any final revisions, as approved by my thesis committee and the Graduate Studies office, and that this thesis has not been submitted for a higher degree to any other University or Institution.

ABSTRACT

In recent years, electric vehicle technologies have evolved rapidly, speeding the transition from internal combustion engine (ICE) vehicles to electric vehicles (EV). With the exponential growth in electric vehicle sales, demand for electric powertrains with higher torque density, higher drive cycle system efficiency, and lower cost has increased. Such a powertrain should lead to increased efficiency, safety, maximum speed, affordability, and driving range of EVs. Addressing these targets, the wound field synchronous machine (WFSM) based powertrain has proven to be a potential candidate for propelling EVs.

Since the WFSM needs a separate rotor excitation system, an inductive power transfer system or a conductive power transfer system using brushes and slip rings could be used. The inductive power transfer (IPT) rotor excitation system has increased loss than the conventional conductive brushed rotor excitation system because of its topology. Therefore, this thesis proposes a maximum overall system efficiency per ampere control for IPT-based WFSMs. The proposed control algorithm improves the overall efficiency by considering WFSM, stator three-phase inverter, and rotor IPT converter losses. The proposed control algorithm is implemented using a proportional-integral controller, and the closed-loop controls are experimentally validated.

This thesis also proposes a novel converter and control topologies for a doubly excited wound field synchronous machine for improving efficiency at lower speeds and torque loads. In the end, an Overall performance comparison between the proposed topologies and finite element analysis simulations for the proposed models are presented.

DEDICATION

Dedicated to my family...

Radha Krishna Rao (Late Grandma),

Mrs. Sri Priya (Mom),

Mr. Venu Gopal (Dad),

Manasa (Achu) (Sister)

*Dedicated to my source of energy - My Gurus and the
Almighty...*

Pratyaksha Guru,

Paroksha Guru,

Paramesthi Guru,

*Almighty God and the force behind this entire
creation and existence*

ACKNOWLEDGEMENTS

First and foremost, I would like to thank the almighty and the force responsible for the entire creation of life for scripting this master's degree journey in my destiny. I would like to extend my gratitude to all my family members: my late grandma, my mother, my father, my sister, all my gurus, and all my well-wishes for all the support, prayers, motivation, encouragement, etc.

I would like to sincerely thank Dr. R. Srikanth, Dr. N. Venkatanathan, Dr. James A. Baskaradas, Dr. J. Jayachandran, and many other faculties at SASTRA University, India, for encouraging and helping me to pursue the Semester Abroad Program (SAP), which brought me to the Centre for Hybrid Automotive Research and Green Energy (CHARGE) Labs, University of Windsor, Canada as a confused and inquisitive intern. I also would like to thank the School of Electrical and Electronics Engineering (SEEE) curriculum and Robotics Club at SASTRA (RCS) for equipping me with the fundamental concepts that greatly helped me during my master's journey.

I would like to thank Dr. Narayan C. Kar, my supervisor, for accepting me first as an intern and later admitting me as a master's candidate at CHARGE Labs. I sincerely thank him for providing me with world-class experimental laboratory facilities and a graduate program of working with industry projects at CHARGE labs. Working at this wonderful laboratory facility during my master's journey, I really had excellent memories, hands-on work satisfaction. Altogether, it made me feel like a real engineer.

I would like to extend my very special thanks to Dr. K. Lakshmi Varaha Iyer, my co-supervisor, for being the best guide and mentor right from day zero. I admire his positivity, team-leading potential, and humbleness. He has been a great pillar of support both in the technical and non-technical aspects during my master's journey. I really owe a major part of my success to him and would again like to thank him for all the opportunities he provided me. Without him, I don't think I would have been at CHARGE labs.

I would also like to extend my gratitude to Dr. Aiswarya Balamurali, Dr. Shruthi Mukundan, Dr. Himavarsha Dhulipati, Animesh Anik, Dr. Ze Li, Soumava Bhattacharjee,

Philip Korta, Dr. Venkata Ratnam Vakacharla, Cameron Pickersgill, Eunha Chu, and many other lab mates and other support staff at CHARGE labs who have been with me and helped me directly or indirectly. I would also like to thank Dr. B. Balasingam and Dr. M. Etemadi for serving on my master's committee panel.

Finally, I would also like to thank all the scientists, mathematicians, inventors, researchers, technicians, and many other great people for bringing science this far. Science might be in a better shape and advancing rapidly today. However, all the fundamental hard work and great sacrifices are made in the past by beautiful minds.

TABLE OF CONTENTS

| | |
|---|-------------|
| DECLARATION OF CO–AUTHORSHIP/PREVIOUS PUBLICATIONS..... | iii |
| ABSTRACT..... | v |
| DEDICATION..... | vi |
| ACKNOWLEDGEMENTS | vii |
| LIST OF TABLES | xii |
| LIST OF FIGURES | xiii |
| LIST OF ABBREVIATIONS..... | xvi |
| CHAPTER 1 INTRODUCTION..... | 1 |
| <i>1.1 Overview of Electric Vehicles</i> | <i>4</i> |
| <i>1.2 Electric Traction Drive Technology</i> | <i>5</i> |
| <i>1.3 Overview of Wound Field Synchronous Machine Drives</i> | <i>7</i> |
| <i>1.4 Motivation and Research Objective</i> | <i>8</i> |
| <i>1.5 Research Contribution</i> | <i>9</i> |
| <i>1.6 Organization of This Thesis</i> | <i>10</i> |
| <i>1.7 Conclusion</i> | <i>10</i> |
| <i>1.8 References</i> | <i>11</i> |
| CHAPTER 2 MODELING AND SIMULATION OF THE WFSM E-DRIVE SYSTEM WITH VARIOUS EXCITATION TECHNIQUES..... | 14 |
| <i>2.1 Introduction</i> | <i>14</i> |
| <i>2.2 Modeling of Wound Field Synchronous Machine</i> | <i>14</i> |
| <i>2.2.1 Reference Frame Theory.....</i> | <i>14</i> |
| <i>2.2.2 Equivalent Circuit Diagram and Mathematical Modeling of WFSM</i> | <i>16</i> |
| <i>2.2.3 Magnetic Saturation and Cross-Coupling Effects</i> | <i>18</i> |
| <i>2.2.4 Loss Modeling of WFSM.....</i> | <i>22</i> |
| <i>2.2.5 Verification of Results with FEA Data.....</i> | <i>23</i> |
| <i>2.3 Modeling of Three-Phase Inverter</i> | <i>24</i> |
| <i>2.3.1 Voltage and Current Characteristics of IGBT and Diode</i> | <i>25</i> |
| <i>2.3.2 Switching Energy Characteristics of IGBT.....</i> | <i>26</i> |
| <i>2.3.3 Inverter Loss Modeling</i> | <i>27</i> |
| <i>2.4 Modeling of Conductive Excitation System</i> | <i>27</i> |

| | |
|--|-----------|
| 2.5 Modeling of Inductive Power Transfer System | 28 |
| 2.6 Conclusion | 30 |
| 2.7 References | 30 |
| CHAPTER 3 MAXIMUM SYSTEM EFFICIENCY PER AMPERE CONTROL OF INDUCTIVE POWER TRANSFER-BASED WFSM E-DRIVE SYSTEM | 34 |
| 3.1 Introduction | 34 |
| 3.2 Design and Modeling of Closed-Loop PI Controllers Using Pole-Zero Cancellation Technique | 34 |
| 3.2.1 Design of PI Controller for Direct Axis | 35 |
| 3.2.2 Design of PI Controller for Quadrature Axis | 37 |
| 3.2.3 Design of PI Controller for Field Axis | 38 |
| 3.3 Design and Modeling of Closed-Loop Controls Based on Feedback | 40 |
| 3.3.1. Design of Closed-Loop Current Control | 41 |
| 3.3.2 Design of Closed-Loop Speed Control | 41 |
| 3.4. Comparison of Conventional Total and Rotor Loss Minimization Control Strategies | 42 |
| 3.5 Maximum System Efficiency Per Ampere Control of IPT-Based WFSM Using Brute-Force Algorithm | 45 |
| 3.5.1 Overall System Loss Model for Efficiency Improvement | 46 |
| 3.5.2 Brute-Force Algorithm and Control Methodology Flowchart | 48 |
| 3.5.3 Comparison of Maximum Overall System Efficiency Per Ampere Algorithm vs Maximum Torque Per Ampere Algorithm | 50 |
| 3.6 Conclusion | 51 |
| 3.7 References | 52 |
| CHAPTER 4 HARDWARE IMPLEMENTATION OF WOUND FIELD SYNCHRONOUS MACHINE CLOSED-LOOP CURRENT CONTROL VALIDATION | 55 |
| 4.1 Introduction | 55 |
| 4.2 Real-Time Embedded Controller | 55 |
| 4.3 Closed-Loop Current Control Hardware Development | 57 |
| 4.3.1 Three-Phase Stator Inverter | 58 |
| 4.3.2 Rotor Buck Converter | 59 |
| 4.3.3 Three-Phase Current Transducers | 60 |
| 4.3.4 Rotor Position Sensor | 62 |

| | |
|--|-----------|
| 4.4 Back EMF Results | 63 |
| 4.5 Closed-Loop Current Control of WFSM on Dynamometer | 66 |
| 4.5.1 Direct Axis Closed-Loop Current Control..... | 66 |
| 4.5.2 Quadrature Axis Closed-Loop Current Control | 67 |
| 4.5.3 Field Axis Closed-Loop Current Control..... | 68 |
| 4.5.4 Observations on Cross-Coupling Effects | 68 |
| 4.6 Validation of Experimental Results..... | 69 |
| 4.6.1 Closed-Loop Control Validation During Transients | 69 |
| 4.6.2 Steady State Load Points Validation..... | 70 |
| 4.7 Conclusion | 71 |
| 4.8 References | 71 |
| CHAPTER 5 NOVEL CONVERTER AND CONTROL TOPOLOGY FOR ENHANCING CONSTANT TORQUE AND POWER REGIONS OF WFSM..... | 74 |
| 5.1 Introduction | 74 |
| 5.2 Modeling of Vehicle Dynamics and Drive Cycle Analysis..... | 74 |
| 5.3 Motivation from ETDs Performance Level..... | 77 |
| 5.4 Doubly Excited Rotor Configuration | 78 |
| 5.5 Proposed Converter Topology..... | 80 |
| 5.5.1 Single-Legged Converter Topology | 80 |
| 5.5.2 Double-Legged Converter Topology | 82 |
| 5.5.3 Overall Performance Analysis Among the Proposed Topologies..... | 83 |
| 5.6 Proposed Control Algorithm and Analysis of Seamless Transfer Between Multiple Torque-Speed Characteristics | 85 |
| 5.6.1 Efficiency Map Generation for Offline Look-Up Tables..... | 85 |
| 5.6.2 Proposed Control Algorithm for Seamless Transfer..... | 87 |
| 5.7 Conclusion | 88 |
| 5.8 Reference | 88 |
| CHAPTER 6 CONCLUSION AND FUTURE WORK..... | 90 |
| 6.1 Conclusion | 90 |
| 6.2 Future Work..... | 91 |
| VITA AUCTORIS | 92 |

LIST OF TABLES

| | | |
|-----------|--|----|
| Table 1.1 | Commercially Available Electric Vehicles..... | 4 |
| Table 4.1 | Validation of Steady State Load Points Between Simulations and Experimental Results..... | 80 |
| Table 5.1 | Ford Fiesta 2014 Model Vehicle Specifications..... | 85 |
| Table 5.2 | Overall Performance Comparison of Converter Topologies and Losses... | 93 |

LIST OF FIGURES

| | |
|---|----|
| Fig. 1.1. Comparison of GHG emissions between ICE and EV. | 1 |
| Fig. 1.2. Electrical vehicle target timelines of strategic OEMs. | 2 |
| Fig. 1.3. New EVs registered by provinces in 2022, Canada. | 3 |
| Fig. 1.4. Electric vehicle powertrain showing various internal components | 6 |
| Fig. 1.5. Torque-speed and power-speed profile of a WFSM. | 6 |
| Fig. 1.6. Schematic diagram of EV powertrain with WFSM as e-motor..... | 7 |
| Fig. 1.7. Block diagram showing power flow in a commercially available PEC stack..... | 8 |
| Fig. 2.1. Park’s transformation. | 15 |
| Fig. 2.2. Equivalent circuit diagram of wound field synchronous machine. (a) d -axis circuit. (b) q -axis circuit. (c) f -axis circuit. | 17 |
| Fig. 2.3. Inductance saturation profile at rated field excitation current. (a) d -axis inductance profile. (b) q -axis inductance profile. (c) Mutual inductance between d and f axes. | 20 |
| Fig. 2.4. Cross-coupling effect includes magnetic saturation. (a) d -axis. (b) q -axis. (c) f - axis. | 21 |
| Fig. 2.5. (a) Torque-speed profile as input to simulation and FEA. (b) difference in torque. | 23 |
| Fig. 2.6. Three-phase two-level voltage source inverter schematic diagram..... | 24 |
| Fig. 2.7. Three-phase two-level voltage source inverter simulations. (a) Three-phase stator phase currents. (b) Three-phase line-to-line voltage..... | 25 |
| Fig. 2.8. Voltage and current characteristics at $V_{GE} = 15V$. (a) IGBT. (b) Diode..... | 25 |
| Fig. 2.9. Switching energy characteristics. (a) E_{ON} of IGBT. (b) E_{OFF} of IGBT. (c) E_{REC} of diode..... | 26 |
| Fig. 2.10. Buck converter for conductive rotor excitation system. (a) Buck converter schematic diagram. (b) Simulation results showing field excitation voltage and current. 28 | 28 |
| Fig. 2.11. Inductive power transfer excitation system. (a) IPT system schematic diagram. (b) Load current. (c) Primary voltage and current. (d) Secondary voltage and current. | 29 |
| Fig. 3.1. Direct axis block diagram in Laplace domain. | 35 |
| Fig. 3.2. Direct axis closed-loop current control block diagram in Laplace domain..... | 35 |
| Fig. 3.3. Quadrature axis block diagram in Laplace domain. | 37 |
| Fig. 3.4. Quadrature axis closed-loop current control block diagram in Laplace domain. | 38 |
| Fig. 3.5. Field axis block diagram in Laplace domain. | 39 |
| Fig. 3.6. Field axis closed-loop current control block diagram in Laplace domain. | 39 |

| | |
|--|----|
| Fig. 3.7. Cascaded control of a motor drive..... | 40 |
| Fig. 3.8. Block diagram of WFSM closed-loop current control. | 41 |
| Fig. 3.9. Block diagram of WFSM closed-loop speed control. | 42 |
| Fig. 3.10. Input torque-speed profile at various stator phase currents..... | 43 |
| Fig. 3.11. Comparison between TLM and RLM control methodologies. (a) Difference in stator phase current. (b) Difference in field current..... | 43 |
| Fig. 3.12. Comparison between TLM and RLM control methodologies. (a) Difference in stator losses. (b) Difference in rotor losses..... | 44 |
| Fig. 3.13. Comparison between TLM and RLM control methodologies in total motor losses..... | 45 |
| Fig. 3.14. Brute-force algorithm for finding i_{dqf} current references towards maximum overall system per ampere of IPT-based WFSM..... | 49 |
| Fig. 3.15. Comparison of direct, quadrature, and field axis current references between MTPA and maximum overall system efficiency methods..... | 50 |
| Fig. 3.16. Comparison of overall system losses between MTPA and maximum overall system efficiency per ampere methods. (a) at 500 rpm. (b) at 1500 rpm. (c) at 2000 rpm. (d) at 2500 rpm..... | 50 |
| Fig. 4.1. Real-time controller architecture | 55 |
| Fig. 4.2. Synchronized real-time simulations computational time profile..... | 56 |
| Fig. 4.3. Block diagram of hardware and software synchronization. | 57 |
| Fig. 4.4. Overall test rig setup for WFSM closed-loop current control. | 58 |
| Fig. 4.5. Stator three-phase inverter connected to motor phase terminals through current transducers | 59 |
| Fig. 4.6. Three-phase inverter operated as a buck converter for WFSM field excitation.. | 60 |
| Fig. 4.7. Closed-loop current transducer block diagram..... | 61 |
| Fig. 4.8. High-accuracy closed-loop current transducers connected through three-phase motor terminals | 61 |
| Fig. 4.9. Three-phase motor phase currents sensed through three-phase current transducers..... | 61 |
| Fig. 4.10. Input excitation signal and output phase shifted sin and cos signals from the variable reluctance resolver | 63 |
| Fig. 4.11. Rotor position sensed though variable reluctance resolver under a constant speed of 100 rpm..... | 63 |
| Fig. 4.12. Measured field excitation circuit PWM voltage and current..... | 64 |
| Fig. 4.13. Generated back EMF line-to-line voltage at a constant speed of 500 rpm at field excitation current of (a) 2 A. (b) 4 A. (c) 6 A. (d) 8 A. | 65 |

| | |
|--|----|
| Fig. 4.14. Generated back EMF line-to-line voltage at a constant speed of 750 rpm at field excitation current of (a) 2 A. (b) 4 A. (c) 6 A. (d) 8 A. | 66 |
| Fig. 4.15. Current tracking capability showing reference and measured direct axis currents. (a) Complete cycle response. (b) Zoomed step response..... | 67 |
| Fig. 4.16. Current tracking capability showing reference and measured quadrature axis currents. (a) Complete cycle response. (b) Zoomed step response..... | 67 |
| Fig. 4.17. Current tracking capability showing reference and measured quadrature axis currents. (a) Complete cycle response. (b) Zoomed step response..... | 68 |
| Fig. 4.18. Asymmetric stator phase currents in the presence of field excitation current. (a) Complete cycle response. (b) Zoomed step response. | 69 |
| Fig. 4.19. Symmetric stator phase currents in the presence of field excitation current. (a) Complete cycle response. (b) Zoomed step response. | 69 |
| Fig. 4.20. Closed-loop control validation during zero direct axis current for load profile-I. (a) Quadrature and field axis currents. (b) Three-phase stator phase currents. | 70 |
| Fig. 4.21. Closed-loop control validation during zero direct axis current for load profile-II. (a) Quadrature and field axis currents. (b) Three-phase stator phase currents. | 70 |
| Fig. 5.1. FTP75 Drive cycle speed profile..... | 77 |
| Fig. 5.2. Tractive torque required for FTP75 drive cycle. | 77 |
| Fig. 5.3. Doubly excited rotor configuration. (a) Conventional rotor excitation with 4 poles. (b) De-excited rotor with 2 poles..... | 78 |
| Fig. 5.4. Wound field synchronous machine with modified slip-ring assembly allowing selective rotor pole de-excitation. | 79 |
| Fig. 5.5. Single-legged converter circuit topology. | 80 |
| Fig. 5.6. Detailed Loss analysis of single-legged converter topology. | 81 |
| Fig. 5.7. Double-legged converter circuit topology..... | 82 |
| Fig. 5.8. Detailed Loss analysis of double-legged converter topology..... | 83 |
| Fig. 5.9. Conventional conductive/brushed rotor excitation converter topology. | 84 |
| Fig. 5.10. Torque-speed and efficiency profiles for conventional WFSM. | 85 |
| Fig. 5.11. Torque-speed and efficiency profiles for de-excited rotor WFSM. | 86 |
| Fig. 5.12. Flowchart of the proposed control strategy for rotor de-excitation..... | 87 |
| Fig. 5.13. Comparison of efficiencies in conventional and de-excited rotor configuration. | 88 |

LIST OF ABBREVIATIONS

| | |
|--------|---|
| BEV | Battery Electric Vehicles |
| CPU | Central Processing Unit |
| ETDS | Electric Traction Drive System |
| EV | Electric Vehicles |
| EMF | Electro-Motive Force |
| FTP | Federal Test Procedure |
| FPGA | Field Programmable Gate array |
| FEA | Finite Element Analysis |
| FWD | Front Wheel Drive |
| GHG | Green House Gasses |
| HEV | Hybrid Electric Vehicles |
| IPT | Inductive Power Transfer |
| IGBT | Insulated Gate Bipolar Transistor |
| ICE | Internal Combustion Engines |
| LPM | Liters Per Minute |
| LUT | Lookup Tables |
| MEPA | Maximum overall system Efficiency Per Ampere |
| MTPA | Maximum Torque Per Ampere |
| MOSFET | Metal Oxide Semiconductor Field Effect Transistor |
| OEM | Original Equipment Manufacturers |
| PMSM | Permanent Magnet Synchronous Machines |
| PHEV | Plug-in Hybrid Electric Vehicles |
| PEC | Power Electronic Controller |
| PI | Proportional-Integral |
| RCP | Rapid Control Prototyping |
| RLM | Rotor Loss Minimization |
| SPWM | Sine Pulse Width Modulation |
| SOC | State of Charge |

| | |
|--------|-------------------------------------|
| SVPWM | Space Vector Pulse Width Modulation |
| TLM | Total Loss Minimization |
| US DOE | US Department of Energy |
| VR | Variable reluctance |
| VSI | Voltage Source Inverter |
| WEG | Water Ethylene Glycol |
| WFSM | Wound Field Synchronous Machines |
| ZEV | Zero-Emission Vehicles |

CHAPTER 1

INTRODUCTION

Research and development interest in electric vehicles (EVs) has been increasing exponentially in recent years [1]-[5]. The objective behind this growth lies in addressing issues such as reducing greenhouse gases (GHG), meeting zero-emission targets, reducing carbon footprint, and increasing electric vehicle sales by creating awareness among the public, etc. [6], [7]. Electric Mobility Canada has set some crucial electric vehicle targets for the year 2030, such as 100% electric passenger vehicle sales, reduction in greenhouse gases by 40%-45%, and electrification of medium- and heavy-duty vehicles by at least by 2040 [8]. It is worthwhile to remember that from 2005 to 2019, only 1% of Canada's greenhouse gases decreased. To reach the targets, greenhouse gases still need to be reduced by 39%-44% in the next 9 years. As seen in Fig. 1.1 [9], a detailed comparison is made between an ICE vehicle and 300-mile electric vehicles to know the lifecycle emission of greenhouse gasses. This shows that the average emission of ICE vehicles over their lifetime is comparably more than that of electric vehicles. Electric vehicles are in the upper hand mainly because of zero tailpipe emissions. The primary GHG emission in EVs is contributed by feedstock and fuel and during battery manufacturing.

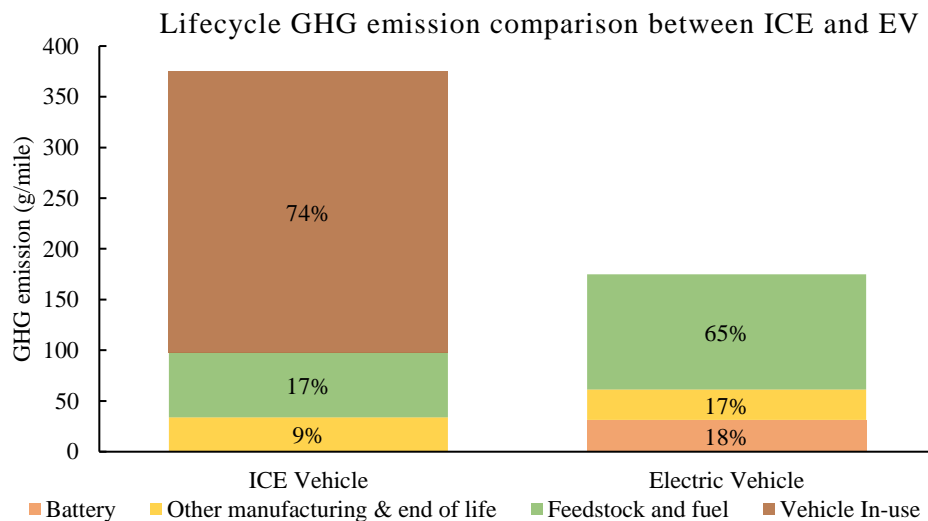


Fig. 1.1. Comparison of GHG emissions between ICE and EV [9].

Therefore, an accelerated transition is required from internal combustion engines (ICE) to electric vehicles (EV). As seen in Fig. 1.2 [11], many multinational original equipment manufacturers (OEMs) have announced their strategic electric roadmap in response to the transition from ICE to EVs [10], [11]. The Government of Canada and many other governments are providing numerous incentives to the public to use zero-emission vehicles (ZEV) [12], [13]. These incentives will be in place until the price of electric vehicles reaches parity with ICE vehicles. It is shown in a study that Canada has approximately 25 million registered vehicles. This includes both ICE and electric vehicles. To achieve the above-mentioned targets, a replacement of 1.8 million ICE vehicles is required. In other words, 7% of ICE vehicles should be replaced with EVs [14].

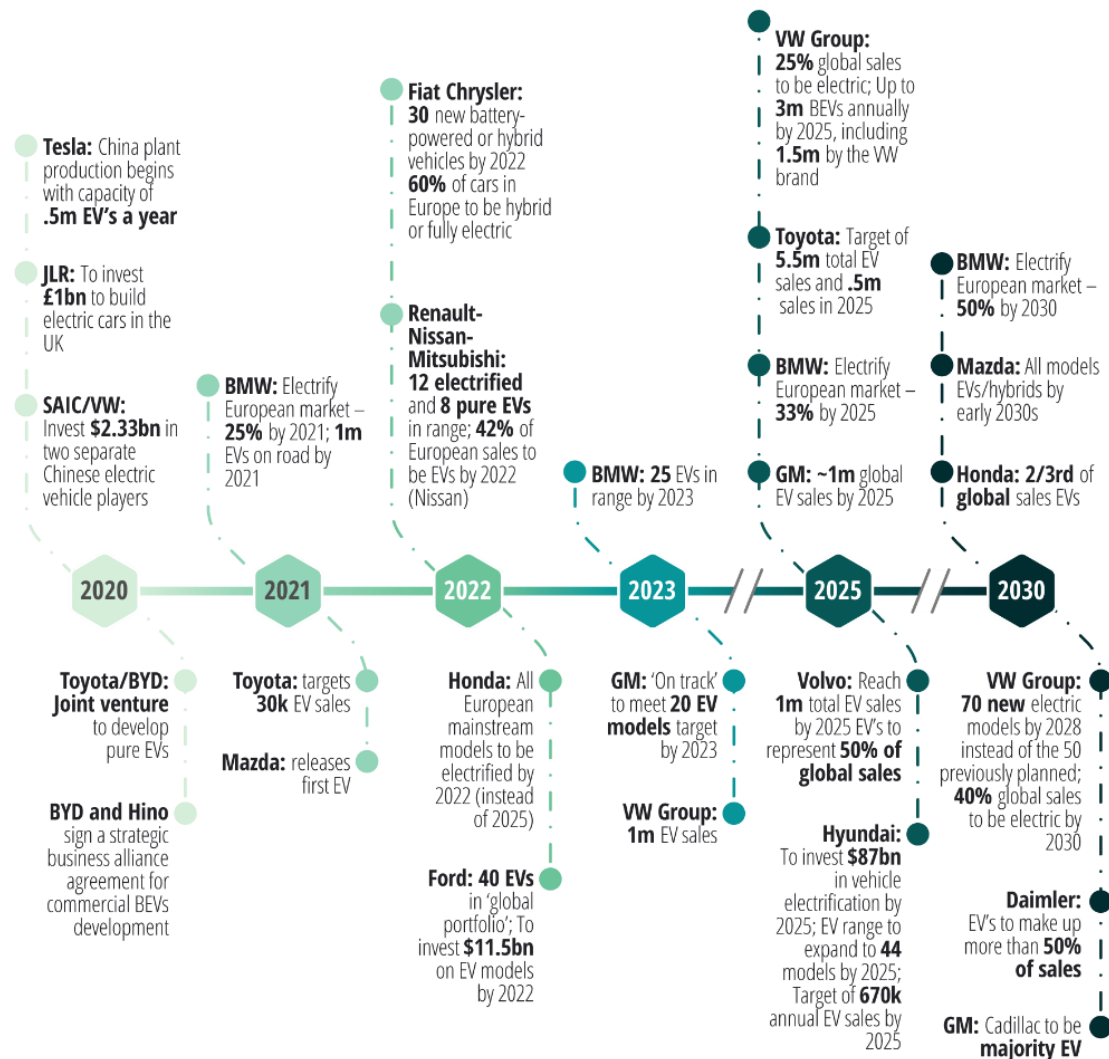


Fig. 1.2. Electrical vehicle target timelines of strategic OEMs [11].

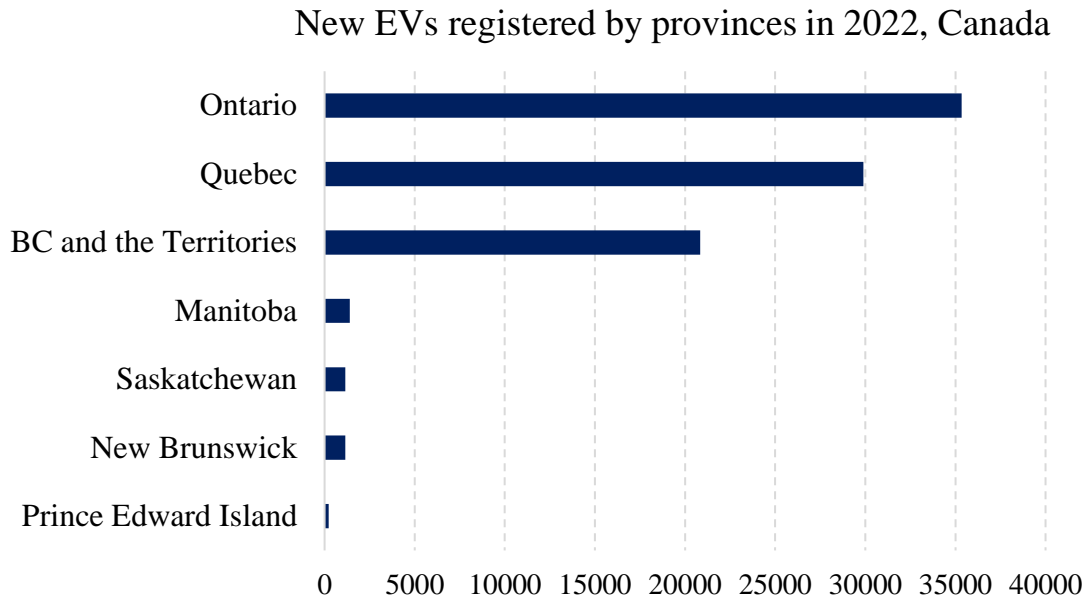


Fig. 1.3. New EVs registered by provinces in 2022, Canada [15].

In the year 2022, approximately 98,000 new electric vehicles are registered in Canada [15], where Ontario, Quebec, and British Columbia being the major players. This consists of battery electric vehicles (BEVs), hybrid electric vehicles (HEVs), and plug-in hybrid electric vehicles (PHEVs). The number of new electric vehicles registered is considerably lower than that of ICE vehicles. Therefore, there is an urgent need to boost research and development in the field of electric vehicles to reduce the initial cost and make them efficient, safe and more affordable. This will directly help in increasing the use of electric vehicles. The main focus of present and future research & development will be reducing the cost of electric motors, inverters, and batteries, increasing system energy efficiency, fast charging, increasing the range of EVs, reliability, autonomous driving, etc. These targets are according to the deliverables set by agencies like the department of energy and others [16]. Increasing the system's energy efficiency can be achieved through several methods. However, this thesis primarily focuses on developing intelligent control algorithms for an efficient electric powertrain system. The advantage of this approach is in adding minimal extra components and making the control algorithm more intelligent, robust, reliable, and competent. However, the hardware approach of improving efficiency is also discussed in this thesis.

1.1 Overview of Electric Vehicles

TABLE 1.1
COMMERCIALLY AVAILABLE ELECTRIC VEHICLES

| Brand | Model | Price (USD) | Range (km) | Battery Size (kWh) | Peak Power (kW) | 0-60 mph (sec) | Top Speed (mph) |
|------------|------------------------------|-------------|------------|--------------------|-----------------|----------------|-----------------|
| Audi | e-tron GT Quattro | \$102,400 | 238 | 93.4 | 390 | 3.9 | 152 |
| BMW | i4 eDRIVE40 | \$55,400 | 301 | 83.9 | 250 | 5.5 | 118 |
| Cadillac | Lyriq | \$58,795 | 300 | 100.4 | 255 | - | - |
| Chevrolet | Bolt EUV | \$33,000 | 247 | 65 | 150 | 7.0 | - |
| Ford | F-150 Lightning Platinum ER | \$90,874 | 280 | 145 | 420 | - | - |
| | Mustang Mach-E GT ER AWD | \$61,995 | 270 | 98.8 | 358 | 3.5 | - |
| GMC | Hummer EV Pickup | \$110,295 | 329 | 200 | 745 | 3.0 | - |
| Jaguar | I-PACE EV400 | \$69,900 | 237 | 90 | 294 | 4.5 | 124 |
| Hyundai | Ioniq Electric | \$33,245 | 170 | 38.3 | 100 | 10.0 | 102 |
| | Kona Electric | \$34,000 | 258 | 64 | 150 | 7.9 | 104 |
| Kia | Nitro EV | \$39,990 | 239 | 64 | 150 | 7.5 | 104 |
| Lucid | Air Grand Touring | \$139,000 | 469 | 112 | 596 | 3.0 | 168 |
| | Air Dream Edition Range | \$169,000 | 481 | 118 | 695 | 2.7 | 168 |
| Mercedes | EQS 580 4Matic | \$119,110 | 340 | 115 | 385 | 4.1 | 130 |
| Mini | Cooper SE | \$29,900 | 114 | 32.6 | 135 | 6.9 | 93 |
| Nissan | Ariya Venture FWD | \$45,950 | 300 | 91 | 178 | - | - |
| Porsche | Taycan Turbo S Cross Turismo | \$187,600 | 202 | 93.4 | 560 | 2.7 | 155 |
| Rivian | R1T | \$67,500 | 314 | 135 | 562 | 3.0 | 125 |
| Tesla | Model 3 RWD | \$44,990 | 272 | 60 | - | 5.8 | 140 |
| | Model S Plaid | \$134,490 | 348 | 100 | 760 | 2.0 | 200 |
| | Model X Plaid | \$131,990 | 311 | 100 | 760 | 2.5 | 163 |
| | Model Y Long Range AWD | \$60,990 | 318 | 80 | - | 4.8 | 135 |
| Volvo | XC40 Recharge | \$55,300 | 223 | 78 | 300 | 4.7 | 112 |
| Volkswagen | ID.4 AWD Pro S | \$48,940 | 240 | 82 | 220 | 5.8 | 111 |

The very first electric vehicle was introduced in the market in the early 1800s [17]. It is seen in the literature that the first EV was developed by a British inventor. However, the first full-scale electric vehicle was built in the USA by William Morrison from Iowa. Morrison's electric vehicle has the capacity to accommodate a dozen of people and with a top speed of 20 mph. Later, the transition from traditional carts to internal combustion vehicles began. With the wide availability of gasoline fuel after the discovery of crude oil in Texas, the mass production and rise of ICE vehicles started. There was a prominent inclination towards electric vehicles with the release of the Toyota Prius in 1997 [18]. This was the vehicle in the world that had witnessed mass production. In the 2000s, electric vehicles made a complete comeback with the huge drop in lithium-ion batteries. Now, we see exponential growth in electric vehicles, with increased range, reduced prices, etc. Various commercially available electric vehicles with cost, range, etc., are populated in the Table. 1.1 [19], [20].

1.2 Electric Traction Drive Technology

Electric vehicle powertrain has many important subsystems such as: 1) High voltage battery: The main source of power for the electric vehicle. The high-voltage battery can be charged and discharged based on the state of charge (SoC). Charging can be done either from a power grid or through regenerative braking. 2) DC/DC converter: The DC/DC converter converts the high-voltage DC from a high-voltage battery to all the low-voltage devices on the electric vehicle. 3) E-motor: The electric motor converts electrical energy to mechanical energy. The electrical power is supplied by the high-voltage battery onboard, and the output mechanical energy is transmitted to the drivetrain and eventually to the wheels. 4) Onboard charger: The onboard charger has many power electronic circuits which are responsible for charging the high-voltage battery when connected to the power grid. 5) Power electronic controller: The power electronic controller is the brain of the electric vehicle. The intelligent motor control algorithm embedded inside the power electronic controller (PEC) controls the electric motor and the inverter in the most efficient manner. The inverter is a part of PEC, and it converts the DC voltage from high-voltage battery to a three-phase AC that is fed to the motor. 6) Cooling circuits: Liquid cooling circuits are usually employed for cooling the heat dissipated by the electric motor, inverter, and battery. 7) Transmission: The mechanical power generated by the electric motor is

transmitted through the gearbox and then to the wheel. Fig. 1.4 shows the detailed powertrain layout consisting of a high-voltage battery, electric motor, inverter stack, etc. [21]. As seen in the below figure, the electric motor delivers power to the front wheels of the vehicle, i.e., the front wheel drive (FWD) drivetrain. Fig 1.5 shows the characteristics of the electric motor that propels the power train. The torque-speed profile is seen to be constant from zero until the base speed and then gradually decreases. The power-speed profile is seen to be linearly increasing until the base speed and then constant throughout. Hence, it is termed as constant torque and constant power regions, respectively. It is usually desired to have extended constant torque and power regions for maximum performance.

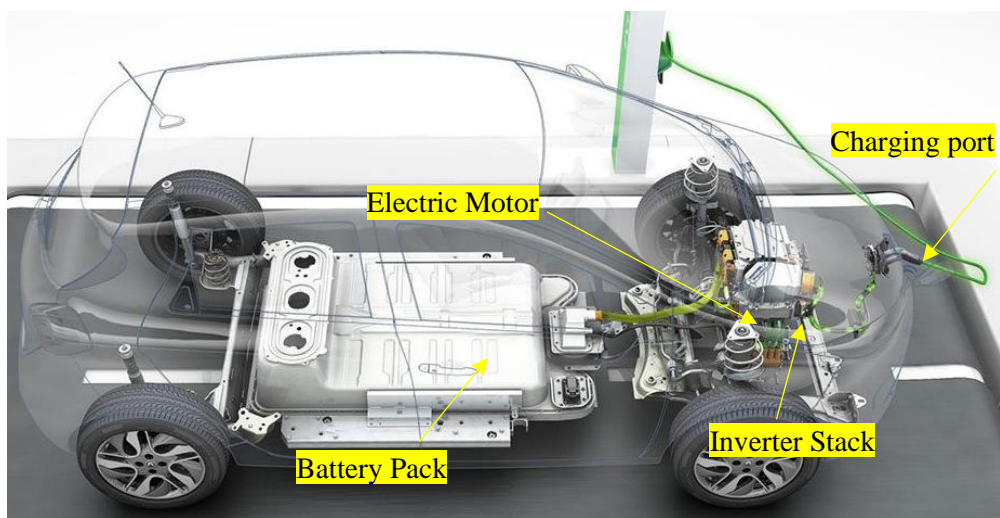


Fig. 1.4. Electric vehicle powertrain showing various internal components [21].

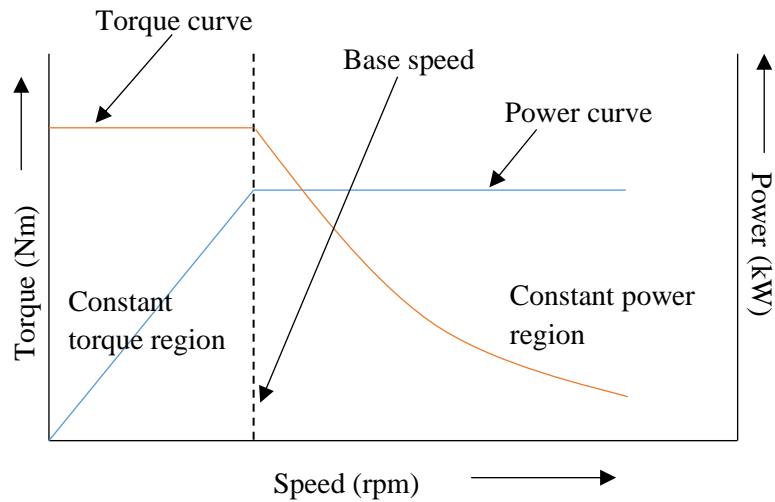


Fig. 1.5. Torque-speed and power-speed profile of a WFSM.

1.3 Overview of Wound Field Synchronous Machine Drives

There is an increased inclination towards wound field synchronous machines (WFSM) in recent years [22]-[24]. The main advantages of WFSMs are seen in having an extra degree of control in the field axis, i.e., i_f current control and lack of rare earth permanent magnets. This leads WFSM drives to advantages such as improved power factor control, extended flux weakening region, short circuit current handling capacity, etc. [25]. A few noteworthy examples of WFSM drives used in the EV powertrain are Renault Zoe, Renault Fluence Z.E, BMW fifth-generation electric motors, General Motors-developed prototypes, BRUSA Elektronik AG, etc. [26]. Figure. 1.6 shows the schematic diagram of a complete powertrain electrical connection. As seen, a two-level three-phase IGBT/MOSFET inverter converts the DC power from the high voltage battery to drive the electric motor. The three-phase inverter is controlled by an intelligent control algorithm that decides the strategy of power flow into the electric motor to achieve the commanded speed and torque by the vehicle driver. The efficiencies of the three-phase inverter and electric motor can be improved mainly in two methods: 1) increasing the efficiency through changes in the hardware, and 2) increasing the efficiency through an intelligent control algorithm.

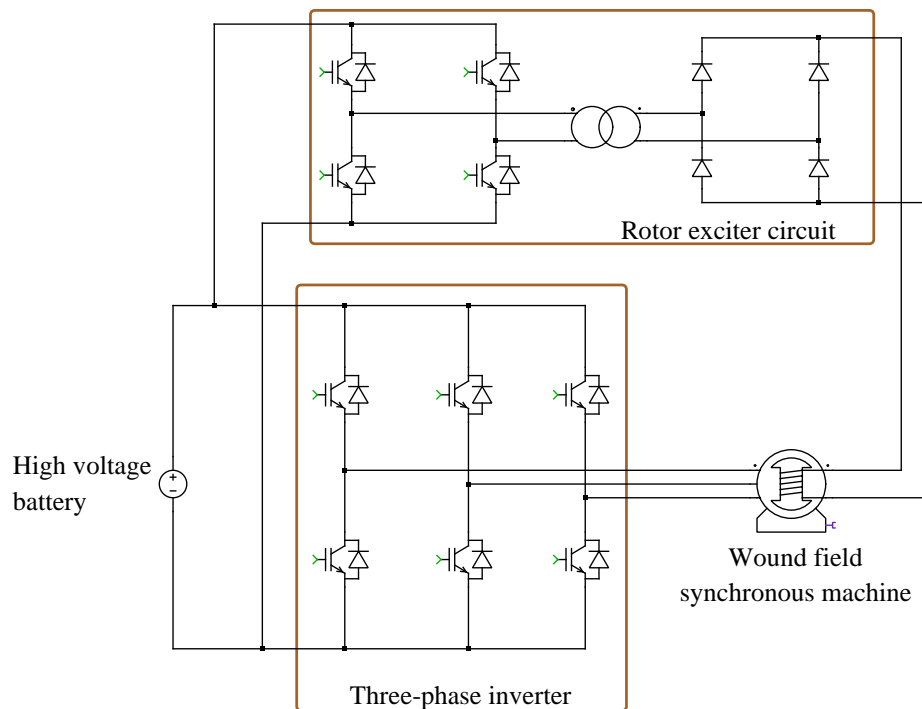


Fig. 1.6. Schematic diagram of EV powertrain with WFSM as e-motor.

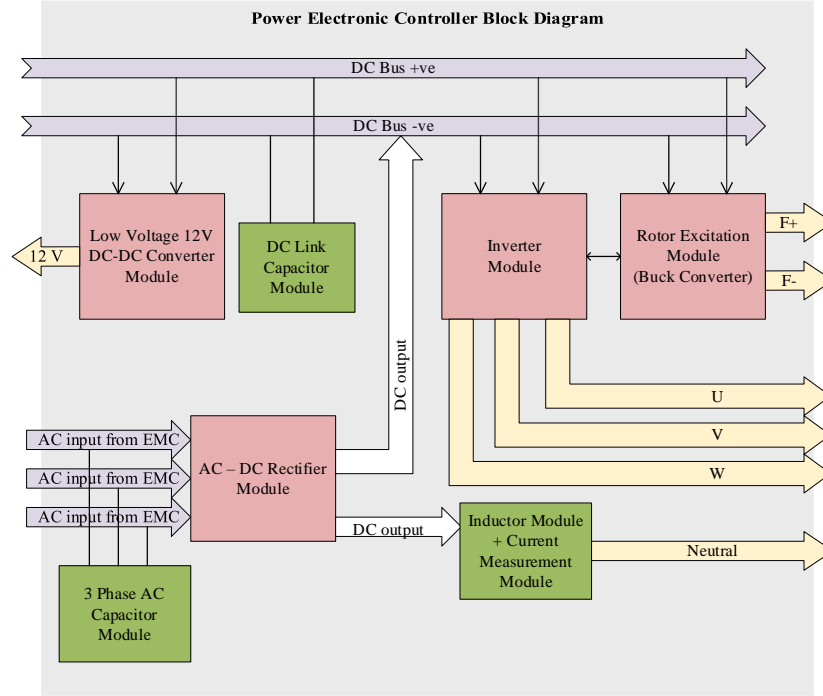


Fig. 1.7. Block diagram showing power flow in a commercially available PEC stack.

Figure 1.7 shows the detailed power flow of a commercially available power electronic converter stack. The shown block diagram also includes an integrated charging strategy for charging the battery. Integrated charging uses the three-phase electric motor winding as an inductor to boost the DC voltage. This helps eliminate extra heavy inductor components added to the power electronic converter [27].

1.4 Motivation and Research Objective

The main motivation of this thesis is to increase the overall system level energy efficiency with minimal addition of power electronic components for the WFSM drives. In other words, increasing the energy efficiency of the overall system through improved intelligent control algorithms. The reason behind the choice of WFSMs lies in the design of WFSM rotors. The rotor of WFSMs uses copper windings by completely neglecting the usage of rare earth permanent magnets. This helps in reducing the overall cost of the electric motor as the cost of rare earth permanent magnets such as neodymium magnets are dramatically increasing by 300% since early 2021 [28]. The US department of energy (DOE) also provided an electrical and electronics roadmap in the year 2017, mentioning a few important research targets for the year 2025 [16]. The targets are as follows: 1) Electric

vehicle cost should be no more than that of comparable internal combustion engine vehicles. 2) Cost difference between EV and ICE vehicles should be no greater than three years of fuel cost savings. 3) Cost of a 100-kW peak power electric traction drive system (ETDS) should be \$6 USD/kW with \$2.7 USD/kW for a power electronic of 100 kW/L power density and \$3.3 USD/kW for an electric motor of 50 kW/L power density. 4) Electric vehicle reliability should be at least 15 years or 150,000 miles.

Based on the above-mentioned motivations, the research objective of this thesis is primarily focused on improving the overall system efficiency of WFSM drives. This is crucial as an increase in power density (kW/L) will increase the stator and rotor copper losses for the same machine volume. The copper losses (i^2r) in the stator and rotor increase as more current will be injected into the machines causing increased i^2r losses. Therefore, an advanced intelligent control algorithm is required to operate the system in an optimal condition that results in overall system efficiency with respect to the operating point in the torque-speed profile of a given electric motor. However, improving the efficiency through the change in hardware is also proposed in this thesis.

1.5 Research Contribution

The major contribution of this thesis is summarized below:

1. Develop a detailed mathematical model of a wound field synchronous machine (WFSM), three-phase inverter, conductive and inductive rotor excitation systems, and vehicle dynamics model. Loss modeling of WFSM, inverter, and converters. Validating the developed model with the finite element analysis (FEA) and experimental data.
2. Design a closed-loop current/speed control using proportional-integral controller and validated it with simulation and experimentations. Develop a maximum overall system efficiency per ampere intelligent motor control using loss modeling of motor, inverter, and rotor exciter circuit.
3. Hardware implementation of developed closed-loop current control of WFSM on a real-time embedded controller towards dynamic and transient response validation with a commercially available WFSM.
4. Develop a novel converter and control topology for enhancing the energy efficiency of the WFSM drive.

1.6 Organization of This Thesis

This thesis presents the research conducted in developing an intelligent motor control algorithm for maximum overall system efficiency and developing a novel converter and control topology for enhancing the energy efficiency of wound field synchronous machine drives in six chapters. This includes both the introductory and conclusion chapters.

Chapter 1 introduces the architecture of electric vehicles' powertrains and discusses various advantages of using electric vehicles compared to internal combustion engines. It also emphasizes the urgency of the transition to EVs from ICE vehicles. The motivation, research objective, and research contributions are clearly elaborated.

Chapter 2 presented in-detail mathematical modeling of WFSM, stator inverter, rotor converter, and loss modeling. The simulation results of WFSM, inverter, and various rotor excitation topologies are also presented.

Chapter 3 discusses the design and implementation of closed-loop speed and current controller by designing proportional-integral (PI) controllers. A comparison between conventional total- and rotor-loss minimization techniques are presented. Aligning to the research objective, a maximum overall system efficiency per ampere intelligent control is proposed using the developed loss model of the system. The advantages of the proposed control algorithm over the conventional maximum torque per ampere are discussed.

Chapter 4 extends the research presented in Chapters 2 and 3 to build, implement, and validate the proposed controls using a real-time embedded controller and a commercially available wound field synchronous machine on a 175 kWp high-speed dynamometer test bench.

Chapter 5 proposes a novel converter and control topologies for a doubly excited wound field synchronous machine towards improving efficiency. Finite element analysis and simulation results are presented, supporting the proposed topologies and method.

Chapter 6 concludes the thesis by summarizing the research presented on maximizing the overall system efficiency of WFSM drives for EV application. The future work to further extend this research is also discussed.

1.7 Conclusion

In this chapter, an introduction to electric vehicles and detailed electric vehicle powertrain architecture is explained. Moreover, the advantages of using electric vehicles

over internal combustion engines are discussed, and the inclination of OEMs, and the road map of various OEMs transitioning towards an electric vehicle are shown. The need for the hour of the presented research, motivation, research objectives, and research contribution are also highlighted in this chapter. In the end, a detailed layout of the thesis is mentioned for better understanding.

1.8 References

- [1] Statista. (2022, Oct.). Electrical Vehicles – Worldwide. [Online]. Available: <https://www.statista.com/outlook/mmo/electric-vehicles/worldwide>
- [2] L. Paoli. (2022, Sep.) Electrical Vehicles. LEA. [Online]. Available: <https://www.iea.org/reports/electric-vehicles>
- [3] M. Dennis. (2021, Sep.) Are We on the Brink of an Electric Vehicle Boom? Only with More Action. World Resources Institute. [Online]. Available: <https://www.wri.org/insights/what-projected-growth-electric-vehicles-adoption>
- [4] Virta. (2022, Oct.). The Global Electric Vehicle Market Overview in 2022: Statistics & Forecasts. [Online]. Available: <https://www.virta.global/en/global-electric-vehicle-market>
- [5] S. Blanco. (2022, Aug.). Electric Cars’ Turning Point May Be Happening as U.S Sales Number Start Climb. Car and Driver. [Online]. Available: <https://www.caranddriver.com/news/a39998609/electric-car-sales-usa/>
- [6] V. McConnell and B. Leard. (2020, Dec.). Progress and Potential for Electric Vehicles to Reduce Carbon Emissions. Resources. [Online]. Available: <https://www.rff.org/publications/reports/potential-role-and-impact-evs-us-decarbonization-strategies/>
- [7] Plug ‘N Drive. (2022, Oct.). Electric Car Benefits. [Online]. Available: <https://www.plugndrive.ca/electric-vehicle-benefits/>
- [8] Electric Mobility Canada. (2021, Nov.). Electric Mobility Canada Sets Important Electric Vehicle Target with Its 2030 EV Action Plan. [Online]. Available: <https://emc-mec.ca/new/electric-mobility-canada-sets-important-electric-vehicle-targets-with-its-2030-ev-action-plan/>
- [9] EPA. (2022, Oct.). Electric Vehicle Myths. [Online]. Available: <https://www.epa.gov/greenvehicles/electric-vehicle-myths>

- [10] N. Winton. (2022, Oct.). BMW, VW Will Lead Belated Electric Charge; FCA, Toyota Lag as China Sprints Ahead. Forbes. [Online]. Available: <https://www.forbes.com/sites/neilwinton/2017/09/08/bmw-vw-will-lead-belated-electric-charge-fca-toyota-lag-as-china-sprints-ahead/?sh=7ce9e94b5df7>
- [11] M. Woodward *et al.*, (2020, July). Electric Vehicles – Setting a Course for 2030. Deloitte. [Online]. Available: <https://www2.deloitte.com/us/en/insights/focus/future-of-mobility/electric-vehicle-trends-2030.html>
- [12] Transport Canada. (2022, Nov.). Incentives for Purchasing Zero-Emission Vehicles. [Online]. Available: <https://tc.canada.ca/en/road-transportation/innovative-technologies/zero-emission-vehicles/light-duty-zero-emission-vehicles/incentives-purchasing-zero-emission-vehicles>
- [13] Transport Canada. (2022, Nov.). Eligible Vehicles - Incentives for Purchasing Zero-Emission Vehicles. [Online]. Available: <https://tc.canada.ca/en/road-transportation/innovative-technologies/zero-emission-vehicles/light-duty-zero-emission-vehicles/eligible-vehicles>
- [14] PwC Canada. (2022, Nov.). Accelerating Canada’s Electric Vehicle Transition. [Online]. Available: <https://www.pwc.com/ca/en/industries/automotive/publications/accelerating-canadas-electric-vehicle-transition.html>
- [15] Statistics Canada. (2022, Nov.). New Motor Vehicle Registrations: Quarterly Data Visualization Tool. [Online]. Available: <https://www150.statcan.gc.ca/n1/pub/71-607-x/71-607-x2021019-eng.htm>
- [16] U.S Department of Energy. (2017, Oct.). Electrical and Electronics Roadmap. pp 1-41, 2017
- [17] U.S Department of Energy. (2014, Sep.). The History of the Electric Car. [Online]. Available: <https://www.energy.gov/articles/history-electric-car>
- [18] J. D. Simpson and W. V. Barlingen. (2021, Nov.). The History of Electric Cars. Evbox. [Online]. Available: <https://blog.evbox.com/electric-cars-history>
- [19] M. Kane. (2022, July). Compare Electric Cars: EV Range, Specs, Pricing & More. INSIDEEVs. [Online]. Available: <https://insideevs.com/reviews/344001/compare-evs/>

- [20] S. Oldham *et al.*, (2022, Oct.). Here's Every New Electric Vehicle Model for Sale in the U.S for 2022. Car and Driver. [Online]. Available: <https://www.caranddriver.com/shopping-advice/g32463239/new-ev-models-us/>
- [21] Green Car Congress. (2012, Mar.). Renault Features Production Version of ZOE, Twizy EV at Geneva. [Online]. Available: <https://www.greencarcongress.com/2012/03/zoe-20120309.html>
- [22] A. Frias *et al.*, "Rotor and stator shape optimization of a synchronous machine to reduce iron losses and acoustic noise," in *Proc. IEEE Veh. Power Propulsion Conf.*, Oct. 2012, pp. 98–103.
- [23] C. Stancu, T. Ward, K. M. Rahman, R. Dawsey, and P. Savagian, "Separately excited synchronous motor with rotary transformer for hybrid vehicle application," *IEEE Trans. Ind. Appl.*, vol. 54, no. 1, pp. 223–232, Jan./Feb. 2018.
- [24] I. Jeong, J. Kim, Y. Kim, and K. Nam, "Extended MTPA with cross coupling inductances for electrically excited synchronous motors," in *Proc. IEEE Energy Convers. Congr. Expo.*, Sep. 2013, pp. 867–873.
- [25] A. K. Jain and V. T. Ranganathan, "Modeling and Field Oriented Control of Salient Pole Wound Field Synchronous Machine in Stator Flux Coordinates," *IEEE Transactions on Industrial Electronics*, vol. 58, no. 3, pp. 960-970, March 2011, doi: 10.1109/TIE.2010.2048295.
- [26] Y. Nie, D. C. Ludois, and I. P. Brown, "Deadbeat-Direct Torque and Flux Control of Wound Field Synchronous Machine at Low Sampling to Fundamental Frequency Ratios," *IEEE Trans. Industry Applications*, vol. 55, no. 4, pp. 3813-3822, July-Aug. 2019, doi: 10.1109/TIA.2019.2914681.
- [27] S. Loudot, B. Braine, O. Ploix, and A. Villeneuve, "Fast charging device for an electric vehicle," Pub. No.: US 2012/0286740 A1, Nov 15, 2012.
- [28] Magnosphere, Neodymium Magnets with Drastic Price Developments. [Online] Available: <https://www.magnosphere.co.uk/information-permanent-magnet/price-explosion-for-neodymium-magnets-raw-material>

CHAPTER 2

MODELING AND SIMULATION OF THE WFSM E-DRIVE SYSTEM WITH VARIOUS EXCITATION TECHNIQUES

2.1 Introduction

This chapter elaborates on the detailed mathematical modeling of a wound field synchronous machine (WFSM). This includes a discussion on reference frame theory, equivalent circuit representation and mathematical modeling of WFSM, magnetic saturation and cross-coupling effects, loss modeling, etc. [1]-[3]. In a similar manner, the mathematical modeling of the three-phase inverter, conductive excitation system, inductive power transfer system, and vehicle dynamics are explained in detail. The above-mentioned developed mathematical models are utilized in the next chapter to develop the proposed control algorithms.

2.2 Modeling of Wound Field Synchronous Machine

2.2.1 Reference Frame Theory

A three-phase WFSM has three RL load stator phase windings connected in either star or delta configuration. These three-phase windings generate a rotating magnetic field when excited by three-phase currents. On the other hand, there is an RL load field winding wound to the rotor. Hence, the motor is termed a wound field synchronous machine. The rotor field winding is excited by a DC current. It is known that the WFSM inductances (L_a , L_b , L_c) vary according to the rotor position. Therefore, the voltage equations coefficients describing the motor dynamics change according to the rotor position. This, in return, becomes difficult to perform closed-loop control of the machine. The closed-loop control algorithm becomes more complex and time-consuming because of the differential equations' varying coefficients. In 1920s, R. H. Park proposed a new concept of change in reference frame theory that revolutionized machine control and analysis [4]. The proposed change of reference theory eliminated the coefficients of differential equations that change with the rotor positions. Replacing the stationary reference frame, a new rotating frame of reference rotating at the angular velocity of the rotor is introduced [5]. The main advantages of change in the reference frame are mentioned as follows: 1) Eliminating machine inductances that vary with respect to time/rotor position.

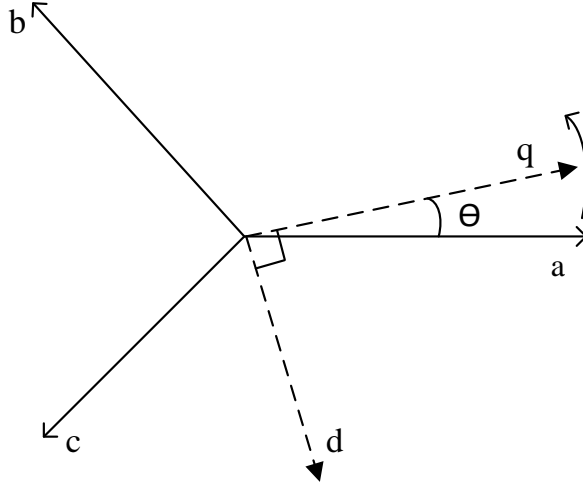


Fig. 2.1. Park's transformation.

2) Reduces the complexity of the machine's voltage differential equation. 3) Easier implementation of motor control and detailed analysis. This transformation from the stationary reference frame to the rotating reference frame is often known as *abc* to *dq* or Park's transformation. Representation of *abc* and *dq* reference frame is shown in Fig. 2.1. The change of reference frame from stationary to rotating reference frame is given as follows [5], [6]

$$f_{dq0} = K_s f_{abc} \quad (2.1)$$

where,

$$(f_{dq0})^T = [f_d \quad f_q \quad f_0] \quad (2.2)$$

$$(f_{abc})^T = [f_a \quad f_b \quad f_c] \quad (2.3)$$

$$K_s = \frac{2}{3} \begin{bmatrix} \cos \theta & \cos\left(\theta - \frac{2\pi}{3}\right) & \cos\left(\theta + \frac{2\pi}{3}\right) \\ \sin \theta & \sin\left(\theta - \frac{2\pi}{3}\right) & \sin\left(\theta + \frac{2\pi}{3}\right) \\ \frac{1}{2} & \frac{1}{2} & \frac{1}{2} \end{bmatrix} \quad (2.4)$$

The inverse transformation is given as,

$$f_{abc} = K_s^{-1} f_{dq0} \quad (2.5)$$

$$K_s^{-1} = \begin{bmatrix} \cos \theta & \sin \theta & 1 \\ \cos\left(\theta - \frac{2\pi}{3}\right) & \sin\left(\theta - \frac{2\pi}{3}\right) & 1 \\ \cos\left(\theta + \frac{2\pi}{3}\right) & \sin\left(\theta + \frac{2\pi}{3}\right) & 1 \end{bmatrix} \quad (2.6)$$

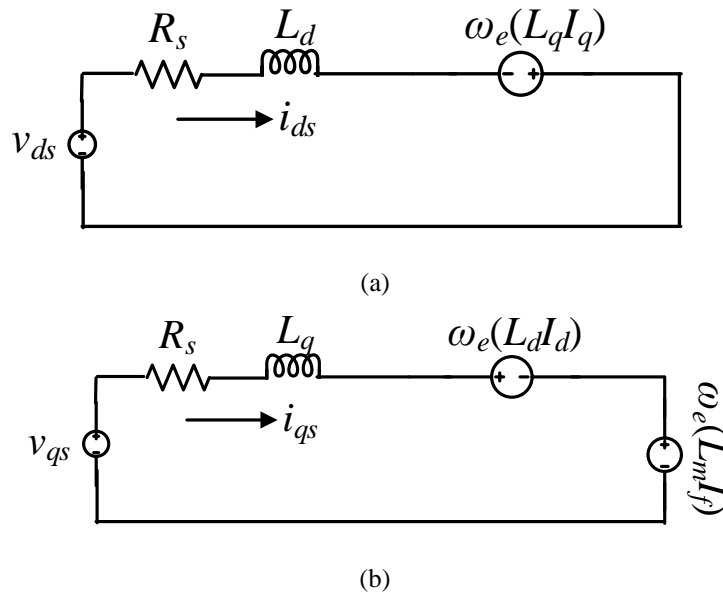
The relation between angular position and velocity is given as follows,

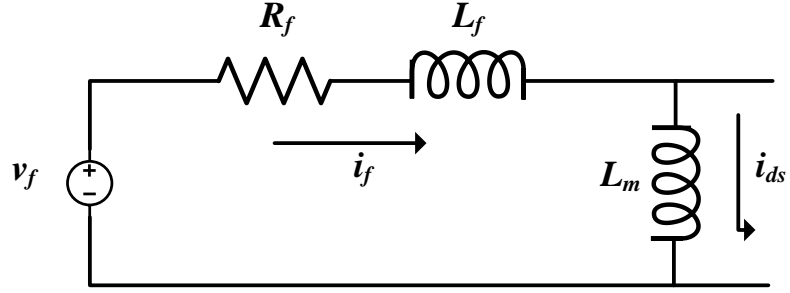
$$\frac{d\theta}{dt} = \omega \quad (2.7)$$

The equation (2.1) can be applied for the transformation of voltage, current, flux linkage, etc.

2.2.2 Equivalent Circuit Diagram and Mathematical Modeling of WFSM

The equivalent circuit diagrams of a WFSM in dqf -axis is shown in Fig. 2.2. The equivalent circuit diagrams of dqf -axis are represented in the rotating reference frame or Park's reference frame. Where v_{ds} , v_{qs} , v_f are the dqf -axis voltages, R_s and R_f are the stator and rotor field resistance, L_d , L_q , L_f are the dqf -axis inductance, L_m is the mutual inductance between the d - and f -axis. ω_e is the electrical speed in radians per second.





(c)

Fig. 2.2. Equivalent circuit diagram of wound field synchronous machine. (a) d -axis circuit. (b) q -axis circuit. (c) f -axis circuit.

The voltage equations of the three-phase wound field synchronous machine govern the electrical and mechanical dynamics of the machine. The voltage equations for the stator represented in the rotating frame of reference are given as follows in the equations (2.8) - (2.13) [7], [8]:

$$v_{ds} = r_s i_{ds} + \frac{d\lambda_{ds}}{dt} - \omega_r \lambda_{qs} \quad (2.8)$$

$$v_{qs} = r_s i_{qs} + \frac{d\lambda_{qs}}{dt} + \omega_r \lambda_{ds} \quad (2.9)$$

$$v_{fr} = r_f i_{fr} + \frac{d\lambda_{fr}}{dt} \quad (2.10)$$

where,

$$\lambda_{ds} = L_d i_{ds} + L_m i_{fr} \quad (2.11)$$

$$\lambda_{qs} = L_q i_{qs} \quad (2.12)$$

$$\lambda_{fr} = L_f i_{fr} + \frac{3}{2} L_m i_{ds} \quad (2.13)$$

Equations (2.8) to (2.10) represent the stator and rotor voltage equations. It is to be noted that damper windings are omitted for this type of machine. This is because the machine is

assumed to be excited by a voltage source inverter (VSI). The flux linkages in dqf axes are expressed from (2.11) to (2.13). The generated electromagnetic torque is given as follows:

$$T_e = \frac{3}{4} P \left[\lambda_d i_{qs} - \lambda_q i_{ds} \right] \quad (2.14)$$

Substituting (2.11) and (2.12) in (2.13):

$$T_e = \frac{3}{4} P \left[(L_d i_{ds} + L_m i_{fr}) i_{qs} - (L_q i_{qs}) i_{ds} \right] \quad (2.15)$$

Re-writing (2.15) as (2.16),

$$T_e = \frac{3}{4} P \left[(L_d - L_q) i_{qs} i_{ds} + (L_m i_{fr}) i_{qs} \right] \quad (2.16)$$

The mechanical equations are described in (2.17) and (2.18),

$$\frac{d}{dt} \omega_m = \frac{1}{J} (T_e - T_f - T_L) \quad (2.17)$$

$$T_f = B \omega_m \quad (2.18)$$

Where, T_e is the electromagnetic torque, T_f is the friction torque, T_L is the load torque, P is the number of poles, J is the inertia, B is the friction coefficient, and ω_m is the mechanical speed.

2.2.3 Magnetic Saturation and Cross-Coupling Effects

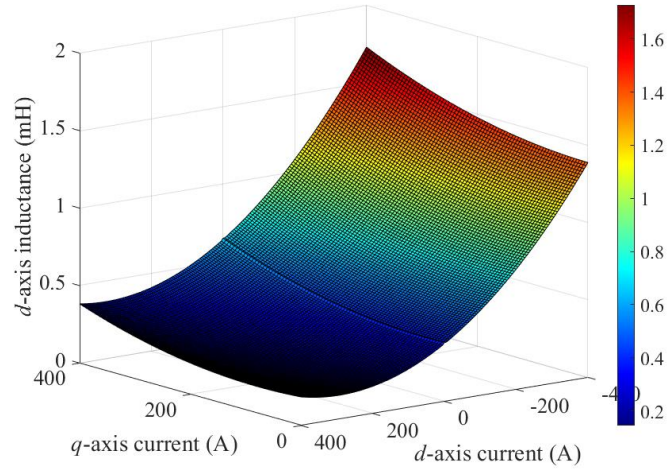
Synchronous machines such as WFSM are highly non-linear compared to permanent magnet synchronous machines (PMSMs). Non-linearity is to be considered to a greater extent for precise motor control and detailed analysis [9]. Moreover, the dq -axis inductances in WFSM are cross-coupled with the field axis and vary with changes in excitation field current [10]. Equations (2.19) to (2.21) are the flux linkages in dqf -axis as a function of dqf currents [11].

$$\lambda_d(i_d, i_q, i_f) = L_{dd} i_d + L_{dq} i_q + L_m i_f \quad (2.19)$$

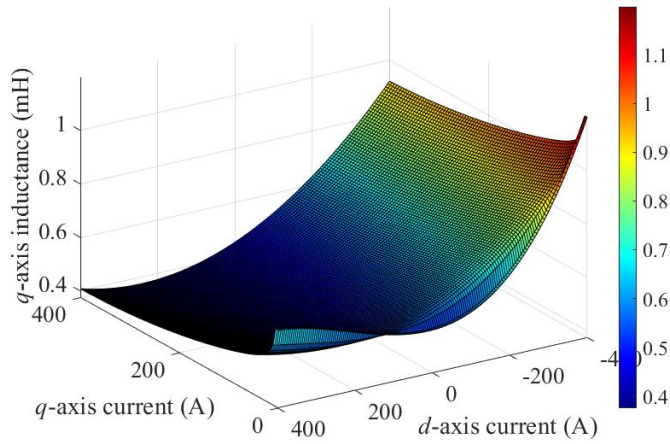
$$\lambda_q(i_d, i_q, i_f) = L_{qq} i_q + L_{qd} i_d \quad (2.20)$$

$$\lambda_f(i_d, i_q, i_f) = L_f i_f + \frac{3}{2} L_{md} i_d \quad (2.21)$$

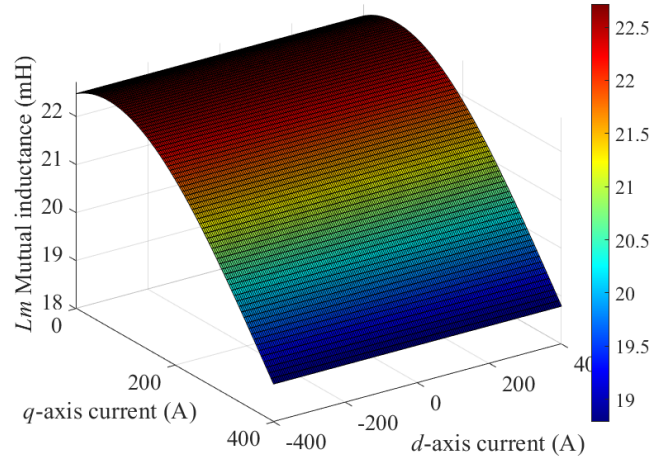
where, L_{dd} and L_{qq} are the d - and q -axis self-inductances, respectively. L_{dq} and L_{qd} are the mutual inductances between the d and q axes. L_{md} is the mutual inductance between the d and f axes. In the mathematical modeling of the WFSM, the inductance non-linearity is incorporated as lookup tables (LuTs). The inductance L_d and L_q are represented as a function of i_d , i_q , and i_f . As shown in Fig. 2.3, the inductances are generated from zero to maximum q -axis peak current and from maximum negative d -axis to maximum positive d -axis current at various f -axis currents. The d -axis is swept from positive maximum to negative minimum because of variation in phase advance from -90° to $+90^\circ$. For increased accuracy and precision, inductance maps are generated in a high computational power FEA. The variation of mutual inductance L_m with respect to i_{dqf} non-linearity map is also included to improve accuracy.



(a)



(b)



(c)

Fig. 2.3. Inductance saturation profile at rated field excitation current. (a) d -axis inductance profile. (b) q -axis inductance profile. (c) Mutual inductance between d and f axes.

Unlike in PMSMs, In WFSMs, the field excitation current can be varied. Hence, the rotor flux can also be controlled according to the control algorithm. Apart from the cross-coupling effects between d and q axes in the WFSM, there exists another cross-coupling between d and f axis directly and q and f axis indirectly. The interactions of various axes and cross-coupling effects are shown in Fig. 2.4. Substituting the equation (2.13) to (2.10) we get,

$$i_{fr} = \frac{1}{R_f} \left(v_{fr} - L_f \frac{di_{fr}}{dt} - \frac{3}{2} L_m \frac{di_{ds}}{dt} \right) \quad (2.22)$$

From equation (2.22), it can be observed that i_{fr} is directly influenced by i_{ds} . However, this effect only appears during a change in i_{ds} because of the derivative term. These effects might be more evident depending on the turns ratio between the stator and rotor (N_s/N_f). In the WFSM mathematical modeling, the above-mentioned cross-coupling effects are included to capture the transient effects.

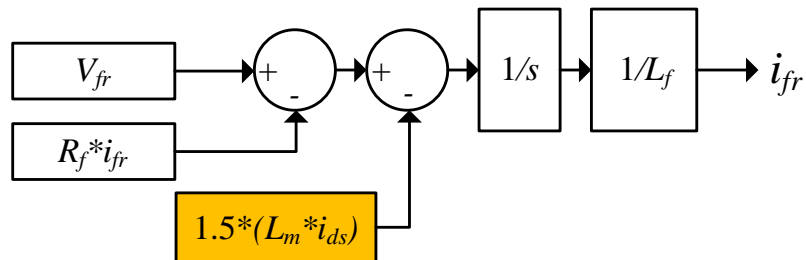
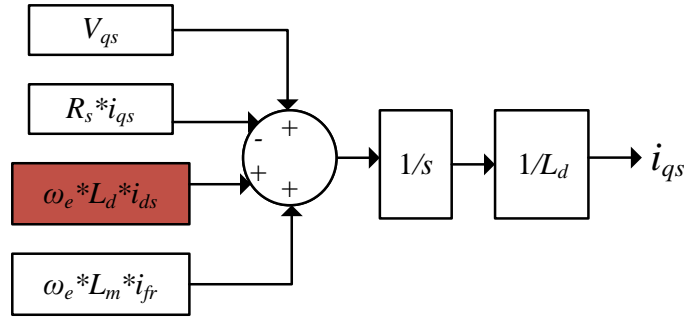
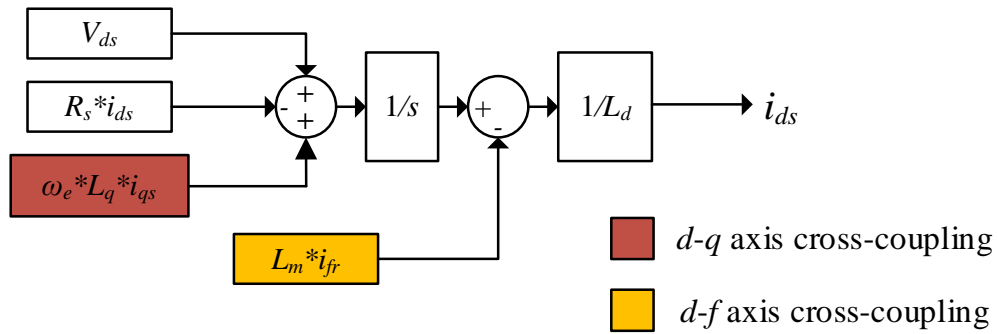


Fig. 2.4. Cross-coupling effect includes magnetic saturation. (a) d -axis. (b) q -axis. (c) f -axis.

2.2.4 Loss Modeling of WFSM

As mentioned in Chapter I, the main objective of this thesis focuses on developing a maximum system efficiency control. Therefore, loss modelling of the WFSM is required. The detailed loss modeling of the WFSM includes copper and core losses of the stator and rotor. The copper losses in WFSM will include both the stator copper losses and rotor copper losses. Usually in a WFSM, the rotor copper losses are dominated by the stator copper losses. The equations for the copper losses are given as follows [12]-[14]:

$$P_{cu-stator} = 3i_s^2 R_s \quad (2.23)$$

$$P_{cu-stator} = 3(i_d^2 + i_q^2) R_s \quad (2.24)$$

$$P_{cu-rotor} = i_f^2 R_f \quad (2.25)$$

$$P_{cu-total} = P_{cu-stator} + P_{cu-rotor} \quad (2.26)$$

where R_s is the stator phase resistance, and R_f is the field winding resistance.

The core losses are emitted on the core of WFSM's stator and rotor. This is mainly because of the eddy and hysteresis losses. There are many approaches for calculating the core losses of a synchronous machine in the literature, such as Bertotti (Maxwell method), Bertotti (classical method), Steinmetz method, etc. Out of these, the Modified Steinmetz method is used for calculating the losses. The equation for the stator core losses is given as follows [15]-[18]:

$$W_{Fe} [W / kg] = K_h \cdot f \cdot B^{(\alpha+\beta)} + 2 \cdot \pi^2 \cdot K_{eddy} \cdot f^2 B^2 \quad (2.27)$$

where f is the frequency, B is the peak flux density, K_h , K_{eddy} , α , β are specific to the type of material and found out using curve fitting techniques. To calculate the total stator core losses from (2.27), the total weight of the stator core is multiplied by W_{FE} in (2.27). This equation can also be applied to calculate the core losses of the stator yoke and stator tooth separately. It is to be noted that the rotor core losses of a synchronous machine can be neglected. This is because the rotor of a WFSM is rotating at a synchronous speed, and induced currents are only caused by the harmonic components. Hence, it is negligible in calculating the total machine's core losses.

2.2.5 Verification of Results with FEA Data

A simulation model including loss modeling of WFSM is developed using mathematical models discussed in the previous sections using (2.1) -(2.18). Fig. 2.5(a) shows the torque-speed input profile given as input for both simulation and FEA calculations. As seen in the figure, various torque-speed profiles are chosen based on various stator current values up to rated current. The maximum torque is around 225 Nm and base speed is around 3,000 rpm. Fig. 2.5(b) shows the difference in torque between the simulations and the FEA. The difference in torque approximately up to 1 Nm. These differences might be seen because of the thermal effects that are not included in the developed machine model.

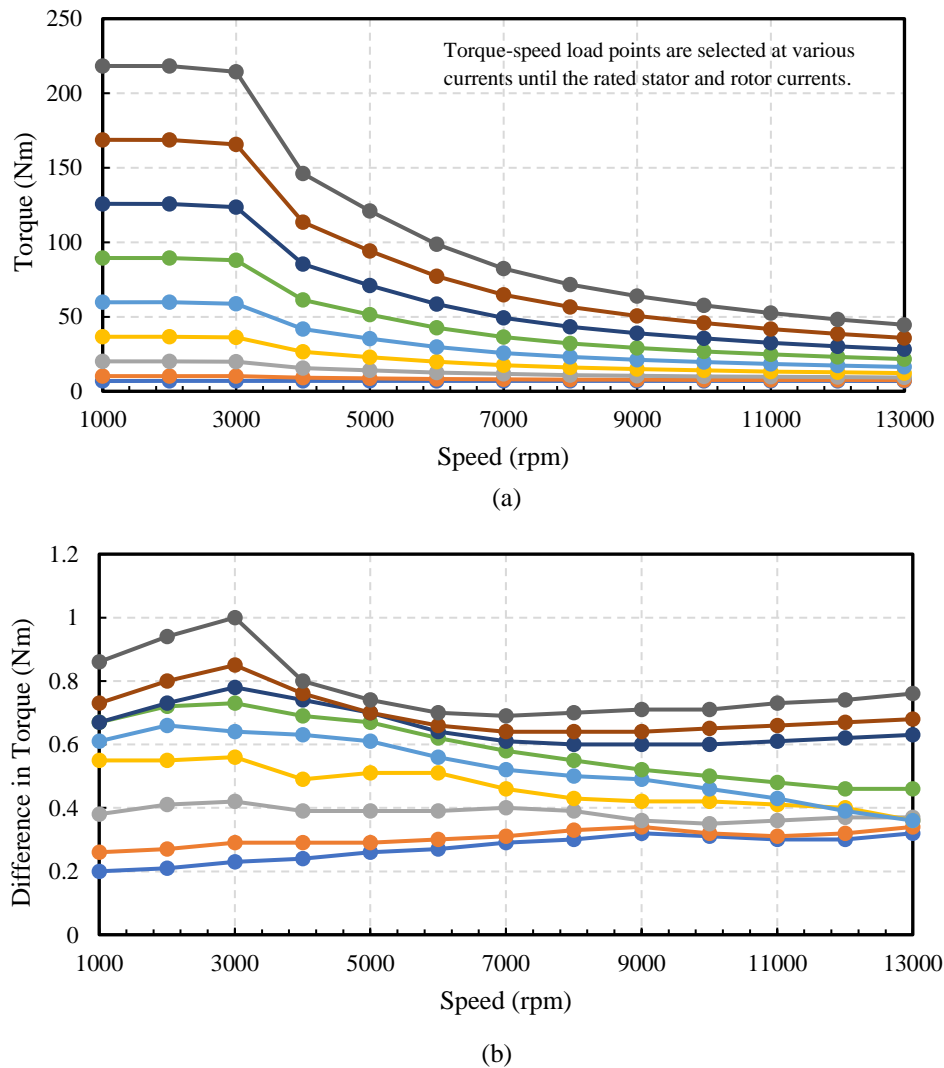


Fig. 2.5. (a) Torque-speed profile as input to simulation and FEA. (b) difference in torque.

2.3 Modeling of Three-Phase Inverter

A three phase two level VSI is crucial in supplying a three-phase voltage to be applied on the stator of the WFSM. For the rotor of the WFSM, a rotor converter circuit is used in supplying DC voltage for the field circuit. Modeling of the rotor converter and simulation results are seen in the following sub-section. Both the inverter and the converter share the same high voltage DC of the battery. In a VSI, there are a total of 6 switches with anti-parallel diodes. These switches can be either IGBTs or MOSFETs, according to the application. These switches are conventionally named S_1 - S_6 switches. Fig. 2.6 shows the configuration of an IGBT three-phase inverter connected to a WFSM. These kinds of inverters are controlled through a space vector pulse width modulation (SVPWM) or sine pulse width modulation (SPWM) modulation technique [19]-[22]. In closed-loop control, the feedback currents are used to compare with the reference signals to generate control signals. These control signals are further compared to a comparator signal to generate digital PWM gate signals. As seen in (2.29), the SVPWM technique is 115% more efficient than the SPWM.

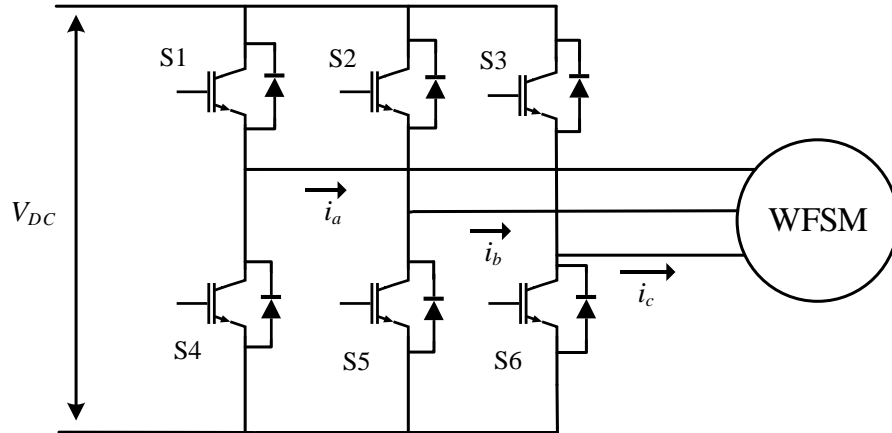


Fig. 2.6. Three-phase two-level voltage source inverter schematic diagram.

The output line-to-line RMS voltage of the inverter, when modulated in SPWM and SVPWM, is given as follows:

$$V_{LL-rms} = 0.612 * m_a * V_{DC} \text{ for SPWM} \quad (2.28)$$

$$V_{LL-rms} = 0.612 * 1.15 * m_a * V_{DC} \text{ for SVPWM} \quad (2.29)$$

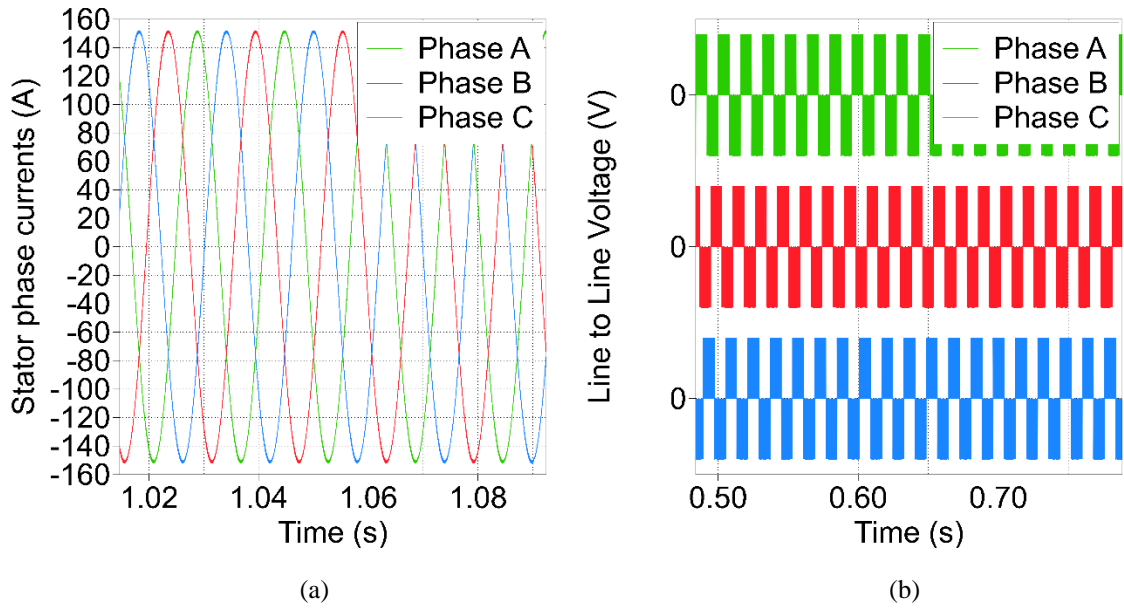


Fig. 2.7. Three-phase two-level voltage source inverter simulations. (a) Three-phase stator phase currents. (b) Three-phase line-to-line voltage.

Figure 2.7 shows the simulation results of a 2-level VSI three-phase inverter. Wherein, Fig. 2.7(a) shows the three-phase stator phase currents, and Fig. 2.7(b) shows the three-phase line-to-line voltages.

2.3.1 Voltage and Current Characteristics of IGBT and Diode

As mentioned in Chapter 1, to develop a maximum system efficiency control algorithm, computing the losses of the stator inverter and rotor converter is crucial.

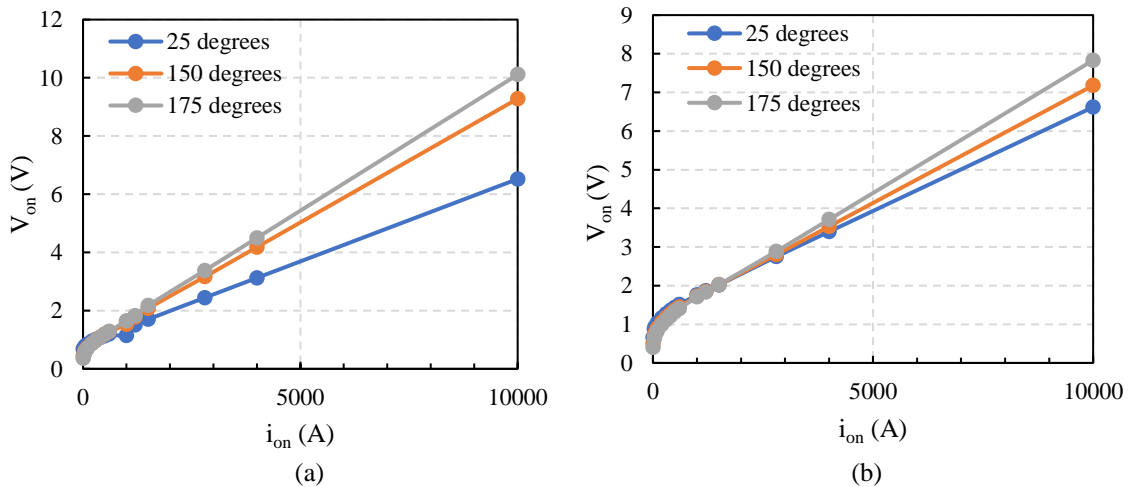


Fig. 2.8. Voltage and current characteristics at $V_{GE} = 15V$. (a) IGBT. (b) Diode.

To accurately calculate the conduction and switching losses of the three-phase inverter, an accurate representation of thermal characteristics is required. The main thermal characteristics of an IGBT/MOSFET or any other power electronic semi-conductors are: (i) voltage-current characteristics, and (ii) energy characteristics. The voltage current characteristics are used to calculate the conduction losses during the device is in ON condition. As shown in Figs. 2.8(a) and (b), the voltage-current characteristics from the manufacturer's datasheet are used to represent the V - I characteristics of the IGBT and the diode. These characteristics are the same for all the switches in the inverter. The above-shown V - I characteristics are for multiple operating temperatures and at 15 V of V_{GE} .

2.3.2 Switching Energy Characteristics of IGBT

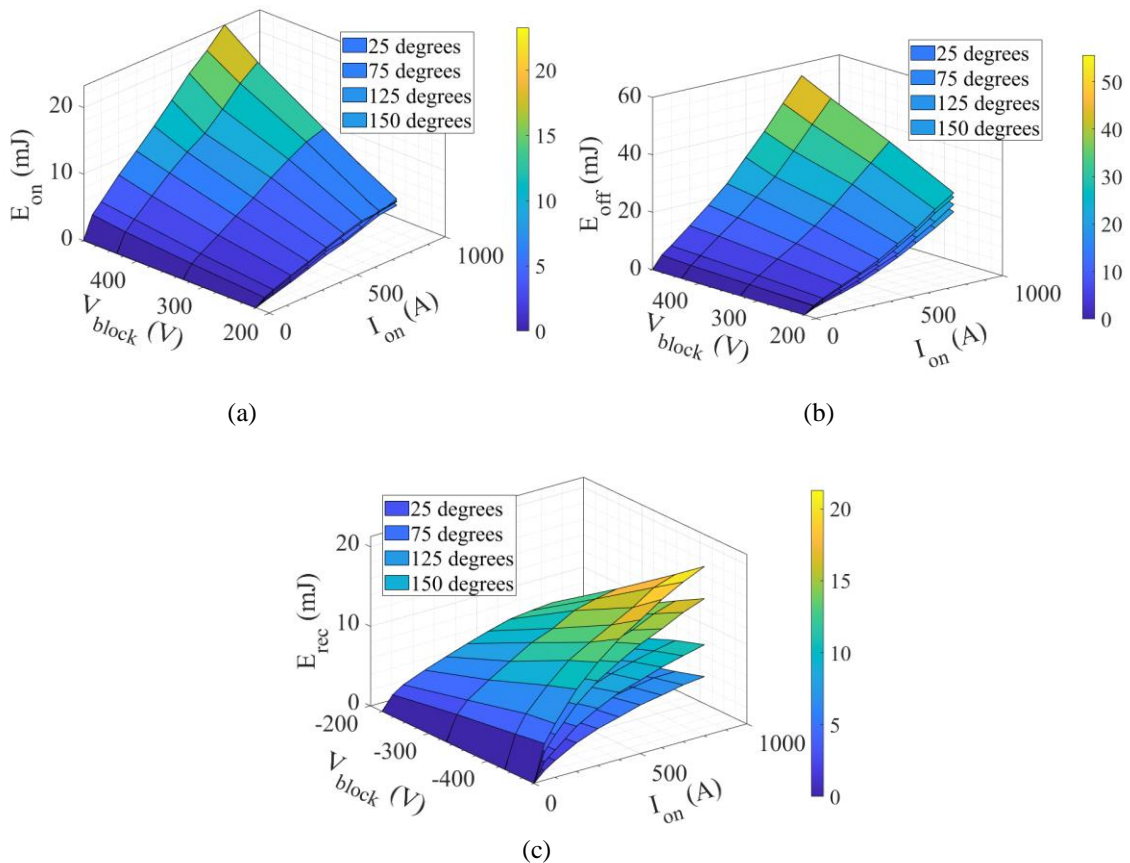


Fig. 2.9. Switching energy characteristics. (a) E_{ON} of IGBT. (b) E_{OFF} of IGBT. (c) E_{REC} of diode.

The switching energy characteristics of the IGBT and the diode are represented in Fig. 2.9. Fig. 2.9(a) shows the energy dissipated by the IGBT while switching ON. Fig. 2.9(b) shows the switch OFF energy of IGBT. Fig. 2.9(c) describes the energy dissipated during reverse recovery of the diode. The switching energy dissipated also depends on the blocking voltage and the current, respectively.

2.3.3 Inverter Loss Modeling

The main losses contributing to a three-phase IGBT based inverters are classified into two categories. These are conduction and switching losses of IGBTs and anti-parallel diodes. To precisely estimate the conduction and switching losses, an analytical model is used which includes the effects of sensitive inverter parameters such as voltage-current characteristics, turn-on, and turn-off energy characteristics, conductive ON-state resistance, etc. [23], [24]. The parameters used in the model are shown in Figs. 2.8 and 2.9 as given by the device manufacturer. The equations for the conduction and switching losses are given as follows [25]: The loss modeling equation can be applied to most of the power electronic semiconductor switches. However, the thermal characteristics vary accordingly.

$$P_{cond} = \frac{1}{T_s} \int_0^{T_s} [R_{ON}(t) * i_c^2(t)] dt \quad (2.30)$$

$$P_{sw} = [E_{ON}(t) + E_{OFF}(t) + E_{rec}(t)] * f_{sw} \quad (2.31)$$

where $R_{ON}(t)$ is the on-state resistance, and $i_c(t)$ is the collector current, E_{ON} and E_{OFF} , are the energy dissipated during ON and OFF for the IGBT. E_{rec} is the energy dissipated during the reverse recovery of the diode.

2.4 Modeling of Conductive Excitation System

The conductive excitation system based WFSM has two sets of brushes and sliprings for supply DC power to the rotor. The high-voltage DC bus is shared between the stator inverter and the rotor converter. Hence, the rotor converter/buck converter converts the high-voltage DC to controllable low voltage DC. Therefore, as shown in-

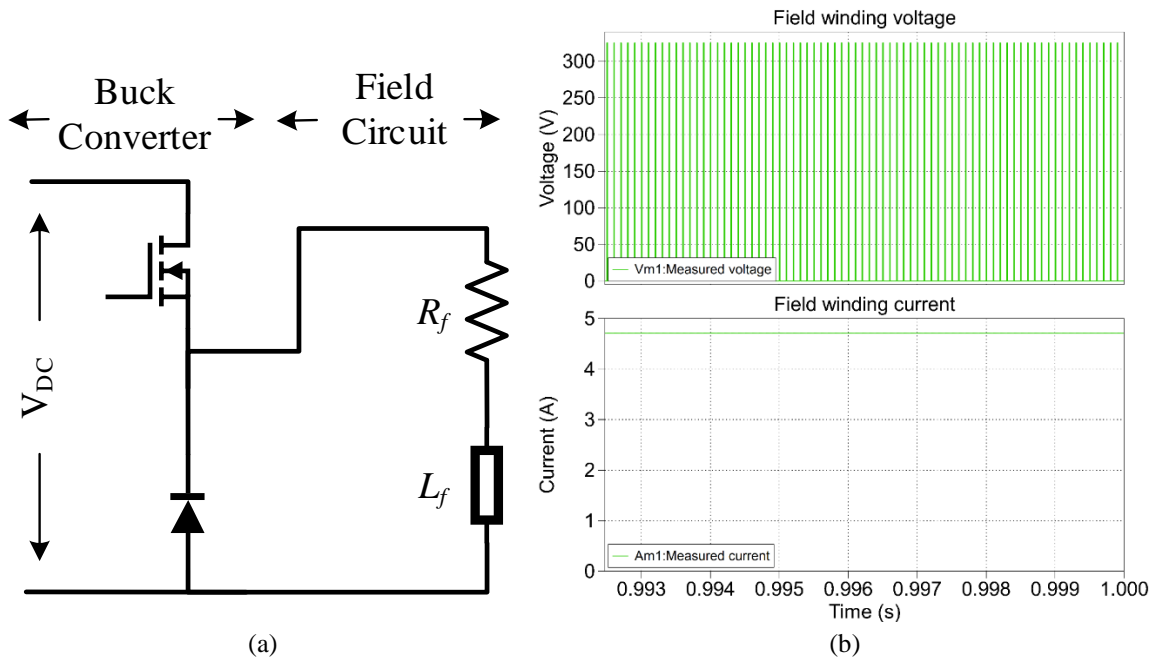


Fig. 2.10. Buck converter for conductive rotor excitation system. (a) Buck converter schematic diagram. (b) Simulation results showing field excitation voltage and current.

Figure. 2.10(a), the buck converter is connected to the shared high-voltage DC supply. Only the top IGBT is switched to generate a pulsed DC voltage as shown in Fig. 2.10(b). The DC field excitation current flows into the rotor field circuit along the field winding resistance (R_f) and field winding inductance (L_f). The buck converter is controlled by PWM modulation technique, and the output voltage is controlled by varying the duty ratio (D) from 0-1. The buck converter is also switched at the same switching frequency rate of 10kHz.

2.5 Modeling of Inductive Power Transfer System

Unlike the brushed conductive excitation system, an Inductive Power Transfer (IPT) based excitation system does not have a set of brushes and slip rings. As shown in Fig. 2.21(a), the IPT system is divided into two parts, namely, stationary/primary and rotating/secondary sides. The primary side has a single-phase inverter connected to the shared high-voltage DC bus supply. The single-phase inverter feeds the AC voltage as shown in Fig. 2.21(c) to the rotating transformer. On the secondary side, there is a rotating single-phase rectifier circuit that is connected to the rotor field winding circuit. The load current and the secondary voltage, current, are shown in Fig. 2.21(b), (d).

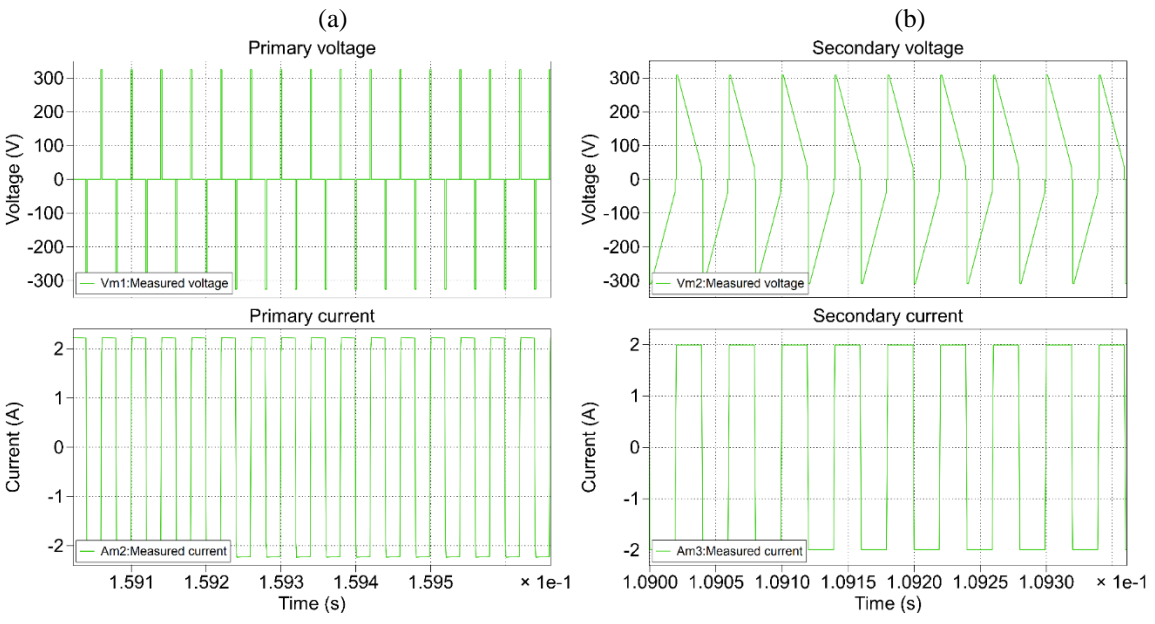
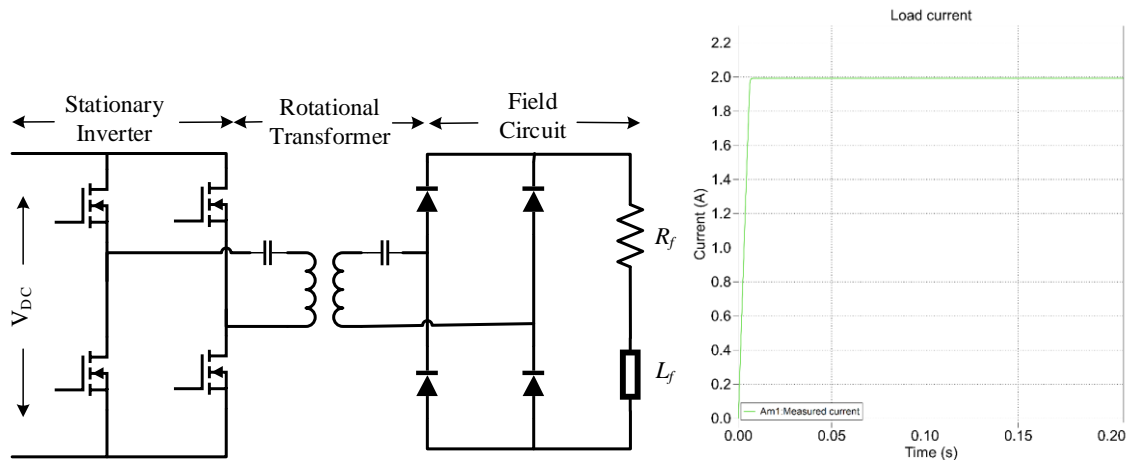


Fig. 2.11. Inductive power transfer excitation system. (a) IPT system schematic diagram. (b) Load current. (c) Primary voltage and current. (d) Secondary voltage and current.

The IPT circuit is controlled by phase shift closed-loop controller. This is because to supply always an AC voltage to the rotating transformer to avoid saturation. Therefore, the positive and negative volt-sec should always be the same in the primary voltage feeding into the rotating transformer. The power transfer from the stationary to rotating side is based on resonance. The stationary circuit resonates at a high frequency, usually from 15 kHz to 80 kHz based on the distance between and the circuit parameters. The IPT has many advantages due to the absence of brushes. The main advantages are the absence of wear and tear on brushes, maintenance, sparking effects, etc. Due to the presence of more

switches and operating at high frequencies due to resonant frequency, the IPT circuit losses are usually high compared to the buck converter. Hence, calling for the maximum overall system efficiency per ampere control.

2.6 Conclusion

In this chapter, mathematical modeling of WFSM, three-phase inverter, and various rotor excitation system as discussed. The advantages of the IPT system over the conductive excitation system are also elaborated. The loss-modeling of the WFSM and inverter is also discussed. In the chapter, closed-loop controls involving current and speed controller are demonstrated. The closed-loop controls are designed based on the developed models in this chapter.

2.7 References

- [1] B. H. Kenny and R. D. Lorenz, "Stator- and rotor-flux-based deadbeat direct torque control of induction machines," *IEEE Trans. Ind. Appl.*, vol. 39, no. 4, pp. 1093–1101, Jul./Aug. 2003.
- [2] J. S. Lee, C. H. Choi, J. K. Seok, and R. D. Lorenz, "Deadbeat-direct torque and flux control of interior permanent magnet synchronous machines with discrete time stator current and stator flux linkage observer," *IEEE Trans. Ind. Appl.*, vol. 47, no. 4, pp. 1749–1758, Jul./Aug. 2011.
- [3] N. T. West and R. D. Lorenz, "Digital implementation of stator and rotor flux-linkage observers and a stator-current observer for deadbeat direct torque control of induction machines," *IEEE Trans. Ind. Appl.*, vol. 45, no. 2, pp. 729–736, Mar./Apr. 2009.
- [4] R. H. Park, "Two-Reaction Theory of Synchronous Machines—Generalized Method of Analysis—Part I," *AIEE Trans.* vol. 48, July 1929, pp. 716 – 727.
- [5] P. C. Krause, O. Wasynczuk, and S. Sudhoff, *Analysis of Electric Machinery and Drive Systems*. Wiley-IEEE Press, 2002
- [6] R. Krishnan, *Permanent Magnet Synchronous and Brushless DC Motor Drives*. CRC Press, 2010
- [7] Y. Nie, I. P. Brown, and D. C. Ludois, "Low switching frequency deadbeat–direct torque and flux control of wound field synchronous machines," in *Proc. 2018 IEEE Energy*

- Conversion Congress and Exposition (ECCE)*, 2018, pp. 6542–6549, doi: 10.1109/ECCE.2018.8557780.
- [8] T. Wisniewski, J. -C. Vannier, B. Lorcet, J. Saint-Michel, and X. Jannot, "Extended dq modeling of wound-rotor synchronous machines with dampers for transient analysis," in *Proc. 2017 18th International Symposium on Electromagnetic Fields in Mechatronics, Electrical and Electronic Engineering (ISEF) Book of Abstracts*, 2017, pp. 1-2, doi: 10.1109/ISEF.2017.8090768.
- [9] P. Winzer, J. Richter, and M. Doppelbauer, "Dynamic control of generalized electrically excited synchronous machines using predictive flux control," in *Proc. IECON 2016 - 42nd Annual Conference of the IEEE Industrial Electronics Society*, 2016, pp. 2772-2777, doi: 10.1109/IECON.2016.7793666.
- [10] Y. Kim and K. Nam, "Copper-Loss-Minimizing Field Current Control Scheme for Wound Synchronous Machines," *IEEE Transactions on Power Electronics*, vol. 32, no. 2, pp. 1335-1345, Feb. 2017, doi: 10.1109/TPEL.2016.2547953.
- [11] A. Balamurali, A. Kundu, V. Kurrumsetty, L. V. Iyer, and N. C. Kar, "Coupled Numerical and Circuit Model Considering Stator and Field Winding Flux Linkage for Loss Minimization Control of Wound Field Synchronous Machines," Presented at the IEEE Joint MMM-Intermag Conference, New Orleans, USA, January 2022.
- [12] C. Cavallaro, A. O. Di Tommaso, R. Miceli, A. Raciti, G. R. Galluzzo, and M. Trapanese, "Efficiency enhancement of permanent-magnet synchronous motor drives by online loss minimization approaches," *IEEE Transactions on Industrial Electronics*, vol. 52, no. 4, pp. 1153-1160, Aug. 2005, doi: 10.1109/TIE.2005.851595.
- [13] J. O. Estima, and A. J. Marques Cardoso, "Efficiency Analysis of Drive Train Topologies Applied to Electric/Hybrid Vehicles," *IEEE Transactions on Vehicular Technology*, vol. 61, no. 3, pp. 1021-1031, March 2012, doi: 10.1109/TVT.2012.2186993.
- [14] C. Dutta and S. M. Tripathi, "Comparison between conventional and loss d-q model of PMSM," in *Proc. International Conference on Emerging Trends in Electrical Electronics & Sustainable Energy Systems (ICETEESES)*, 2016, pp. 256-260, doi: 10.1109/ICETEESES.2016.7581370.

- [15] Allen N, Lai HC, Rodger D, and Leonard PJ, "On the validity of two A-/spl psi/ finite element formulations for modelling eddy current problems with velocity" *IEEE Trans. Magnetics*, vol. MAG-34, no. 5, September 1998, pp. 2535-2538.
- [16] Hameyer K and Belmans R, *Numerical modelling and design of electrical machines and devices*. WIT Press, 1999
- [17] S. J. Salon, *Finite element analysis of electrical machines*. Norwell, MA: Kluwer Press, 1995.
- [18] "Electromagnetic Losses Modelling in Motor-CAD," Jun 2021, Accessed on Nov. 1, 2022. [Online]. Available: https://www.cadfem.net/fileadmin/user_upload/05-cadfem-informs/resource-library/2021_popescu_CADFEM_Techday2_electromagnetic_losses_modelled_in_motor_cad.pdf
- [19] X. Zhang, X. Wu, C. Geng, X. Ping, S. Chen, and H. Zhang, "An Improved Simplified PWM for Three-Level Neutral Point Clamped Inverter Based on Two Level Common-Mode Voltage Reduction PWM," *IEEE Trans. Power Electronics*, vol. 35, no. 10, pp. 11143-11154, Oct. 2020.
- [20] O. López, D. Dujic, M. Jones, F. D. Freijedo, J. Doval-Gandoy, and E. Levi, "Multidimensional Two-Level Multiphase Space Vector PWM Algorithm and Its Comparison with Multifrequency Space Vector PWM Method," *IEEE Trans. Industrial Electronics*, vol. 58, no. 2, pp. 465-475, Feb. 2011.
- [21] M. A. Al-Hitmi, S. Moinoddin, A. Iqbal, K. Rahman, and M. Meraj, "Space Vector vs. Sinusoidal Carrier-Based Pulse Width Modulation for a Seven-Phase Voltage Source Inverter," *CPSS Trans. Power Electronics and Applications*, vol. 4, no. 3, pp. 230-243, Sept. 2019.
- [22] R. A. Villarreal-Ortiz, M. Hernandez-Angeles, C. R. Fuerte-Esquivel, and R. O. Villanueva-Chavez, "Centroid PWM Technique for Inverter Harmonics Elimination," *IEEE Trans. Power Delivery*, vol. 20, no. 2, pp. 1209-1210, April 2005.
- [23] A. Kundu, P. Korta, A. Balamurali, L. V. Iyer, and N. C. Kar, "Improved Electro-Thermal Model Incorporating Device Aging Effect Towards Accurate Temperature Tracking in Electric Motor Drives," in *Proc. 24th International Conference on Electrical Machines and Systems (ICEMS)*, 2021, pp. 1037-1042, doi: 10.23919/ICEMS52562.2021.9634576.

[24] M. Bonisławski and M. Hołub, "Averaged inverter loss estimation algorithm," in *Proc. 18th European Conference on Power Electronics and Applications (EPE'16 ECCE Europe)*, 2016, pp. 1-9, doi: 10.1109/EPE.2016.7695567.

[25] D. Graovac, M. Pürschel, and K. Andreas, "MOSFET power losses calculation using the data- sheet parameters," *Infineon Technol. Application Note*, vol 1.1, pp. 1–23, July 2006.

CHAPTER 3

MAXIMUM SYSTEM EFFICIENCY PER AMPERE CONTROL OF INDUCTIVE POWER TRANSFER-BASED WFSM E-DRIVE SYSTEM

3.1 Introduction

Maximizing the overall system efficiency is given more importance when compared to maximizing the efficiency of discrete components separately, such as the motor or inverter, which are a part of the overall system. Therefore, this chapter discusses the design and modeling of the closed-loop proportional-integral (PI) controller for direct, quadrature, and field axis control loops. Design and modeling of current and speed closed-loop controls are also discussed for IPT-based WFSM. A maximum system efficiency per ampere control algorithm is developed to address maximizing the overall system efficiency based on the loss models of WFSM, inverter, and IPT converter developed in chapter 2.

3.2 Design and Modeling of Closed-Loop PI Controllers Using Pole-Zero Cancellation Technique

The design and modeling of closed-loop based on PI controllers are designed according to the open-loop transfer function of the system. The mathematical open-loop transfer functions of the WFSM model are derived from (3.1)-(3.6). The selection of gains of the proportional (K_p) and integral (K_i) terms is based on the pole-zero cancellation technique. This technique is explained in detail in the following subsections. Since the modeling of the WFSM is developed in the rotor reference or $dq0$ frame of reference, the pole-zero cancellation technique is used for all the three axes, namely direct, quadrature, and field axis, separately for designing a closed-loop current control [1]-[4].

$$v_{ds} = r_s i_{ds} + \frac{d\lambda_{ds}}{dt} - \omega_r \lambda_{qs} \quad (3.1)$$

$$v_{qs} = r_s i_{qs} + \frac{d\lambda_{qs}}{dt} + \omega_r \lambda_{ds} \quad (3.2)$$

$$v_{fr} = r_f i_{fr} + \frac{d\lambda_{fr}}{dt} \quad (3.3)$$

where,

$$\lambda_{ds} = L_d i_{ds} + L_m i_{fr} \quad (3.4)$$

$$\lambda_{qs} = L_q i_{qs} \quad (3.5)$$

$$\lambda_{fr} = L_f i_{fr} + \frac{3}{2} L_m i_{ds} \quad (3.6)$$

3.2.1 Design of PI Controller for Direct Axis

The design of proportional-integral (PI) controllers is developed on the basis of the pole-zero cancellation method. For developing the closed-loop current control of the direct axis, the pole of the direct axis is calculated from the voltage equations (3.1) -(3.6). Substituting (3.4) and (3.5) in (3.1), we get:

$$v_{ds} = r_s i_{ds} + L_d p i_{ds} + L_m p i_{fr} - \omega_r L_q i_{qs} \quad (3.7)$$

$$v_{ds} - L_m p i_{fr} + \omega_r L_q i_{qs} = (r_s + s L_d) i_{ds} \quad (3.8)$$

$$i_{ds} = \frac{1}{(r_s + s L_d)} * (v_{ds} - L_m p i_{fr} + \omega_r L_q i_{qs}) \quad (3.9)$$

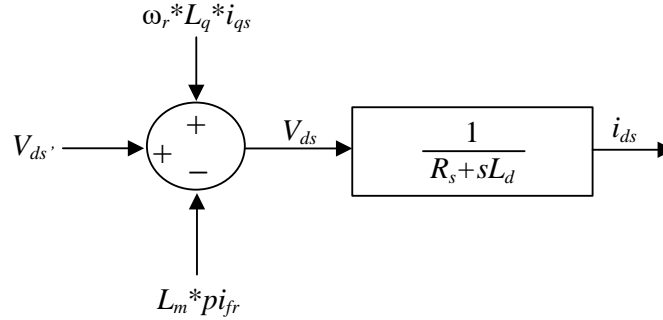


Fig. 3.1. Direct axis block diagram in Laplace domain.

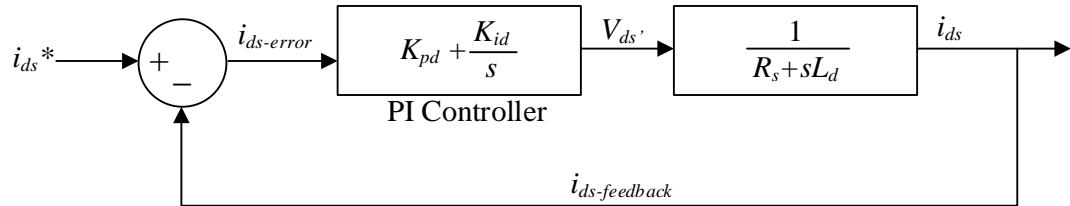


Fig. 3.2. Direct axis closed-loop current control block diagram in Laplace domain.

Figure 3.1 shows the block diagram of the direct axis in the Laplace domain. The transfer function of the PI controller is given as $K_{pd} + K_{id}/s$. According to the pole-zero cancellation technique, the zero of the PI controllers should be placed on the pole of the direct-axis's transfer function. From Fig. 3.2, the overall transfer function $G(s)$, can be derived and as follows in the equation (3.10).

$$G(s) = \left(K_{pd} + \frac{K_{id}}{s} \right) * \left(\frac{1}{R_s + sL_d} \right) \quad (3.10)$$

Re-writing (3.10) into (3.11)

$$G(s) = \left(\frac{K_{pd} \left(s + \frac{K_{id}}{K_{pd}} \right)}{s} \right) * \left(\frac{1}{L_d \left(s + \frac{r_s}{L_d} \right)} \right) \quad (3.11)$$

The condition for canceling the pole-zero from (3.11) is given in (3.12). Substituting (3.12) in (3.11) will give (3.13).

$$\frac{K_{id}}{K_{pd}} = \frac{R_s}{L_d} \quad (3.12)$$

$$G(s) = \frac{K_{pd}}{sL_d} \quad (3.13)$$

$$G(s) = \frac{1}{1 + s\tau} \quad (3.14)$$

Comparing (3.13) with the closed-loop transfer function with unity feedback (3.14), we get the time constant, $\tau = L_d/K_{pd}$. The bandwidth of the controller for the direct axis is fixed as one-tenth of the inverter switching frequency i.e., 10 kHz [5]. Therefore, the bandwidth of the controller is 1,000 Hz. The time constant τ is given in (3.15).

$$\tau = \frac{1}{2 * \pi * 1000} \text{ sec/ rad} \quad (3.15)$$

From (3.15) and $\tau=L_d/K_{pd}$, we get,

$$K_{pd} = (L_d * 2 * \pi * 1000) \quad (3.16)$$

From (3.12) and (3.16), K_{id} is given as,

$$K_{id} = K_{pd} * \frac{R_s}{L_d} \quad (3.17)$$

$$K_{id} = (R_s * 2 * \pi * 1000) \quad (3.18)$$

Equations (3.16) and (3.18) are the gains of proportional and integral terms of the PI controller. Where R_s is the stator phase resistance, and L_d is the d -axis inductance at the rated currents.

3.2.2 Design of PI Controller for Quadrature Axis

The design of the PI controller for the quadrature axis is developed in the same procedure as followed for the direct axis closed-loop controller. For developing the closed-loop current control of the direct axis, the pole of the direct axis is calculated from the voltage equations (3.1)-(3.6). Substituting (3.4) and (3.5) in (3.2), we get:

$$v_{qs} = r_s i_{qs} + L_q p i_{qs} + \omega_r L_{ds} i_{ds} + \omega_r L_m i_{fr} \quad (3.19)$$

$$v_{qs} - \omega_r L_{ds} i_{ds} - \omega_r L_m i_{fr} = (r_s + sL_q) i_{qs} \quad (3.20)$$

$$i_{qs} = \frac{1}{(r_s + sL_q)} * (v_{qs} - \omega_r L_{ds} i_{ds} - \omega_r L_m i_{fr}) \quad (3.21)$$

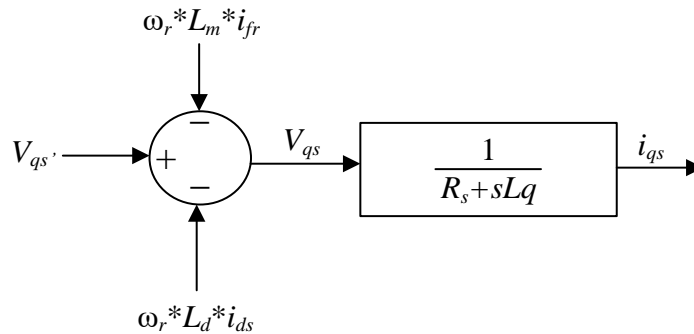


Fig. 3.3. Quadrature axis block diagram in Laplace domain.

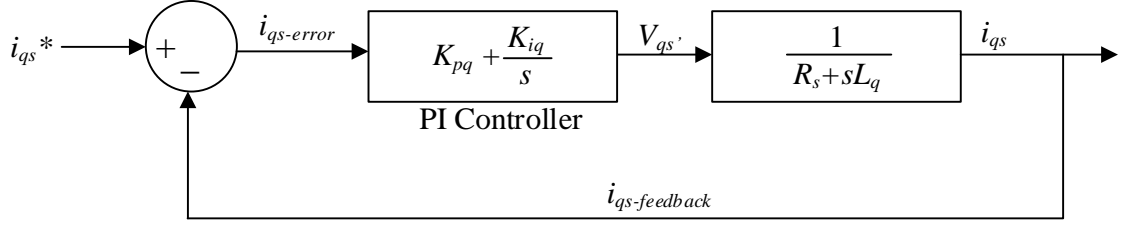


Fig. 3.4. Quadrature axis closed-loop current control block diagram in Laplace domain.

Figure 3.3 shows the block diagram of the quadrature axis in the Laplace domain. The transfer function of the PI controller is given as $K_{pq} + K_{iq}/s$. The same procedure is followed as that of direct axis closed-loop control. Fig. 3.4 shows the closed-loop current control block diagram of the quadrature axis in the Laplace domain. The expressions for the gains of proportional and integral terms of the controller for the quadrature axis are derived in (3.22)–(3.25).

$$\tau = \frac{1}{2 * \pi * 1000} \text{sec/ rad} \quad (3.22)$$

From equation (3.15) and the time constant for the quadrature axis, $\tau = L_q/K_{pq}$,

$$K_{pq} = (L_q * 2 * \pi * 1000) \quad (3.23)$$

From (3.12) and (3.16), K_{iq} is given as,

$$K_{iq} = K_{pq} * \frac{R_s}{L_q} \quad (3.24)$$

$$K_{iq} = (R_s * 2 * \pi * 1000) \quad (3.25)$$

Equations (3.23) and (3.25) are the gains of proportional and integral terms of the PI controller. Where R_s is the stator phase resistance, and L_q is the quadrature axis inductance at the rated currents.

3.2.3 Design of PI Controller for Field Axis

For developing a closed-loop current control for the field axis, the voltage equation (3.6) is substituted in the equation (3.3) we get,

$$v_{fr} = r_f i_{fr} + L_f p i_f + \frac{3}{2} L_m p i_d \quad (3.26)$$

$$v_{fr} - \frac{3}{2} L_m p i_d = (r_f + s L_f) i_f \quad (3.27)$$

$$i_f = \frac{1}{(r_f + s L_f)} * \left(v_{fr} - \frac{3}{2} L_m p i_d \right) \quad (3.28)$$

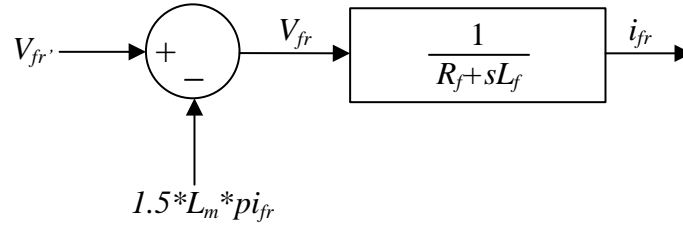


Fig. 3.5. Field axis block diagram in Laplace domain.

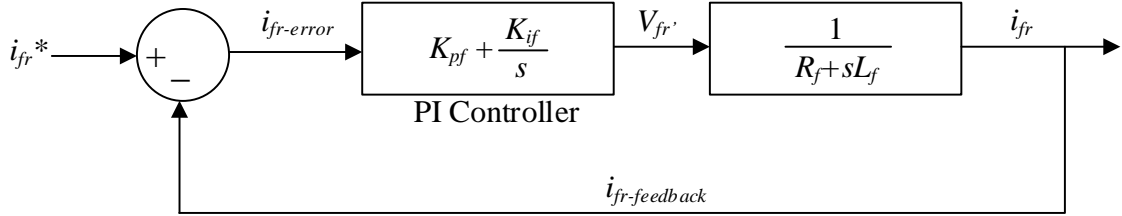


Fig. 3.6. Field axis closed-loop current control block diagram in Laplace domain.

Figure. 3.5 shows the block diagram of the field axis in Laplace domain, and Fig. 3.6 shows the field axis closed-loop current control block diagram in the Laplace domain.

The PI controller for the field axis is derived in the same procedure as that of direct and quadrature axis. However, the bandwidth of the field axis controller is fixed at one-fifth of the rotor converter switching frequency. Therefore, the bandwidth of the controller is 2,000 Hz. The time constant τ is given in equation (3.29).

$$\tau = \frac{1}{2 * \pi * 2000} \text{sec/ rad} \quad (3.29)$$

From (3.15), we get the time constant for field axis as $\tau = L_f / K_{pf}$, K_{pf} can be written as,

$$K_{pf} = (L_f * 2 * \pi * 2000) \quad (3.30)$$

From (3.12) and (3.16), K_{if} is given as,

$$K_{if} = K_{pf} * \frac{R_f}{L_f} \quad (3.31)$$

$$K_{if} = (R_f * 2 * \pi * 2000) \quad (3.32)$$

Equations (3.30) and (3.32) are the gains of proportional and integral terms of the PI controller. Where R_f is the field winding resistance, and L_f is the field winding inductance at the rated currents.

3.3 Design and Modeling of Closed-Loop Controls Based on Feedback

In this section the modeling of closed-loop controls based on feedback is discussed for the following loops: (i) closed-loop current-control, and (ii) closed-loop speed control. These following closed-loop control topics are a sub-part and are derived from the concepts of cascaded control of a motor drive [6] and is represented in Fig. 3.7. The electrical system in the figure consists of WFSM, inverter, etc. The focus on the cascaded motor control is limited to only until the speed control. As seen in the figure, the speed control of the machine is seen as the outer loop of the inner current control. Therefore, the above-designed PI controllers for the three axes are implemented to design a closed-loop current control. The implementation of both closed-loop controls is discussed in the next subsection.

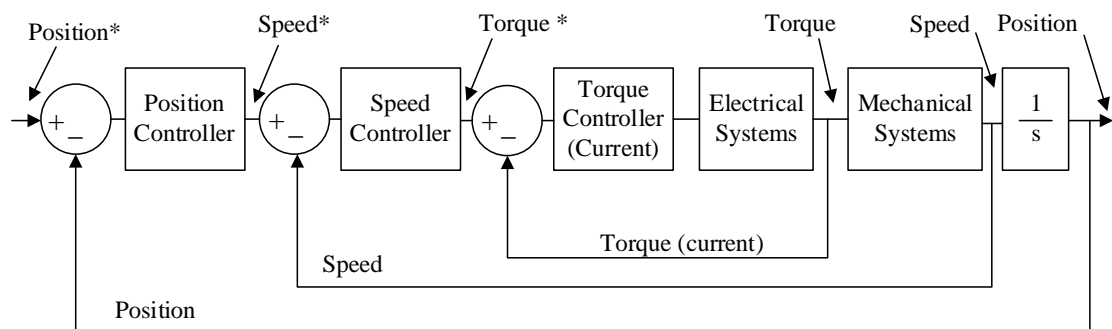


Fig. 3.7. Cascaded control of a motor drive.

3.3.1. Design of Closed-Loop Current Control

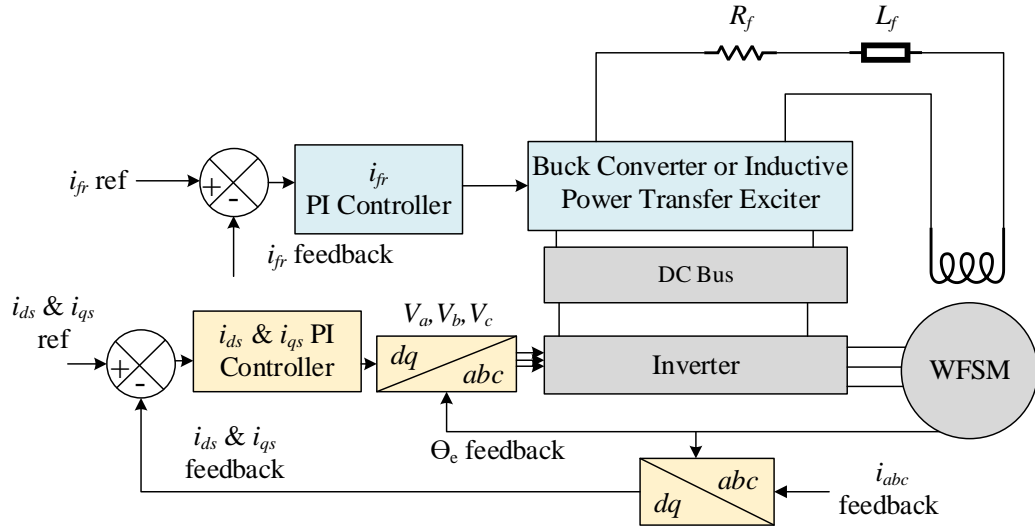


Fig. 3.8. Block diagram of WFSM closed-loop current control.

The complete block diagram of WFSM closed-loop current control for WFSM is shown in Fig. 3.8. The developed PI controllers are employed in all the three axes: direct, quadrature, and field axis as seen in the figure. The stator phase currents, and the rotor position are used as the feedback signals for Park's and inverse Park's transformations. The error current signals from the reference and feedback signals are directed to the PI controllers. The output voltage from the PI controllers is used as control signals to generate the SPWM gate signals by comparing it to the carrier reference signals. The closed-loop current control is performed on the WFSM by rotating the rotor at a constant speed that lies inside the torque-speed envelope of the machine. Then, the reference currents are commanded to verify the robustness and stability of the current controller and the performance of the machine by measuring the generated torque output.

3.3.2 Design of Closed-Loop Speed Control

Figure 3.9 shows the block diagram of WFSM closed-loop speed control. As described in the cascaded control, the inner loop of the closed-loop speed control remains the same as that of closed-loop current control, as shown in the previous sub-section. The speed error signal is generated by comparing the speed reference and speed error signals. The error speed signal is fed into the speed PI controller, and the output of the PI controller

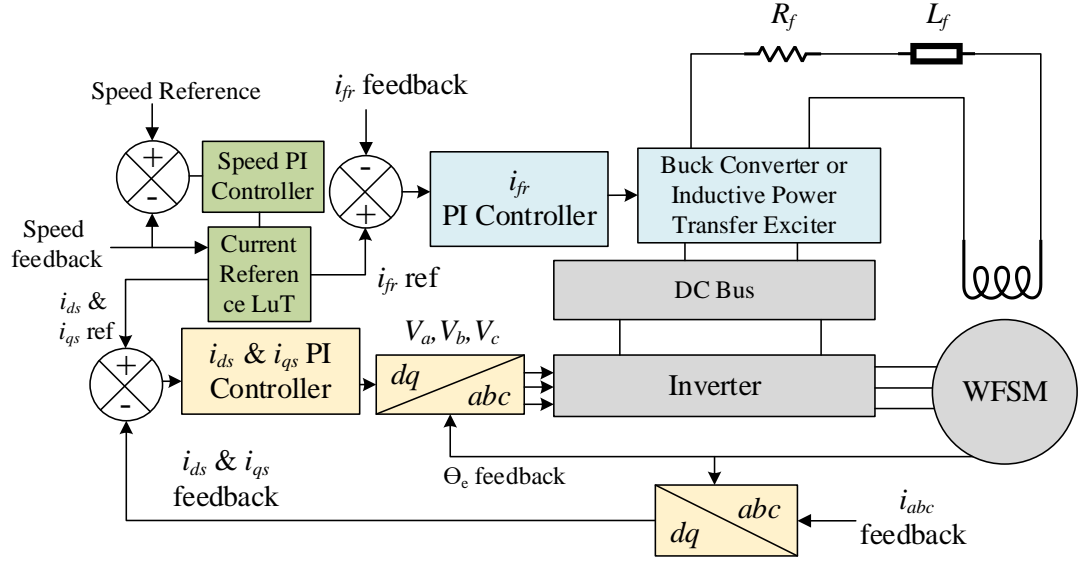


Fig. 3.9. Block diagram of WFSM closed-loop speed control.

is a torque command signal. As shown in the above figure, the torque command and speed feedback signals are used to determine the direct, quadrature, and field reference currents. The main research problem in closed-loop speed control of synchronous machines is in finding the current references based on the feedback. As seen in the block diagram, a look-up-table (LuT) is used to generate i_{dqf} reference currents for the closed-loop current controller. The LuT is essentially a three-dimensional table for all three currents based primarily on speed feedback and torque command. These reference tables can be advanced with many other factors, and the next subsection discusses regarding those intelligent control algorithms.

3.4. Comparison of Conventional Total and Rotor Loss Minimization Control Strategies

As discussed in the previous subsection, the reference direct, quadrature, and field axis current references are based on speed feedback and torque command. These reference commands can be derived either analytically or numerically. The numerical method uses a three-dimensional LuTs as it can reduce the runtime by interpolating points when compared to analytical solutions as it can consume more time due to iterative cycles [7], [8]. Moreover, deriving an analytical solution for finding the reference currents for WFSM from the voltage and torque curve intersection is difficult due to the third independent variable i.e., field axis current [9]. There are many loss minimization techniques based on

various parameters such as temperature, power factor, DC bus voltage, etc., for synchronous machine are seen in the literature [10]-[16]. However, in this section, a comparison between the two loss minimization techniques is discussed. The two-loss minimization techniques are, namely, total loss minimization (TLM) control and rotor loss minimization (RLM) control methodologies. The TLM control method focuses on minimizing the total losses of the motor, whereas the RLM method focuses on minimizing the rotor losses primarily. Both the loss minimizing control methods includes motor losses such as eddy, hysteresis, stator and rotor copper, stator and rotor back iron, and stator and rotor back iron losses are taken into consideration. The main differences in these control strategies are found in the selection of i_{ds} , i_{qs} , and i_{fr} currents for a required amount of torque and speed, considering minimal total and rotor losses. The current reference LuTs are generated for both the loss minimization control methodologies to compare the reference currents and overall losses for the same input torque-speed profile to the FEA model as input, as shown in Fig. 3.10. The torque-speed input points are chosen at various stator currents until the rated current of the WFSM.

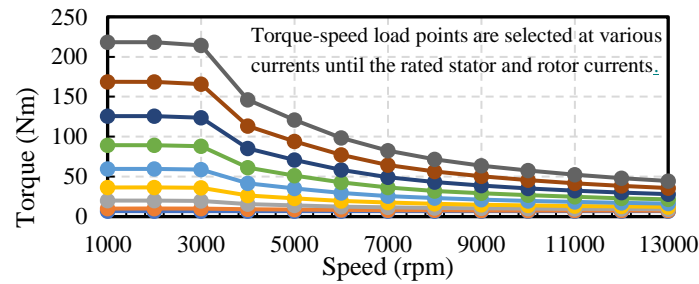


Fig. 3.10. Input torque-speed profile at various stator phase currents.

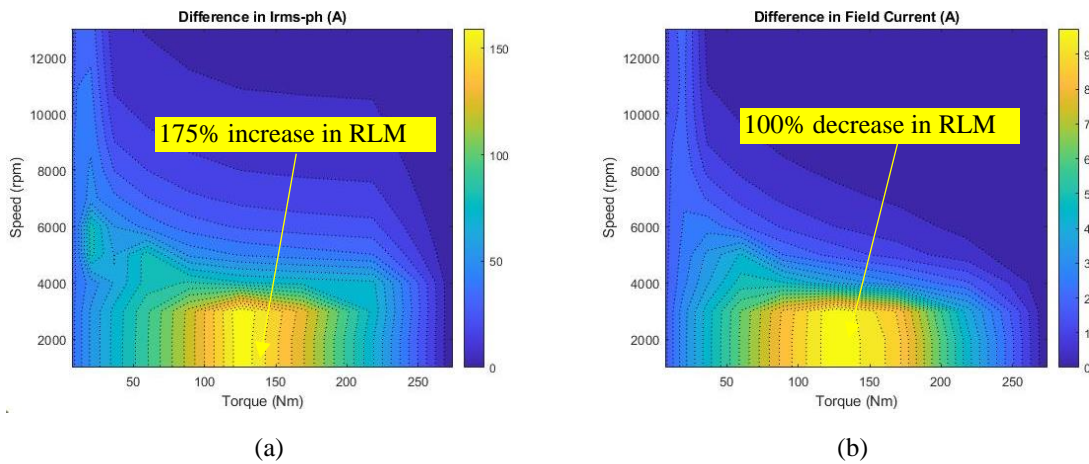


Fig. 3.11. Comparison between TLM and RLM control methodologies. (a) Difference in stator phase current. (b) Difference in field current.

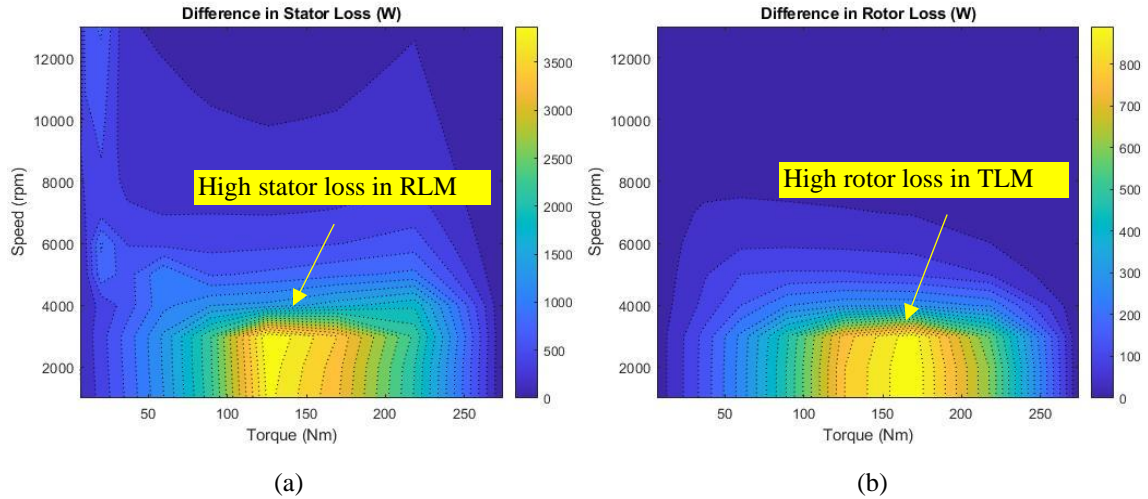


Fig. 3.12. Comparison between TLM and RLM control methodologies. (a) Difference in stator losses. (b) Difference in rotor losses.

Figure 3.11(a) shows the difference in the reference stator phase currents between TLM and RLM control methods. It is seen that the phase currents are increased by 175% in the RLM method, mainly in the lower torque and mid-torque region. This is because the RLM method focuses on minimizing the copper losses of the rotor compared to that of the stator. Figure 3.11(b) shows the difference in the reference field currents, and it is observed that there is a 100% decrease in the RLM method. This is because of the low reference field excitation current in the RLM method to decrease the rotor losses. Fig. 3.12(a) shows the difference in the stator losses alone, which includes the copper and core losses of the stator. The overall stator losses are more in the RLM method. This is because the RLM method minimizes the field current and increases the stator phase current to achieve the same torque load point by minimizing the rotor losses. Fig. 3.12(b) shows the difference in the rotor losses, that includes core and copper losses. It can be seen that rotor losses are increased in the TLM method. This is because the TLM concentrates on minimizing the stator losses while increasing the rotor field current to achieve the same load torque point. The overall motor losses are seen in Fig. 3.13, where the overall motor losses are increased by 190% in the RLM mode. Based on the following observations, the following results are derived:

- The differences among the control methods are only seen in the lower speed regions and mid-torque regions.

- The TLM control methodology has lower overall motor losses at any torque-speed load point.
- The RLM control methodology can be used to decrease the rotor losses, i.e., it can be used at times when the rotor needs to be cooled.

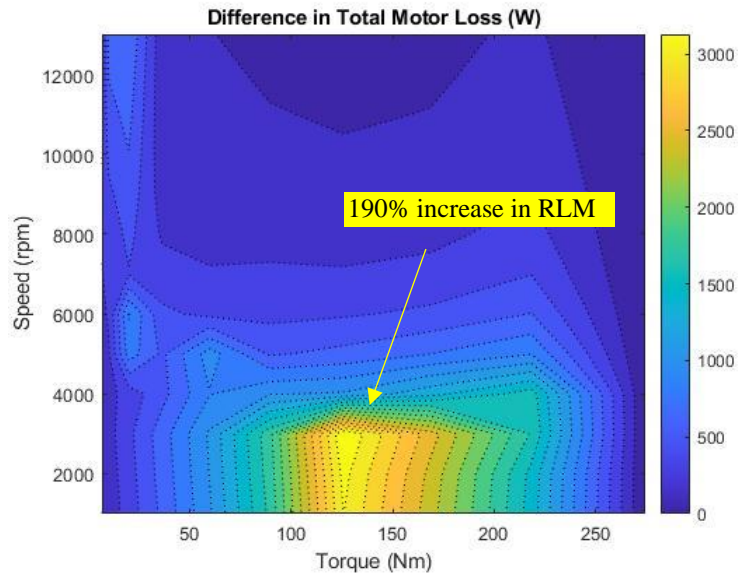


Fig. 3.13. Comparison between TLM and RLM control methodologies in total motor losses.

3.5 Maximum System Efficiency Per Ampere Control of IPT-Based WFSM Using Brute-Force Algorithm

The need of improving energy efficiency in synchronous machine is seen to be increasing in many industrial and academic EV applications [17]-[19]. Several control strategies are proposed for optimizing and maximizing the efficiency of the electric traction drives [20]-[24]. One of the most commonly used control techniques for maximum efficiency is Maximum Torque Per Ampere (MTPA) control strategy. The MTPA control strategy focuses on generating maximum torque for a minimum amount of current. However, this technique only considers the copper loss [25]. There are other loss minimization techniques that consider the core loss of the motor that includes both the stator and rotor losses. However, these control methodologies do not optimize the overall system loss or maximize the efficiency at the system level. In [25], the basic necessary features for developing a control methodology for improving efficiency are described as follows: (i) robustness of the control methodology under real-time conditions with changes

in motor parameters due to external factors, (ii) loss minimization or maximizing the efficiency at the overall system level, and (iii) lower execution time and ease of implementation. Minimizing overall system-level loss becomes more crucial in the inductive power transfer-based WFSM. This is because of the extra power electronic components in the rotor exciter. Moreover, the switching losses are to be taken into consideration because the switching frequency of the inductive power transfer-based rotor excitation system is very high due to resonant frequency, i.e., 15–80 kHz. Therefore, this thesis proposes a control methodology, namely maximum system efficiency per ampere control, that focuses on optimizing/reducing the overall system-level loss, which leads to maximizing the overall system-level efficiency. The upper hand for this control is in taking the stator inverter, the rotor's inductive power transfer-based converter, and WFSM into consideration. The working principle, control algorithm flowchart, and results are discussed in the following subsection.

3.5.1 Overall System Loss Model for Efficiency Improvement

The main objective of the proposed algorithm is to minimize the total loss and improve the overall system energy efficiency. Therefore, as the primary goal of this control algorithm is focused on improving overall efficiency, there might be cases where the loss of an internal subsystems in a system are more than the other. For example, as seen in the comparison of the total- and rotor-loss minimization control methodologies in the previous section, the total loss minimization is seen to be more efficient than the rotor-loss minimization method by 190 %. To achieve the upper hand in the efficiency compared to rotor loss minimization method, the TLM method gives more weightage to the stator losses when compared to rotor loss. Therefore, even if the rotor losses are higher in the TLM method, the overall efficiency is still high in the TLM method. In the same procedure, the maximum overall system efficiency per ampere control method focuses only on improving the overall system loss.

In the real-time application, the electric vehicle is controlled by the master controller in the electric drive in the speed control mode. As seen in Fig. 3.9, to achieve the reference speed commanded by the passenger in the car, the speed error is damped to zero by the torque proportional-integral controller. As seen in the block diagram of Fig.

3.9, the ‘current reference generator’ block generates the current references to achieve the commanded speed. Therefore, the inputs and outputs of the maximum overall system efficiency per ampere cost function are input(s) – direct, quadrature, and field axis currents; output(s) – Overall system losses including WFSM, three-phase stator inverter and rotor single phase converter for the inductive power transfer rotor excitation system. Hence, the proposed algorithm replaces the current reference generator block with a three-dimensional look-up table to provide an optimized current reference. Since the output of the cost function is the overall system loss, calculating the overall system loss would be the first step in the algorithm. The overall system loss of the IPT-based WFSM is given as shown in the equation (3.33).

$$P_{Overall System Losses} = P_{Overall WFSM Losses} + P_{Overall Inverter Losses} + P_{Overall Converter Losses} \quad (3.33)$$

$$\begin{aligned} P_{Overall System Losses} &= P_{WFSM Stator Copper} + P_{WFSM Stator Core} \\ &+ P_{WFSM Rotor Copper} + P_{WFSM Rotor Core} \\ &+ P_{Inverter Conduction Losses} + P_{Inverter Switching Losses} \\ &+ P_{Converter Conduction Losses} + P_{Converter Switching Losses} \end{aligned} \quad (3.34)$$

where,

$$P_{WFSM Stator Copper} = 3(i_d^2 + i_q^2)R_S \quad (3.35)$$

$$P_{WFSM Rotor Copper} = i_f^2 R_f \quad (3.36)$$

$$P_{WFSM Stator Core} \left[\frac{W}{Kg} \right] = K_h \cdot f \cdot B^{(\alpha+\beta \cdot B)} + 2 \cdot \pi^2 \cdot K_{eddy} \cdot f^2 B^2 \quad (3.37)$$

$$P_{Inverter Conduction Losses} = \frac{1}{T_s} \int_0^{T_s} [R_{ON}(t) * i_c^2(t)] dt \quad (3.38)$$

$$P_{Inverter Switching Losses} = [E_{ON}(t) + E_{OFF}(t) + E_{rec}(t)] * f_{sw} \quad (3.39)$$

$$P_{Converter Conduction Losses} = \frac{1}{T_s} \int_0^{T_s} [R_{ON}(t) * i_d^2(t)] dt \quad (3.40)$$

$$P_{\text{Converter Switching Losses}} = [E_{\text{ON}}(t) + E_{\text{OFF}}(t) + E_{\text{rec}}(t)] * f_{\text{sw}} \quad (3.41)$$

Therefore, the $P_{\text{Overall System Loss}}$ are computed using (3.35)–(3.41). It is important to note that the $P_{\text{WFSM rotor core}}$ losses are not included, as the rotor core loss in the WFSM are almost zero/negligible. This is because the rotor is also rotating at the synchronous speed. A very small amount of rotor core losses is generated due to the harmonics, and hence it is neglected.

3.5.2 Brute-Force Algorithm and Control Methodology Flowchart

The overall system loss for the IPT-based WFSM is computed using (3.33)–(3.41). The WFSM parameters, voltage-current characteristics, and energy characteristics are given as the input for the model. A current grid sweep is simulated with the developed closed-loop current control along with the stator inverter and rotor converter. During these offline simulations, using the stator phase currents, rotor field excitation current, frequency, etc., the overall system loss is computed and are stored. These simulations are held at multiple speeds until the maximum speed of the WFSM and at various stator, rotor, and inverter junction temperatures. Then, the brute-force algorithm, as shown in Fig. 3.14, takes inputs/characters such as reference torque & speed, temperatures of rotor stator and junction of inverter and IPT converter from the user. The brute-force algorithm will perform multiple outer search loops to find out the nearest simulated torque values to the reference torque values from the stored data to create an array of the values that are nearest to the torque reference or in other words satisfying $\epsilon_{\text{torque}} < 0.2 - 0.5 \text{ Nm}$. During the same instant, the values of overall losses, i_{dqf} axis current are also stored. Now, having multiple arrays with the values of torques, i_{dqf} axis currents, overall system losses, etc. All the stored torque values satisfy the $\epsilon_{\text{torque}} < 0.2 - 0.5 \text{ Nm}$ when compared to the reference torque. Now, the inner search loop will select the torque value with the least overall system losses from the stored array. Hence, finding the optimal direct, quadrature, and field axis currents to achieve the commanded torque satisfying the minimum overall system losses or maximum overall system efficiency per ampere criteria. The entire torque-speed envelope is given as input to the above-mentioned algorithm to create an optimal look-up table for achieving maximum overall system efficiency.

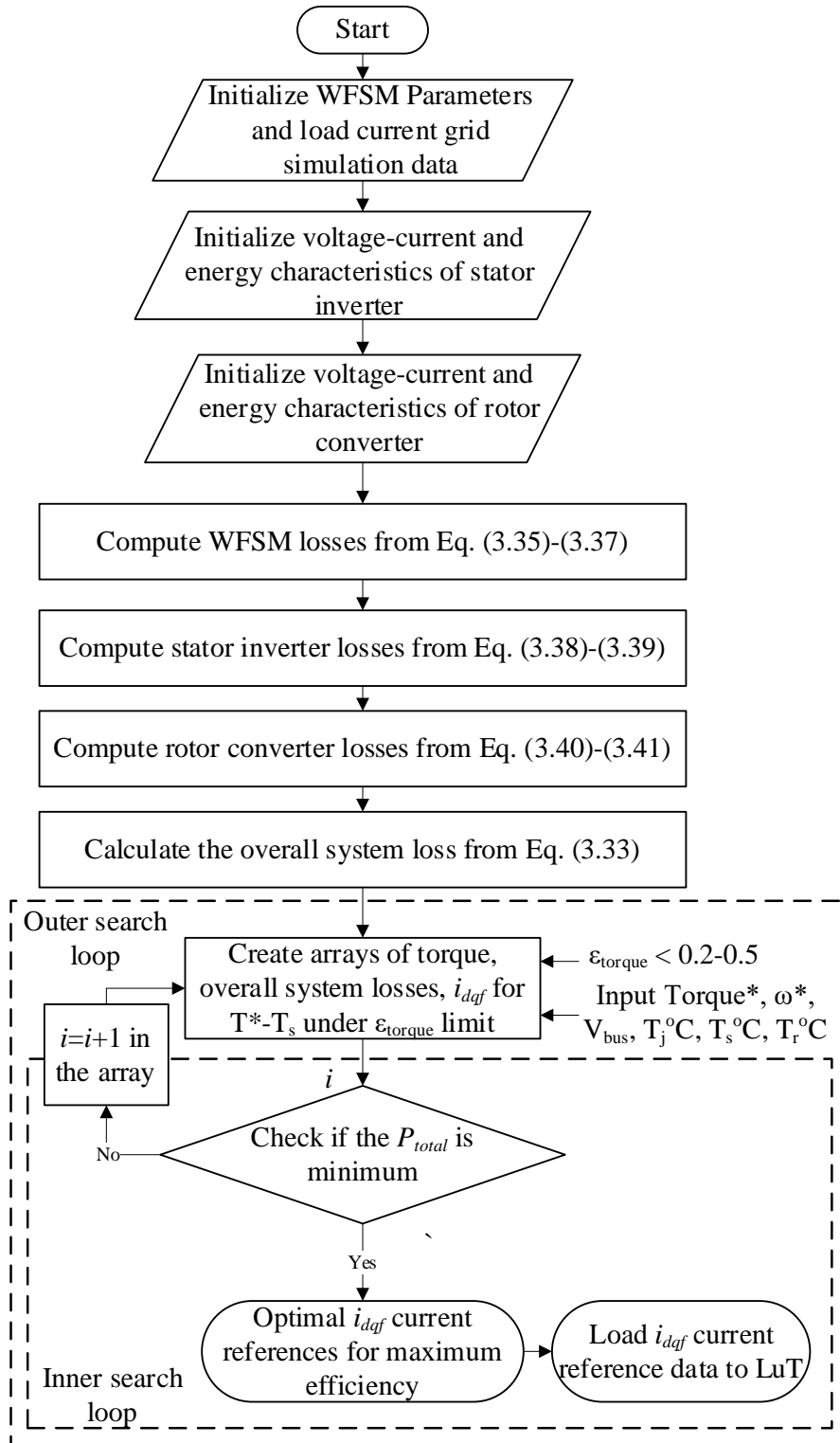


Fig. 3.14. Brute-force algorithm for finding i_{dqf} current references towards maximum overall system per ampere of IPT-based WFSM.

3.5.3 Comparison of Maximum Overall System Efficiency Per Ampere Algorithm vs Maximum Torque Per Ampere Algorithm

In this section, the difference in maximum torque per ampere (MTPA) and maximum overall system efficiency per ampere control is investigated. As discussed previously, the MTPA control algorithm focuses on achieving maximum torque for the -

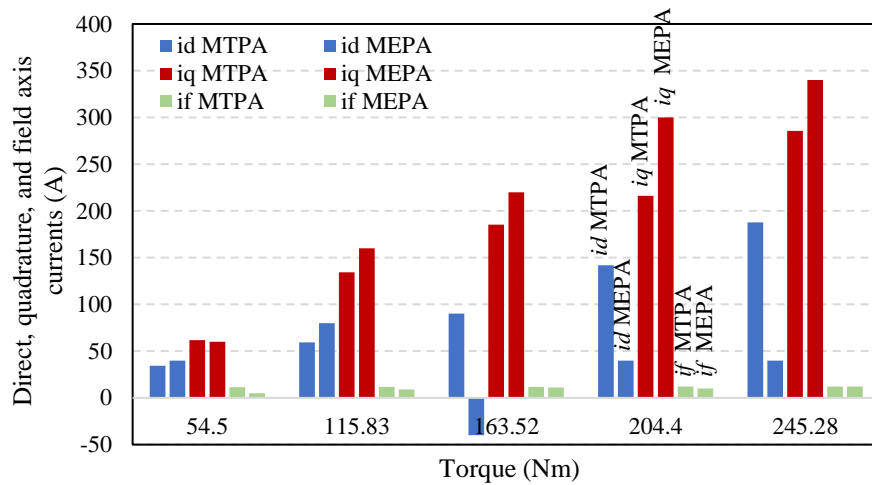


Fig. 3.15. Comparison of direct, quadrature, and field axis current references between MTPA and maximum overall system efficiency methods.

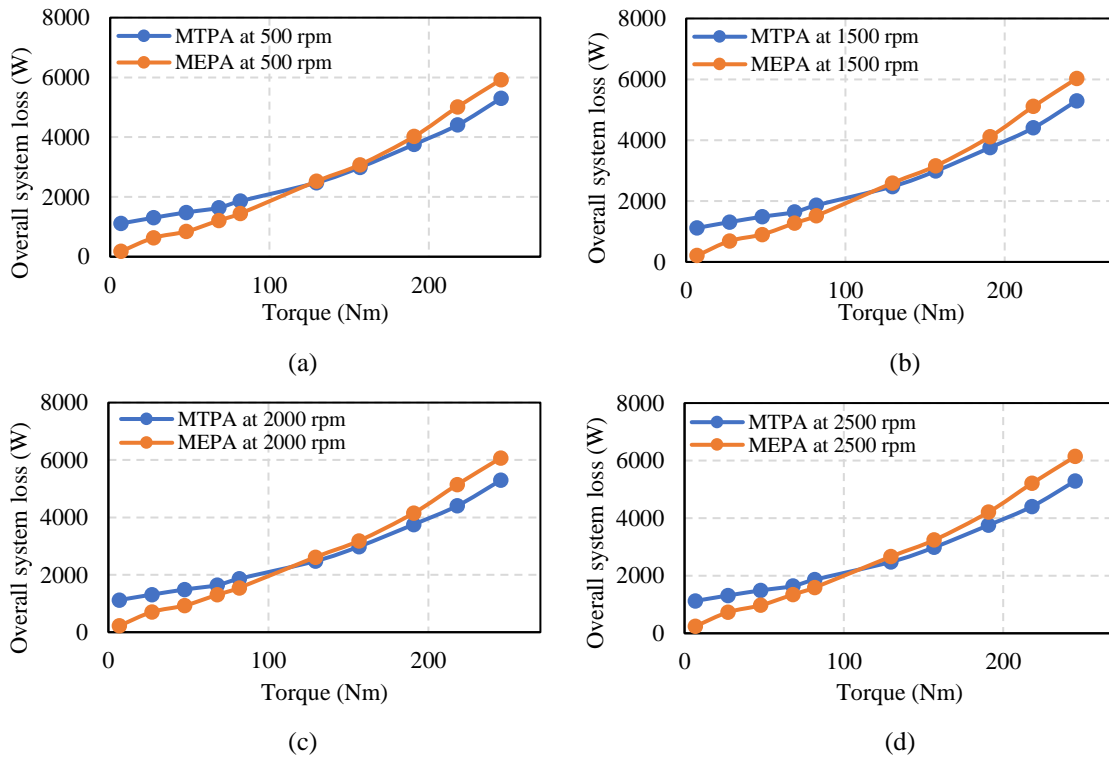


Fig. 3.16. Comparison of overall system losses between MTPA and maximum overall system efficiency per ampere methods. (a) at 500 rpm. (b) at 1500 rpm. (c) at 2000 rpm. (d) at 2500 rpm

minimum usage in the current/ampere. Therefore, the MTPA only focuses on the motor and not the whole system. On the other hand, the maximum overall system efficiency per ampere control focuses on achieving the maximum overall system efficiency satisfying the torque command. Therefore, a comparison is made in the distribution of stator and field reference current among the two control methods. As shown in Fig. 3.15, the current references are compared at various torque load points. The comparison is investigated at a constant rotor speed of 1,500 rpm. A major difference is seen in the field reference currents between the two control methods, the MTPA, in most cases, uses the maximum field current to generate the maximum instant torque. The phase advance in the maximum overall system efficiency method is always kept close to zero degrees, whereas in the MTPA method, the phase advance is varied to utilize a maximum of the reluctance torque.

Figure 3.16. shows the comparison of overall system losses between both control methodologies. The system losses include the losses of WFSM, three-phase stator inverter, and single-phase rotor converter. The overall system losses are seen to be reduced significantly in the proposed maximum overall system efficiency control method when compared to conventional MTPA. However, the improvement is mainly observed in the lower torque level since the field current is not reached its maximum limit in the maximum efficiency control method. The proposed algorithm and the control methodology can be used as a LuT in the speed control as discussed in the sub-section 3.2.2 for generating optimal current references towards maximum overall system efficiency.

3.6 Conclusion

In the chapter, the closed-loop current and speed control are developed with the mathematical models developed in Chapter 2. The PI controller gains are derived using the pole-zero cancellation method for the closed-loop control. Also, a maximum overall system efficiency per ampere control algorithm is proposed and the upper hand on the conventional MTPA control algorithm is discussed for IPT-based WFSM. The maximum overall system efficiency control algorithm's current references are generated using the brute-force algorithm using the computer overall system losses.

In the next chapter, the developed closed-loop current control models are tested on an experimental testbench. The performance of the developed closed-loop current

controllers and the accuracy of the mathematical motor model is also validated by comparing the simulation and experimental results.

3.7 References

- [1] T. Dey, K. Mukherjee, and P. Syam, "Dynamic adjustments of the D-Q axes reference voltage limits during flux weakening and MTPA control of an IPMSM drive for an EV application," in *Proc. 2nd International Conference on Control, Instrumentation, Energy & Communication (CIEC)*, 2016, pp. 324-328, doi: 10.1109/CIEC.2016.7513821.
- [2] N. Bhowmick, K. Mukherjee, and P. Syam, "Design, Control and Simulation Study of a 3-Phase PWM Converter for Unity Power Factor Applications Independent of Load Variations," in *Proc. IEEE 22nd Workshop on Control and Modelling of Power Electronics (COMPEL)*, 2021, pp. 1-6, doi: 10.1109/COMPEL52922.2021.9645771.
- [3] W. J. Kerw and R. W. Carlsten, "A new method of compensation using pole-zero cancellation applied to the design of a voltage-controlled buck converter," in *Proc. IEEE Applied Power Electronics Conference and Exposition*, New Orleans, Louisiana, USA, 1986, pp. 26-34.
- [4] D. Nanda, K. Mukherjee and P. Syam, "A Simplified Control Technique for a Z-Source PWM Rectifier," in *Proc. IEEE Region 10 Symposium (TENSymp)*, 2022, pp. 1-6, doi: 10.1109/TENSymp54529.2022.9864561.
- [5] A. Maiti, K. Mukherjee and P. Syam, "Design, modeling and software implementation of a current-perturbed maximum power point tracking control in a DC-DC boost converter for grid-connected solar photovoltaic applications," in *Proc. IEEE First International Conference on Control, Measurement and Instrumentation (CMI)*, 2016, pp. 36-41, doi: 10.1109/CMI.2016.7413706.
- [6] N. Mohan, *Electric Drives: An Integrative Approach*. MNPERE, 2003.
- [7] M. Märgner and W. Hackmann, "Control challenges of an externally excited synchronous machine in an automotive traction drive application," in *Proc. Emobility – Electrical Power Train*, 2010, pp. 1–6, doi: 10.1109/EMOBILITY.2010.5668056.
- [8] C. D. Nguyen and W. Hofmann, "Self-tuning adaptive copper-losses minimization control of externally excited synchronous motors," in *Proc. International Conference on Electrical Machines (ICEM)*, 2014, pp. 897–902, doi: 10.1109/ICELMACH.2014.6960287.

- [9] Y. Kim and K. Nam, "Copper-loss-minimizing field current control scheme for wound synchronous machines," *IEEE Trans. Power Electronics*, vol. 32, no. 2, pp. 1335–1345, Feb. 2017, doi: 10.1109/TPEL.2016.2547953.
- [10] Q. Liu and K. Hameyer, "High performance adaptive torque control for an IPMSM with real time MTPA operation," *IEEE Trans. Energy Convers.*, vol. 32, no. 2, pp. 571–581, Jun. 2017.
- [11] T. Inoue, Y. Inoue, S. Morimoto, and M. Sanada, "Mathematical model for MTPA control of permanent-magnet synchronous motor in stator flux linkage synchronous frame," *IEEE Trans. Ind. Appl.*, vol. 51, no. 5, pp. 3620–3628, Sep./Oct. 2015.
- [12] Y. A. R. I. Mohamed and T. K. Lee, "Adaptive self-tuning MTPA vector controller for IPMSM drive system," *IEEE Trans. Energy Convers.*, vol. 21, no. 3, pp. 636–644, Sep. 2006.
- [13] S. Bolognani, R. Petrella, A. Prearo, and L. Sgarbossa, "Automatic tracking of MTPA trajectory in IPM motor drives based on AC current injection," *IEEE Trans. Ind. Appl.*, vol. 47, no. 1, pp. 105–114, Jan./Feb. 2011.
- [14] D. Reigosa, F. Briz, P. Garcia, J. Guerrero, and M. Degner, "Magnet temperature estimation in surface PM machines using high-frequency signal injection," *IEEE Trans. Ind. Appl.*, vol. 46, no. 4, pp. 1468–1475, Jul./Aug. 2010.
- [15] A. Ahmed, Y. Sozer, and M. Hamdan, "Maximum torque per ampere control for buried magnet PMSM based on DC-link power measurement," *IEEE Trans. Power Electron.*, vol. 32, no. 2, pp. 1299–1311, Feb. 2017.
- [16] K. Yamazaki and Y. Seto, "Iron loss analysis of interior permanent magnet synchronous motors—Variation of main loss factors due to driving condition," *IEEE Trans. Ind. Appl.*, vol. 42, no. 4, pp. 1045–1052, Jul./Aug. 2006.
- [17] N. C. Kar *et al.*, "Courting and sparking: Wooing consumers? Interest in the EV market," *IEEE Electrific. Mag.*, vol. 1, no. 1, pp. 21–31, Sep. 2013.
- [18] A. Emadi, *Energy-Efficient Electric Motors: Selection and Applications*. New York, NY, USA: Marcel Dekker, Sep. 2004.
- [19] C. Lai, G. Feng, K. Mukherjee, J. Tjong, and N. Kar, "Maximum torque per ampere control for IPMSM using gradient descent algorithm based on measured speed harmonics," *IEEE Trans. Ind. Informat.*, vol. 14, no. 4, pp. 1424–1435, Apr. 2018.

- [20] C. Cavallaro, A. O. D. Tommaso, R. Miceli, A. Raciti, G. R. Galluzzo, and M. Tranpanese, "Efficiency enhancement of permanent-magnet synchronous motor drives by on-line loss minimization approaches," *IEEE Trans. Ind. Electron.*, vol. 52, no. 4, pp. 1153–1160, Aug. 2005.
- [21] J. Lee, K. Nam, S. Choi, and S. Kwon, "Loss-minimizing control of PMSM with the use of polynomial approximations," *IEEE Trans. Power Electron.*, vol. 24, no. 4, pp. 1071–1082, Apr. 2009.
- [22] A. M. Bazzi and P. T. Krein, "Review of methods for real-time loss minimization in induction machines," *IEEE Trans. Ind. Appl.*, vol. 46, no. 6, pp. 2319–2328, Nov./Dec. 2010.
- [23] S. Vaez, V. I. John, and M. A. Rahman, "An on-line loss minimization controller for interior permanent magnet motor drives," *IEEE Trans. Energy Convers.*, vol. 14, no. 4, pp. 1435–1440, Dec. 1999.
- [24] M. N. Uddin and J. Khastoo, "Fuzzy logic-based efficiency optimization and high dynamic performance of IPMSM drive system in both transient and steady-state conditions," *IEEE Trans. Ind. Appl.*, vol. 50, no. 6, pp. 4251–4259, Nov./Dec. 2014.
- [25] A. Balamurali, G. Feng, C. Lai, J. Tjong and N. C. Kar, "Maximum Efficiency Control of PMSM Drives Considering System Losses Using Gradient Descent Algorithm Based on DC Power Measurement," *IEEE Trans. Energy Conversion*, vol. 33, no. 4, pp. 2240-2249, Dec. 2018, doi: 10.1109/TEC.2018.2852219.

CHAPTER 4

HARDWARE IMPLEMENTATION OF WOUND FIELD SYNCHRONOUS MACHINE CLOSED-LOOP CURRENT CONTROL VALIDATION

4.1 Introduction

In Chapters 2 and 3, mathematical modeling of wound field synchronous machine (WFSM), three-phase voltage source inverter, and closed-loop current controls are discussed. This chapter extends the previous chapter's work towards the development of the rapid control prototyping (RCP) test bench, hardware implementation of developed motor control models, and validation of results are demonstrated. A proportional-integral (PI) controller-based closed-loop current control is implemented on the three axes in the WFSM, namely, direct, quadrature, and field axis respectively. For the pulse width modulation (PWM), sine pulse width modulation (SPWM) technique is implemented. The importance of the real-time embedded controller in rapid control prototyping is discussed for motor control applications. Validation of simulation against experiments is shown both in transient and steady-state load points.

4.2 Real-Time Embedded Controller

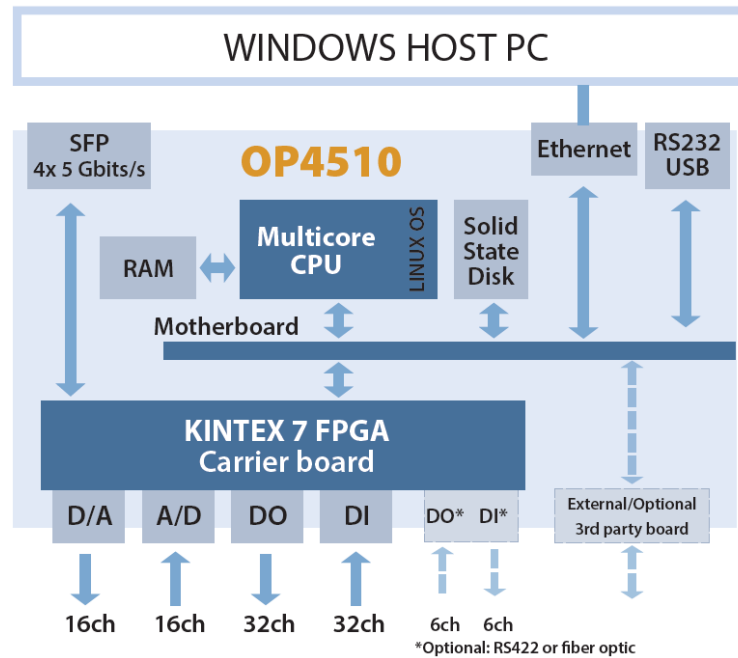


Fig. 4.1. Real-time controller architecture [1].

The architecture of the real-time embedded controller used is shown in Fig. 4.1 [1]. This controller has 128 fast input and output channels with signal conditioning that includes low-speed fiber-optic communication channels. This controller uses an INTEL multicore 3.5 GHz processor with Xilinx Kintex 7 FPGA. The 128 fast I/O includes 16 analog output, 16 analog input, 32 digital output, and 32 digital input channels, respectively. The developed motor control model is flashed on the controller's CPU, and the functions are run in real-time. The Kintex 7 FPGA board on the controllers allows mapping input and output peripherals [5].

Computer software simulations are broadly divided into two categories according to the solver settings, namely, (i) fixed-step simulations and (ii) variable-step simulations. The simulations in the real-time embedded controller are usually discrete-time simulations with a constant step i.e., fixed-step simulations [2], [3]. On the other hand, variable-step time simulations vary the step time according to the type and complexity of the simulations. This technique is usually used in solving non-linear and very low step-time dynamic simulations [4]. Therefore, in the fixed-time or discrete simulations, all the computational functions in the simulations are performed in the same time frame. This synchronization of the computation functions with the simulation clock is called synchronized real-time simulation, as shown in Fig. 4.2 [2]. If the computational operations are not performed within the fixed-step time, the synchronization is lost, and this event is usually called an “overrun”. In the case of offline simulations, the computational functions might happen faster or slower when compared to the simulation clock.

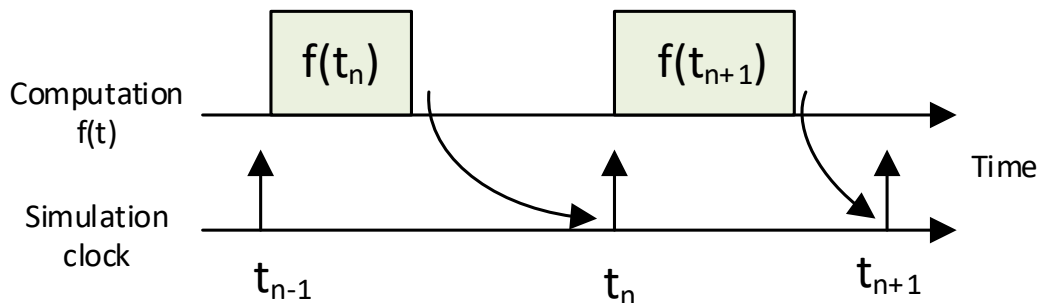


Fig. 4.2. Synchronized real-time simulations computational time profile.

4.3 Closed-Loop Current Control Hardware Development

As discussed in Chapter 3, there exist three current control loops for WFSM, namely: direct, quadrature, and field axis. Hence, a closed-loop motor control model should be developed and flashed into the real-time embedded controller. The motor control model should be able to bridge software and hardware integration in synchronism for seamless control. The hardware includes control of both the stator inverter and rotor converter simultaneously. Figure 4.3. shows the block diagram of the hardware and software interface, including the closed-loop control diagram. A high-accuracy current transducer is used for d , q , and f -axis current feedback. The feedback currents are used for Park's transformation. For the Park's transformation, the rotor position is sensed from a high-speed variable reluctance resolver. SPWM technique is used for the stator digital out pulses, and PWM technique is used for the rotor buck converter with a variable duty ratio through closed-loop control.

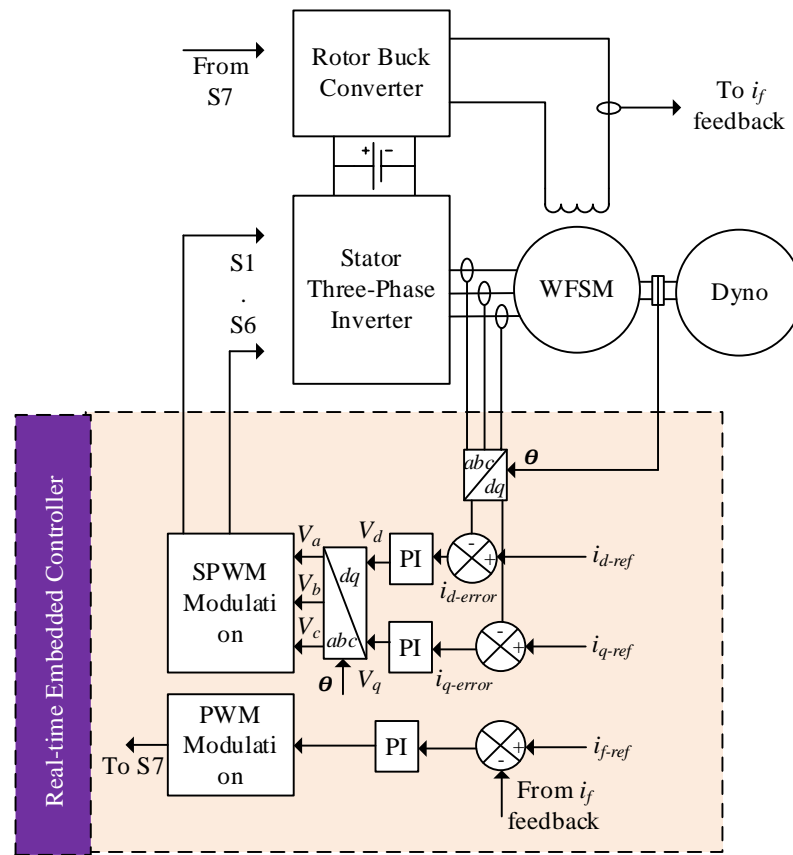


Fig. 4.3. Block diagram of hardware and software synchronization.

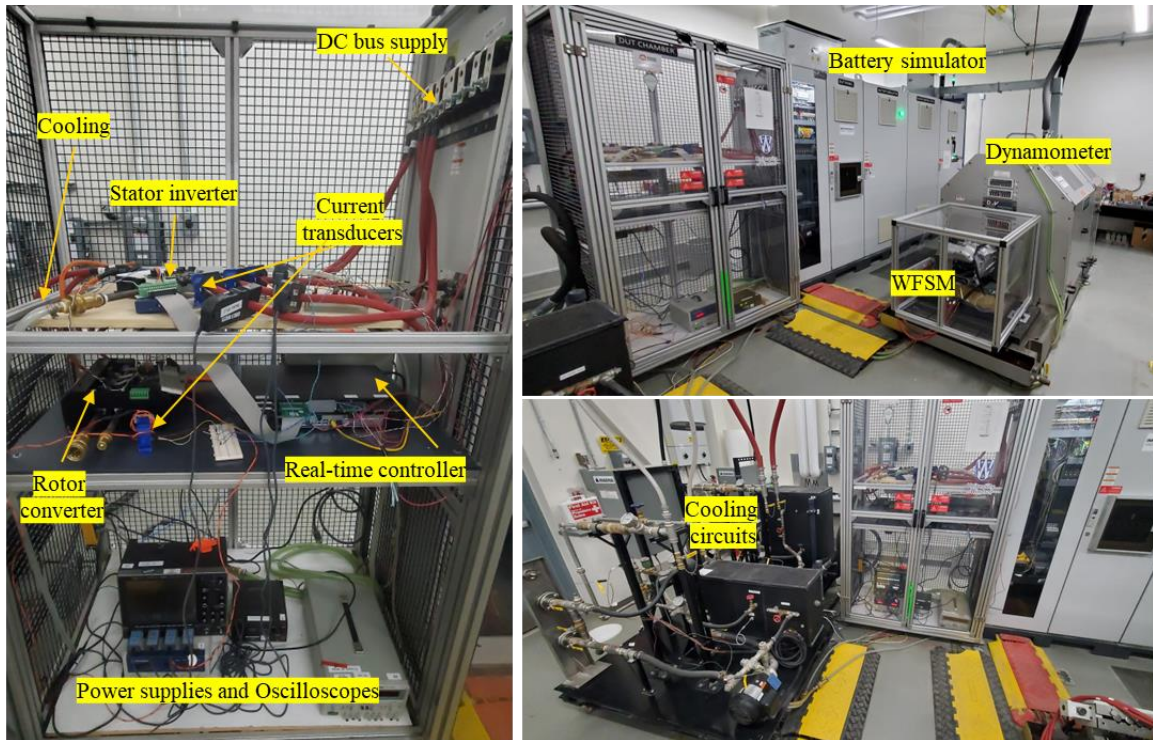


Fig. 4.4. Overall test rig setup for WFSM closed-loop current control.

Figure. 4.4 shows the overall test rig setup with an inverter for a three-phase stator supply, an inverter as a buck converter for the WFSM field excitation, a real-time embedded controller, cooling circuits, high-voltage DC bus supply, low-voltage DC supplies, oscilloscopes, etc. It is important to note that the DC high voltage supply is shared between both the inverter and converters. The WFSM used in the simulations and experimentation rated 100 kW.

4.3.1 Three-Phase Stator Inverter

Figure. 4.5 shows the 150 kW three-phase IGBT inverter connected to the high-voltage DC bus supply on the DC side and three-phase motor terminals on the output side. The inverter has an inbuilt gate driver circuit, as seen in Fig. 4.5 [6]. The amplified gate signals to the gate driver are provided by the embedded controller through high-speed digital output channels. There are a total of six gate signals from the controller to the inverter, and the gate signals are modulated in the SPWM technique. The gate signals are modulated according to the stator current and rotor position feedback from the current transducer and resolver. PI controllers are used for the closed-loop current control. The

output phase terminal connections to the WFSM are passed through the three-phase current transducers. The three-phase inverter is cooled through the cooling pipes connected to the heat sink with water ethylene glycol (WEG) passed at 10 liters per minute (LPM). The maximum phase current of this three-phase inverter is $580A_{rms}$, and the maximum DC bus voltage is $500 V_{DC}$ at a switching frequency of 12 kHz.

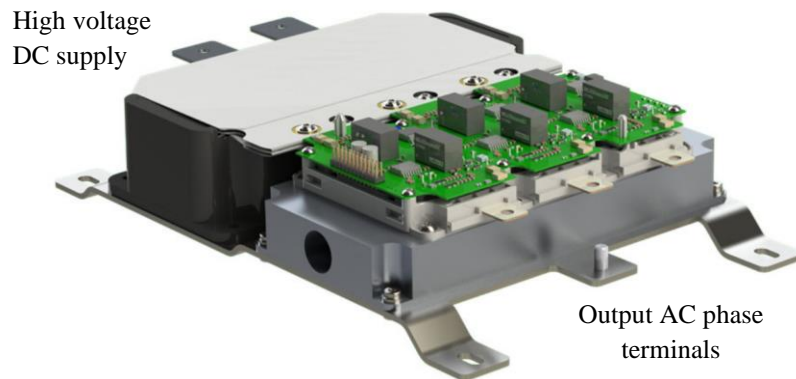


Fig. 4.5. Stator three-phase inverter connected to motor phase terminals through current transducers [6].

4.3.2 Rotor Buck Converter

For the WFSM rotor field excitation, a three-phase SiC inverter is operated as a buck converter. Therefore, only the top switch of the single-phase is switched. The amplified gate signals for the buck converter are generated from the embedded controller and are modulated with a variable duty ratio pulse width modulation (PWM) technique. The reference field excitation current is compared to the feedback field current sensed through the current transducer. A proportional-integral (PI) controller is used for the field excitation current closed-loop control. The WFSM field excitation terminals are connected between the mid-point of the single leg being used and the negative of the high-voltage DC bus supply, as shown in Fig. 4.6 [7]. It is important to note that both the gate signals to the inverter and the buck converter must be synchronized. The inverter used in the experimentation is rated for a maximum DC bus of 800 V and a maximum phase current of $360 A_{rms}$. The inverter is being switched at a rate of 10 kHz, and the inverter is cooled by passing water ethylene glycol (WEG) at a rate of 12 LPM.

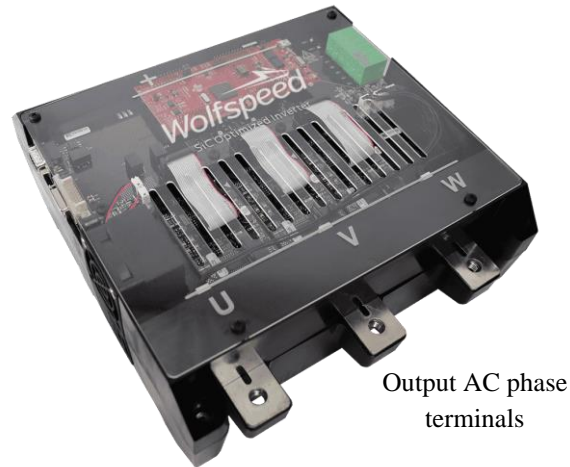


Fig. 4.6. Three-phase inverter operated as a buck converter for WFSM field excitation [7].

4.3.3 Three-Phase Current Transducers

Sensing accurate stator phase and WFSM field excitation feedback currents is very crucial for accurate closed-loop controls. The current transducers are broadly divided into open- and closed-loop current transducers. The open loop current transducer has a hall generator used to sense the magnetic flux density in the air gap to know the primary current passed through the transducer. On the other hand, the closed-loop current transducer has a hall generator that generates a compensation current in the secondary coil to compensate and create a total flux equal to zero. The secondary current creates a magnetic flux equal in magnitude in the opposite direction to the flux generated by the primary current [8], [9]. When the total flux is at zero condition, the secondary current in the secondary coil is exactly equal to the primary current in the primary coil. Therefore, a measuring resistance is connected in series to the secondary coil, as shown in Fig. 4.7 [10]. This creates a voltage difference across the measuring resistance, which is read into the embedded controller through the analog-in channels. The measured voltage corresponds to the primary current by a gain value that can be calculated through experiments or from the manufacturer datasheet. As shown in Fig. 4.8 [10], the high-accuracy closed-loop current transducers are used for all the stator phases and the WFSM field excitation terminal.

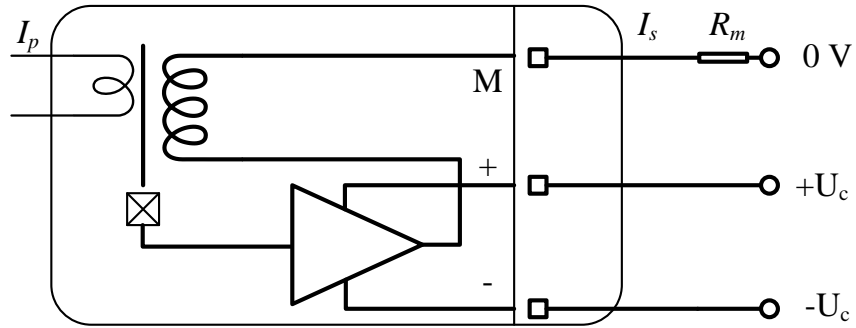


Fig. 4.7. Closed-loop current transducer block diagram.



Fig. 4.8. High-accuracy closed-loop current transducers connected through three-phase motor terminals [10].

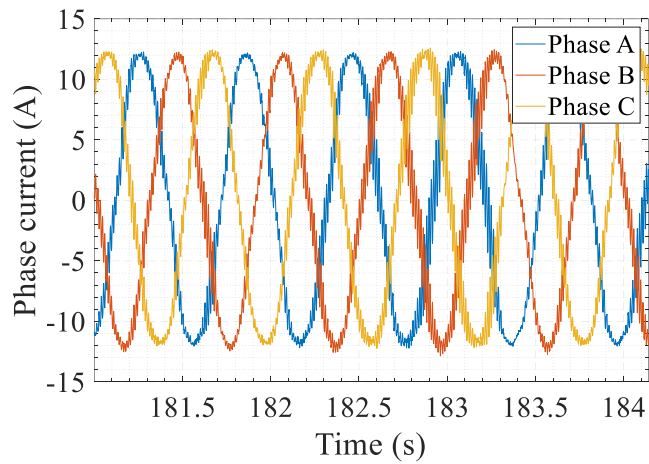


Fig. 4.9. Three-phase motor phase currents sensed through three-phase current transducers.

A sample of three-phase motor phase currents sensed through the three-phase current transducers is shown in Fig. 4.9. The maximum RMS current this current transducer

can sense is up to 500 A_{rms}, and the turn's ratio between the primary and secondary coil is 1:5,000.

4.3.4 Rotor Position Sensor

As discussed in the previous chapters, this thesis employs a closed-loop control. For the closed-loop control, the accurate rotor position is very important. The rotor position information is used for the Park's transformation, as discussed in chapter 2. The park's transformation transforms the three-phase variables into the rotating frame of reference. This helps eliminate the rotor position-dependent variables in the closed-loop control. There are many position sensors available for sensing the rotor position. However, in this thesis and experimentation, a variable reluctance mechanical resolver is used. This is because this type of position sensor is robust and durable during high-speed operation and testing. The variable reluctance (VR) resolver has three pairs of windings, namely, the input excitation circuit, output sine, and output cosine circuits. The output sine and cosine circuits are shifted by 90 degrees mechanically in the resolver. The input for the excitation circuit is fed with a sin wave of constant amplitude and frequency, usually ranging from 50-20,000 Hz [11]. The output of the resolver is modulated sine, and cosine signals which are 90 degrees apart, as shown in Fig. 4.10. The de-modulated sine and cosine output signals are used to calculate the resolver output as shown in equation 4.1. In other words, the demodulated signals are the envelope of the sine and cosine signals, as shown in Fig. 4.10 [12]. Fig. 4.11 shows the sample rotor position obtained at a constant speed of 100 rpm

$$\theta = \tan^{-1} \left(\frac{\sin}{\cos} \right) \text{ in radians} \quad (4.1)$$

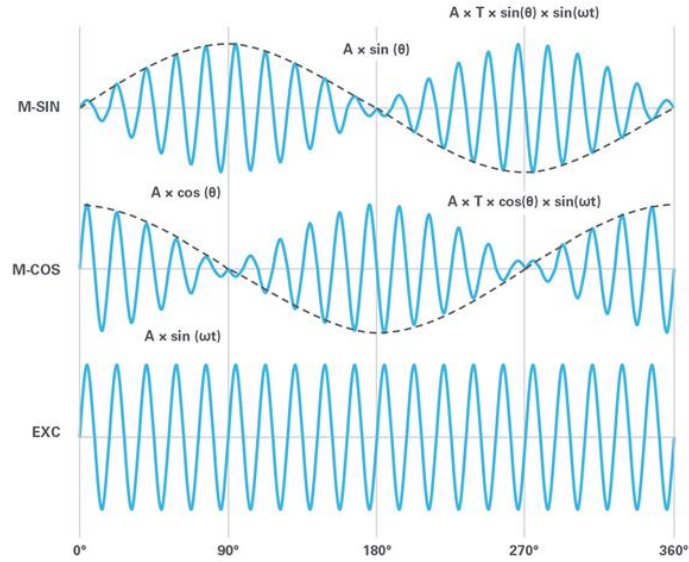


Fig. 4.10. Input excitation signal and output phase shifted sin and cos signals from the variable reluctance resolver [12].

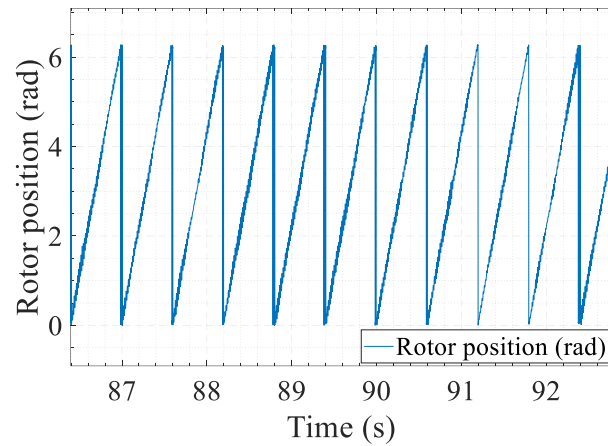


Fig. 4.11. Rotor position sensed through variable reluctance resolver under a constant speed of 100 rpm.

4.4 Back EMF Results

The wound field synchronous machine is excited by a constant field excitation current for generating back emf. The field excitation current is maintained at a constant level by the closed-loop current control. As discussed in the previous sections, a three-phase SiC inverter is used as a single-leg buck converter for field excitation. Figure. 4.12 shows the PWM voltage at the terminals of the field excitation circuit and a constant current of 6 A. For the back EMF test, the WFSM is run at a constant speed of 500 and 750 rpm at various field excitation currents. The generated line-to-line back EMF voltages are

measured at the open terminals of the WFSM. In WFSM, there exists coupling between the d and f axis, which can be calculated experimentally, as seen in the voltage equations (3.1)-(3.6) Under the operation of back EMF, the phase terminals of the motor are open-circuited. Hence, there are no phase currents flowing i.e., $i_d = i_q = 0$ A and there only exists i_f .

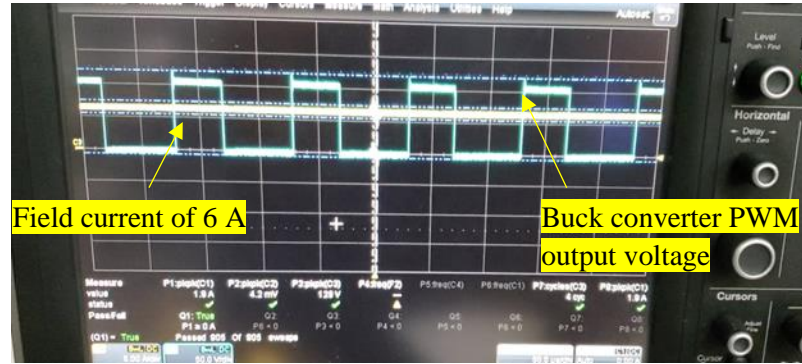


Fig. 4.12. Measured field excitation circuit PWM voltage and current.

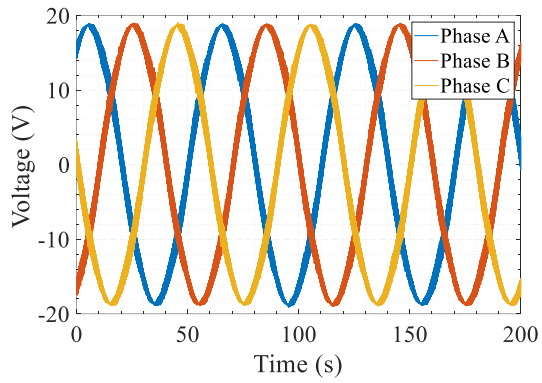
Substituting $i_d = i_q = 0$ A in the equation (4.2) -(4.5) and re-writing equations,

$$v_{ds} = 0 = r_s i_{ds} + L_{ds} \frac{di_{ds}}{dt} + L_m \frac{di_f}{dt} - \omega_r L_{qs} i_{ds} \quad (4.2)$$

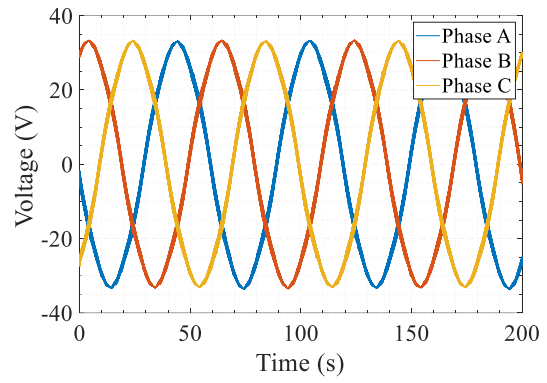
$$v_{qs} = r_s i_{qs} + L_{qs} \frac{di_{qs}}{dt} + \omega_r L_{ds} i_{ds} + \omega_r L_m i_{fr} \quad (4.3)$$

$$L_m = \frac{v_{qs}}{\omega_r i_{fr}} \quad (4.4)$$

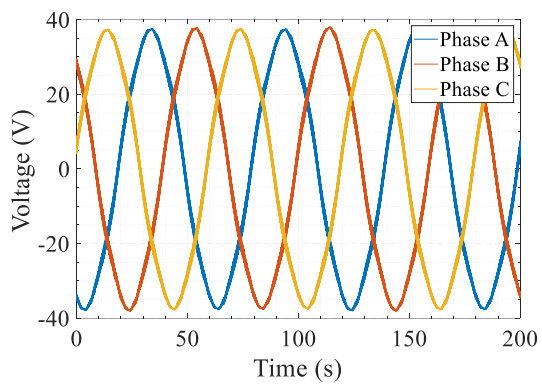
All the terms in (4.7) become zero because of $i_d = i_q = 0$ A. It is important to note that the $(L_m * di_f/dt)$ term in V_{ds} equation also becomes zero as there is no change in field current during steady-state operation. The mutual inductance between the d and f axis (L_m) can be experimentally calculated with the (4.9) from the back-EMF results. From the back EMF results, it can also be seen that there is no asymmetry in the sinusoidal three-phase stator windings.



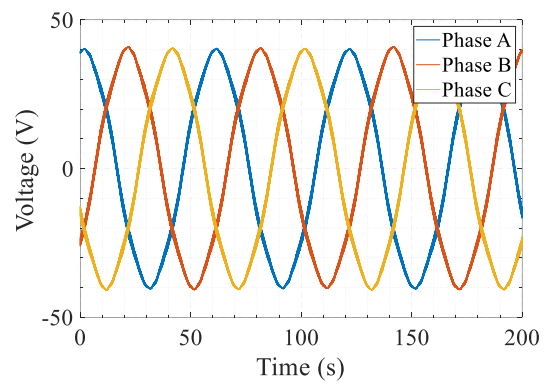
(a)



(b)

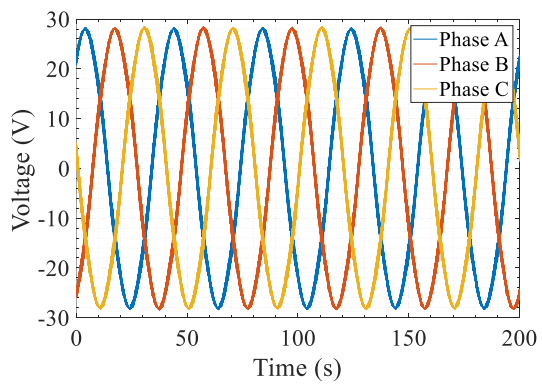


(c)

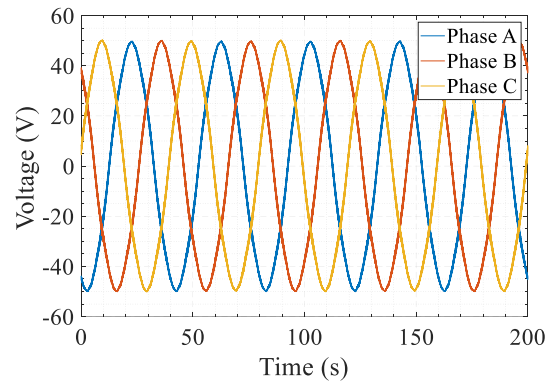


(d)

Fig. 4.13. Generated back EMF line-to-line voltage at a constant speed of 500 rpm at field excitation current of (a) 2 A. (b) 4 A. (c) 6 A. (d) 8 A.



(a)



(b)

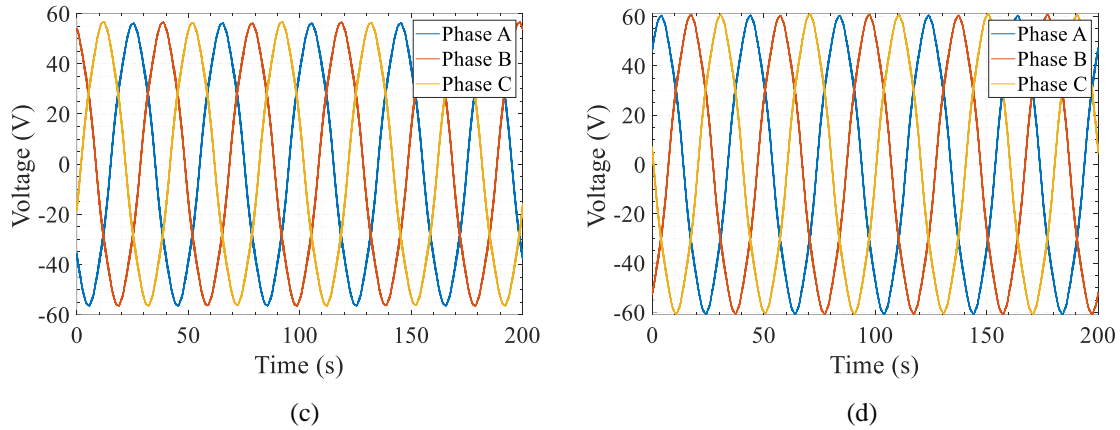


Fig. 4.14. Generated back EMF line-to-line voltage at a constant speed of 750 rpm at field excitation current of (a) 2 A. (b) 4 A. (c) 6 A. (d) 8 A.

4.5 Closed-Loop Current Control of WFSM on Dynamometer

The motor control algorithm for closed-loop current control is developed for the real-time embedded controller. The time-step of the real-time controller is set to run at the time step of 25 μ s. The proportional-integral (PI) controller's gains are designed according to the pole-zero cancellation method, as discussed in Chapter 3. The bandwidth of the d - and q -axis current controllers are made to be one-tenth of the switching frequency and one-fifth of the switching frequency for the f -axis current.

4.5.1 Direct Axis Closed-Loop Current Control

A series of step commands are given as a reference for the closed-loop control to verify the stability and robustness of the control. Fig. 4.15(a) shows the reference and measured currents on the direct axis and Fig. 4.15(b) shows the zoomed step response. The step responses are intentionally slowed down with a rate limiter. The (PI) output is limited by the integration limits to $V_{dc}/2$ to avoid overshoots during control validation during transient conditions.

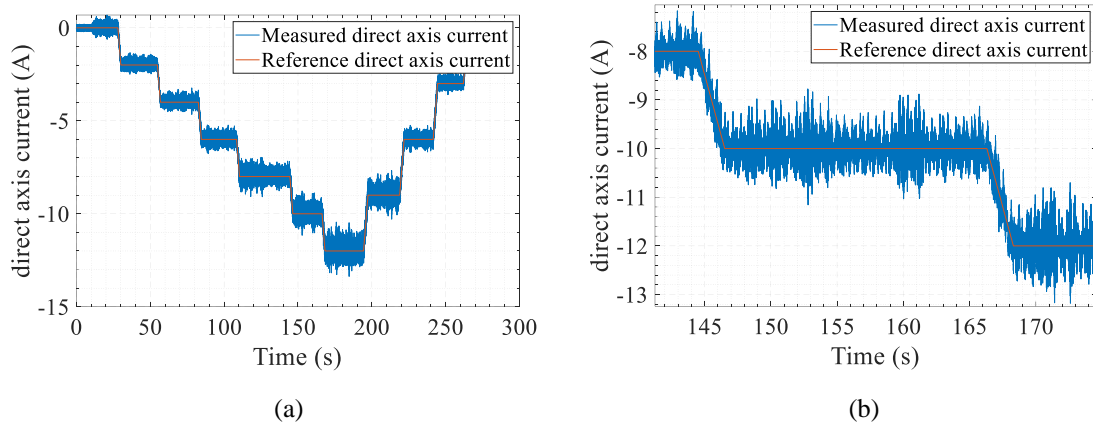


Fig. 4.15. Current tracking capability showing reference and measured direct axis currents. (a) Complete cycle response. (b) Zoomed step response.

4.5.2 Quadrature Axis Closed-Loop Current Control

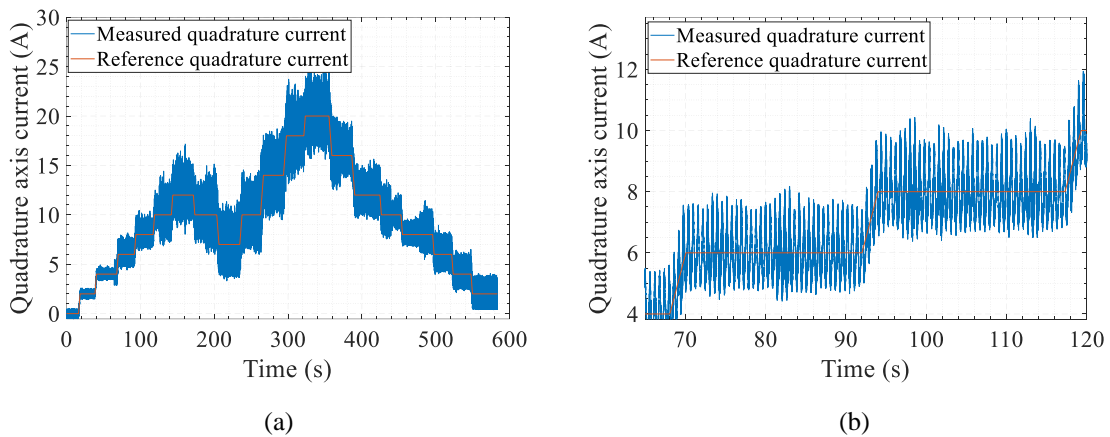


Fig. 4.16. Current tracking capability showing reference and measured quadrature axis currents. (a) Complete cycle response. (b) Zoomed step response.

Similar to the direct axis step response, a series of step reference commands are given as input for the quadrature axis closed-loop control. The reference commands and the measured quadrature axis current are shown in Fig. 4.16(a), and Fig. 4.16(b) shows the zoomed step response. The (PI) output is limited by the integration limits to $V_{dc}/2$ to avoid overshoots during control validation during transient conditions similar to the direct axis PI controller.

4.5.3 Field Axis Closed-Loop Current Control

Unlike the direct and quadrature axis closed-loops, the field axis closed-loop current control is not dependent on the rotor position information. Therefore, only the field excitation feedback current is used for the closed-loop control. A series of step responses are given as the reference to the closed-loop control, and the feedback is measured. As discussed in Fig. 4.3, the high-voltage DC bus supply is shared among the stator inverter and the rotor converter. The rated field excitation voltage might be very low compared to the DC bus supply. Hence, to protect the field excitation circuit from overcurrent, the (PI) controller's integration saturation limits are reduced to the rated field excitation voltage. Figures. 4.17(a) and (b) show the reference and measured field currents during the complete cycle and during step response.

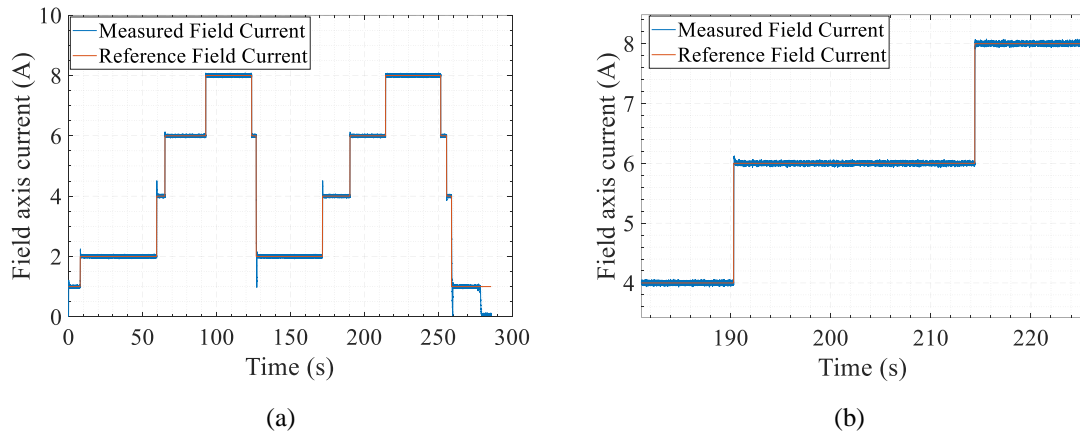


Fig. 4.17. Current tracking capability showing reference and measured quadrature axis currents. (a) Complete cycle response. (b) Zoomed step response.

4.5.4 Observations on Cross-Coupling Effects

In Chapter 2, the effects of cross-coupling between the direct and field axis are discussed, corresponding to the direct and quadrature axis voltage equations. As seen in (3.1)-(3.2), there exists cross-coupling terms, $\omega_e \lambda_d$, and $\omega_e \lambda_q$. The flux linkage terms are given as follows: Substituting (3.4)-(3.6) in (3.1) and (3.2) shows the cross-coupling between the field and quadrature axis. From the above equations, it may be concluded that in the presence of a field excitation current, there exists a cross-coupling effect that induces an asymmetry in the stator phase currents, as shown in Fig. 4.18. In Fig. 4.19, stator phase currents are symmetric in the absence of field excitation current.

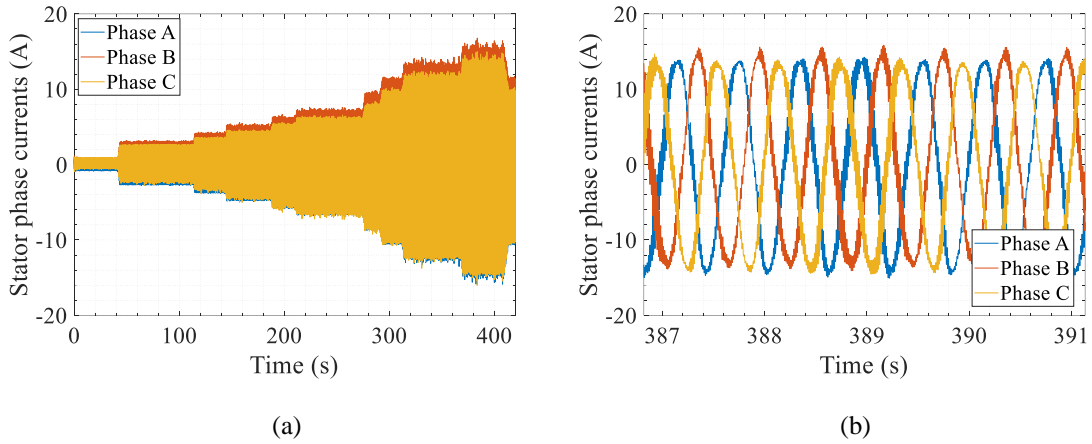


Fig. 4.18. Asymmetric stator phase currents in the presence of field excitation current. (a) Complete cycle response. (b) Zoomed step response.

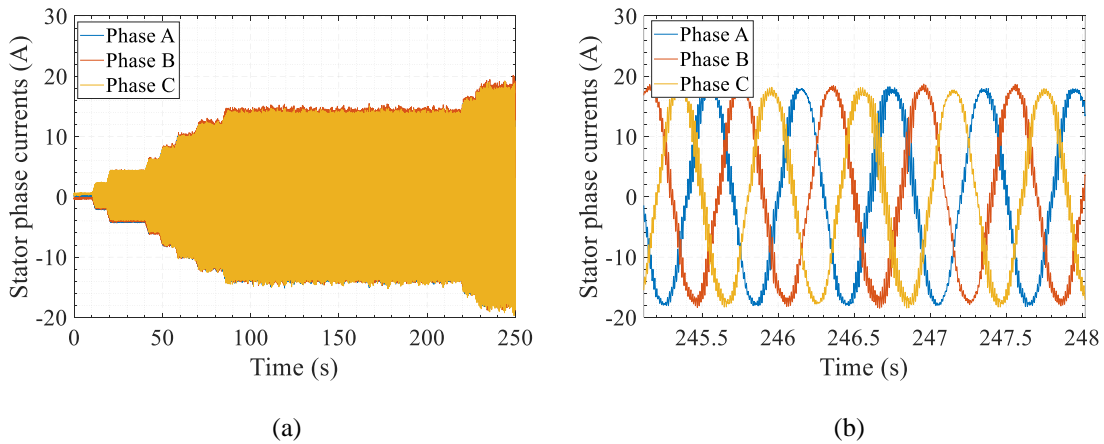


Fig. 4.19. Symmetric stator phase currents in the presence of field excitation current. (a) Complete cycle response. (b) Zoomed step response.

4.6 Validation of Experimental Results

The WFSM experimentation results are validated in two steps in two aspects: (i) closed-loop control validation during transients, (ii) steady-state load point validation.

4.6.1 Closed-Loop Control Validation During Transients

Closed-loop control validation for WFSM is performed by providing quadrature and field axis currents as inputs to the closed-loop control loops under zero direct axis currents. Fig. 4.20(a) and 4.21(a) show the reference and measured response of quadrature and field axis currents, and Fig. 4.20(b) and 4.21(b) show the measured three-phase stator currents.

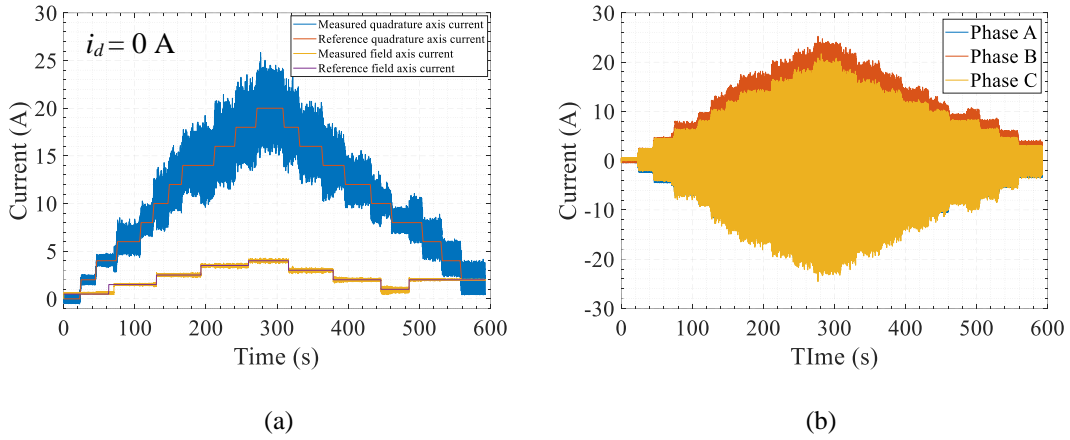


Fig. 4.20. Closed-loop control validation during zero direct axis current for load profile-I. (a) Quadrature and field axis currents. (b) Three-phase stator phase currents.

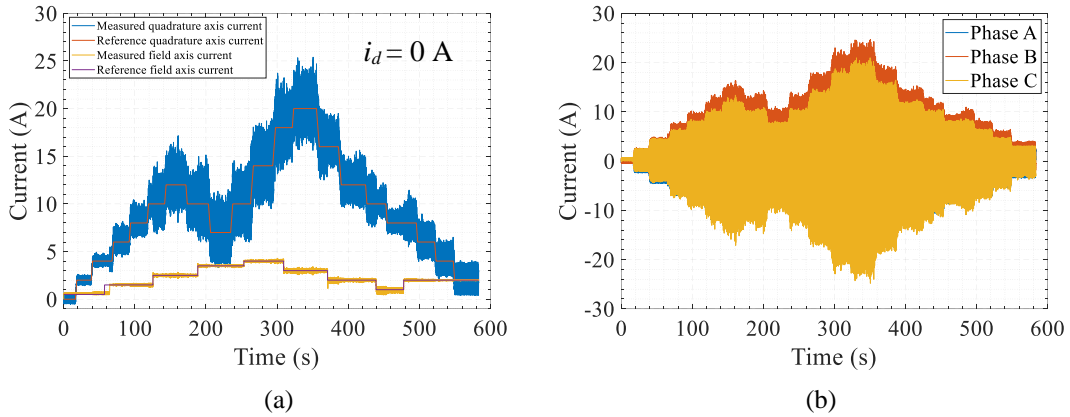


Fig. 4.21. Closed-loop control validation during zero direct axis current for load profile-II. (a) Quadrature and field axis currents. (b) Three-phase stator phase currents.

4.6.2 Steady State Load Points Validation

Various load points are selected at different sets of direct, quadrature, and field axis currents. Torque is simulated and measured for the selected load points in the developed simulation model and developed experimental test rig. Table. 4.1 shows the comparison between simulation and experimentation for validating steady-state load points. As seen in the table, the difference in torque is almost zero or negligible in the lower torque points; however, there exists a variation in the torque in the higher torque load points. This might be because of the considering ideal mechanical losses and temperature non-dependency of the simulation model.

TABLE 4.1

VALIDATION OF STEADY STATE LOAD POINTS BETWEEN SIMULATION AND EXPERIMENTAL RESULTS

| S. No | Simulation Results | | | | Experimental Results | | | |
|-------|--------------------|-----------|-----------|-------------|----------------------|-----------|-----------|-------------|
| | i_d (A) | i_q (A) | i_f (A) | Torque (Nm) | i_d (A) | i_q (A) | i_f (A) | Torque (Nm) |
| 1 | 5.346 | 29.60 | 8 | 19.390 | 5.2763 | 29.599 | 8 | 19.779 |
| 2 | 20.70 | 118.1 | 7.998 | 76.69 | 20.77 | 118.118 | 8 | 79.968 |
| 3 | 41.62 | 236.4 | 8 | 153.7 | 41.609 | 236.385 | 8 | 152.163 |
| 4 | 62.47 | 354.2 | 8.01 | 237.4 | 62.486 | 354.359 | 8 | 210.732 |
| 5 | 10.15 | 28.05 | 3.981 | 11.970 | 10.205 | 28.162 | 4 | 15.682 |
| 6 | 51.39 | 141 | 3.998 | 57.21 | 51.307 | 141.021 | 4 | 78.410 |
| 7 | 82.09 | 225.6 | 4 | 91.320 | 82.103 | 225.489 | 4 | 119.684 |
| 8 | 123.2 | 338.6 | 4.001 | 145.9 | 123.23 | 338.469 | 4 | 164.724 |

4.7 Conclusion

In this chapter, the introduction and the requirement for real-time control are discussed in a detailed manner. Later, the complete development procedure of the experimental test rig is explained for the three-phase stator inverter, rotor buck converter, working principles of three-phase current transducers, and rotor position sensor are discussed. In the end, closed-loop control tests are performed for various direct, quadrature, and field axis currents to validate the current controllers. Also, to validate the torque points between the simulation and experimental results. This proves the accuracy of the WFSM machine and control simulation models built in the previous chapters.

4.8 References

- [1] "OP4510 V2 System Description," Accessed on Oct. 19, 2022. [Online]. Available: <https://wiki.opal-rt.com/display/HDGD/OP4510+V2+System+Description>
- [2] "The What, Where and Why of Real-Time Simulation," Accessed on Oct. 19, 2022. [Online]. Available: https://blob.opal-rt.com/medias/L00161_0436.pdf

- [3] J. J. Sanchez-Gasca, R. D'Aquila, W. W. Price, and J. J. Paserba, "Variable time step, implicit integration for extended term power system dynamic simulation," in *Proc. Power Industry Computer Application Conference*, 1995, Salt Lake City, UT, USA, 7-12 May 1995, pp.183-189.
- [4] D. Gillies. (2009, Oct.) Internet FAQ Archives. [Online]. <http://www.faqs.org/faqs/realtime-computing/faq/>
- [5] "OP4510 Simulator – OPAL-RT" Accessed on Oct. 21, 2022 [Online]. Available: https://blob.opal-rt.com/medias/L00161_0124.pdf.
- [6] "NVH820S75L4SPB-EVK: VE-Trac Direct EZ Kit", Accessed on Nov. 2022. [Online] Available: <https://www.onsemi.com/design/tools-software/evaluation-board/nvh820s75l4spb-evk>
- [7] "300kW XM3 Three-Phase Inverter: CRD300DA12E-XM3", Accessed on Nov. 2022. [Online] Available: <https://www.wolfspeed.com/crd300da12e-xm3/>
- [8] "What is the Difference between Closed Loop and Open Loop?", Accessed on Nov. 2022. [Online]. Available: <https://www.electrohms.com/faq-what-is-the-difference-between-closed-loop-and-open-loop#:~:text=While%20open%20loop%20current%20transducers,Hall%20generator%2C%20equal%20to%20zero.>
- [9] "Hall Effect Current Sensing: Open-Loop and Closed-Loop Configurations," Jul. 25, 2021, Accessed on Nov. 2022. [Online]. Available: <https://www.allaboutcircuits.com/technical-articles/hall-effect-current-sensing-open-loop-and-closed-loop-configurations/>
- [10] "LEM: Current Transducer LF 510-S," Accessed on Nov. 2022. [Online]. Available: https://www.lem.com/sites/default/files/products_datasheets/lf_510-s.pdf
- [11] "Precision Resolver-to-Digital Converter Measures Angular Position and Velocity," Mar. 2014, Accessed on Nov. 2022. [Online]. Available: <https://www.analog.com/en/analog-dialogue/articles/precision-rtdc-measures-angular-position-and-velocity.html>
- [12] "High Accuracy Resolver Simulator System with Fault Injection Function," Aug. 2019, Accessed on Nov. 2022. [Online]. Available: <https://www.analog.com/en/analog->

<dialogue/articles/high-accuracy-resolver-simulator-system-with-fault-injection-function.html>

CHAPTER 5

NOVEL CONVERTER AND CONTROL TOPOLOGY FOR ENHANCING CONSTANT TORQUE AND POWER REGIONS OF WFSM

5.1 Introduction

In Chapters 1, 2, 3, and 4, the modeling of wound field synchronous machine (WFSM), closed-loop control development, and testing were discussed. In Chapter 3, The developed maximum overall system efficiency improvement control is machine specific, i.e., dependent on the machine specification. This indirectly means that the efficiency is improved only for a specific torque-speed profile of a specific machine. In this chapter, mathematical modeling of vehicle dynamics is shown, and a novel converter and control topology is proposed where a WFSM is capable of switching between multiple torque-speed profiles towards efficiency improvement. A novel converter and novel control topology are presented, demonstrating seamless transfer during online operation. The proposed methodology is verified through finite element analysis simulations. In the end, an overall performance analysis is also discussed between the two proposed topologies.

5.2 Modeling of Vehicle Dynamics and Drive Cycle Analysis

In an electric vehicle powertrain, the electric motor is the main component that produces propulsion force. Hence, the electric motor is responsible for producing enough tractive force to compensate for the vehicle mass, air drag, etc. Therefore, vehicle dynamics modeling provides important information about the tractive torque requirement at various speeds [1]. Below provided (5.1)-(5.6) represent various governing equations of vehicle dynamics [2], [5]. The vehicle acceleration can be expressed as shown below:

$$\frac{dV}{dt} = \frac{\sum F_t - \sum F_{tr}}{\delta M_v} \quad (5.1)$$

where V is the vehicle speed, F_t is the total tractive effort, F_{tr} is the total resistance, M_v is the total mass of the vehicle, and δ is the mass factor.

The dynamic equation of the vehicle along the longitudinal direction is given as:

$$M_v \frac{dv}{dt} = (F_{tf} - F_{tr}) - (F_{rf} + F_{rr} + F_w + F_g) \quad (5.2)$$

where dv/dt is the linear acceleration of the vehicle, F_{tf} and F_{tr} are the tractive efforts of the front and rear wheels, F_{rf} and F_{rr} are the rolling resistance of the front and rear wheels, F_w is the resistance of wind or aerodynamic drag, and F_g is the grading resistance. The front-wheel tractive effort is zero in a rear-wheel drive vehicle and vice versa.

As seen in equation (5.2), the resistance is mainly caused by three types of resistances, namely, rolling resistance, aerodynamic resistance, and grading resistance. The rolling resistance is mainly caused by the interaction of the tire and the surface. It varies in the change in the type of surfaces such as hard, soft, irregular surfaces, etc. The expression representing the rolling resistance is given in (5.3).

$$F_r = Pf_r \cos \alpha \quad (5.3)$$

$$f_r = 0.01 \left(1 + \frac{V}{100} \right) \quad (5.4)$$

where F_r is the rolling resistance, P is the normal load, f_r is the coefficient of friction, V is the velocity of the vehicle, and α is the angle is the gradient.

Equation (5.5) represents the resistance of air drag or aerodynamic resistance. This is mainly caused by two reasons: (i) vehicle shape: The interaction of vehicle shapes traveling at a certain velocity with respect to the opposing wind. The effect of the vehicle shape is defined as the aerodynamic drag coefficient (C_d), and it varies with the shape and size of the vehicle. (ii) skin friction: The speed of the wind close to the vehicle is almost the same as that of the vehicle. However, the wind far from the vehicle is still. Hence, skin friction is caused due to differences in the wind speed that is close to the vehicle from others. The direction of the wind component (V_w) and the density of the air (ρ) is also taken into consideration. However, V_s is considered to be zero.

$$F_w = \frac{1}{2} \rho A_f C_d (V + V_w)^2 \quad (5.5)$$

The grading resistance expression is given in the equation (5.6). Grading coefficient plays a major role when the vehicle is moving in uphill or downhill conditions. The component of vehicle weight during uphill or downhill conditions is always toward the ground. Hence, the force varies with the gradient of the slope.

$$F_g = M_v g \sin \alpha \quad (5.6)$$

where F_g is the gradient resistance, g is the acceleration due to gravity, α and is the gradient of the road.

In this thesis, Ford Fiesta vehicle specifications are used to model the vehicle dynamics as mentioned above. The specification of the vehicle is given in table 5.1.

TABLE 5.1
FORD FIESTA 2014 MODEL VEHICLE SPECIFICATIONS [1]

| Parameter | Value |
|---|--------------|
| Air Density (Kg/m ³) | 1.202 |
| Acceleration due to gravity (ms ⁻²) | 9.8 |
| Rolling coefficient | 0.013 |
| Drag coefficient | 0.33 |
| Frontal area (m ³) | 2.536 |
| Mass of vehicle (Kg) | 1570 |
| Radius of the wheel (m) | 0.3284 |
| Gear ratio | 6.25 |
| Transmission efficiency | 0.98 |
| Grading Angle (deg) | 3 |

With the developed vehicle dynamics model of the Ford Fiesta vehicle, the total tractive torque is calculated with the FTP75 drive cycle as the input. Fig. 5.1 [3], shows the federal test procedure (FTP75) drive cycle speed (rpm) vs time for this particular type of vehicle. This cycle covers a distance of 17.77 Km in a duration of 1874 seconds and with an average speed being 34.1 Km/h. This drive cycle is divided into three sections, namely, cold start, stabilized, and host start phases. Fig. 5.2 shows the total tractive torque required to be generated by the electric motor to run at the given FTP75 drive cycle profile.

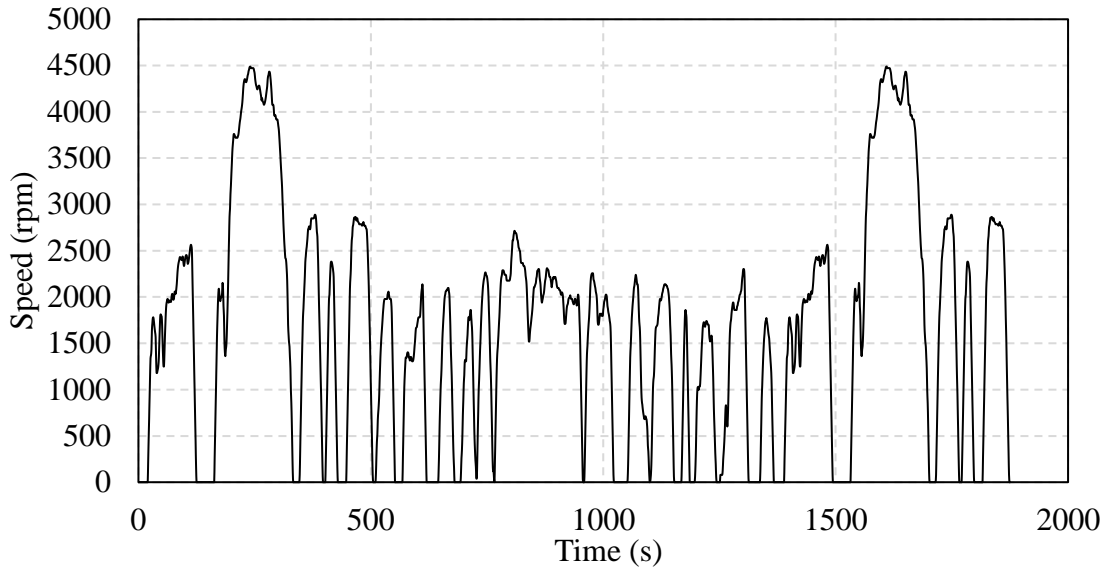


Fig. 5.1. FTP75 Drive cycle speed profile.

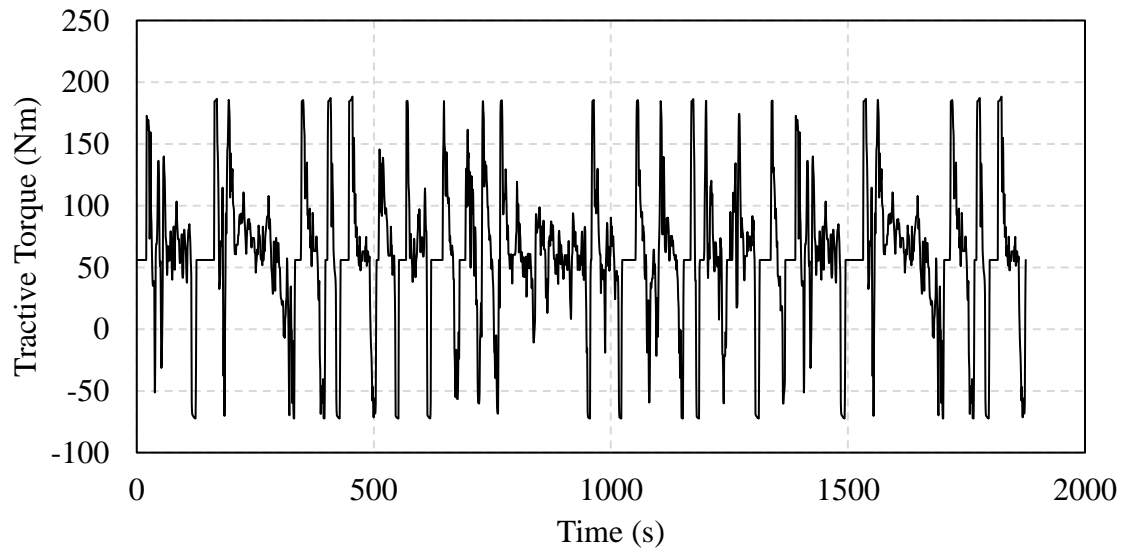


Fig. 5.2. Tractive torque required for FTP75 drive cycle.

5.3 Motivation from ETDs Performance Level

In the above section, a mathematical vehicle dynamics model has been developed, and the total tractive torque required is calculated for a given FTP75 drive cycle. Therefore, with the knowledge of vehicle dynamics corresponding to the mass of the vehicle, shape, wheel radius, maximum speed, etc., an electric motor and the powertrain for an electric vehicle are designed such that all the driving operating points lie under the torque-speed profile of the designed motor. Therefore, for a given electric motor, there exists a torque-

speed profile under which the electric motor operates according to the load. The operation under this torque-speed profile can be optimized as described in Chapter 4 with intelligent motor control algorithms. However, in everyday commutes, the operating condition might not always reach the maximum rated torque and speed the electric motor can deliver. Therefore, this chapter proposes a novel converter and novel control topologies for a doubly excited rotor configuration machine toward efficiency improvement.

5.4 Doubly Excited Rotor Configuration

In the wound field synchronous machine, there are separate windings for the stator and the rotor. Stator windings carry three-phase AC currents, and the rotor windings carry DC currents. The field winding on the rotor is wound in a series/parallel pattern such that the same winding goes into all the poles. There exists a pair of brushes and slip-rings assembly in the case of the conductive/brushed excitation system to pass the power from the rotor converter to the field winding. This thesis proposes a novel rotor winding configuration where a set of poles can be de-excited.

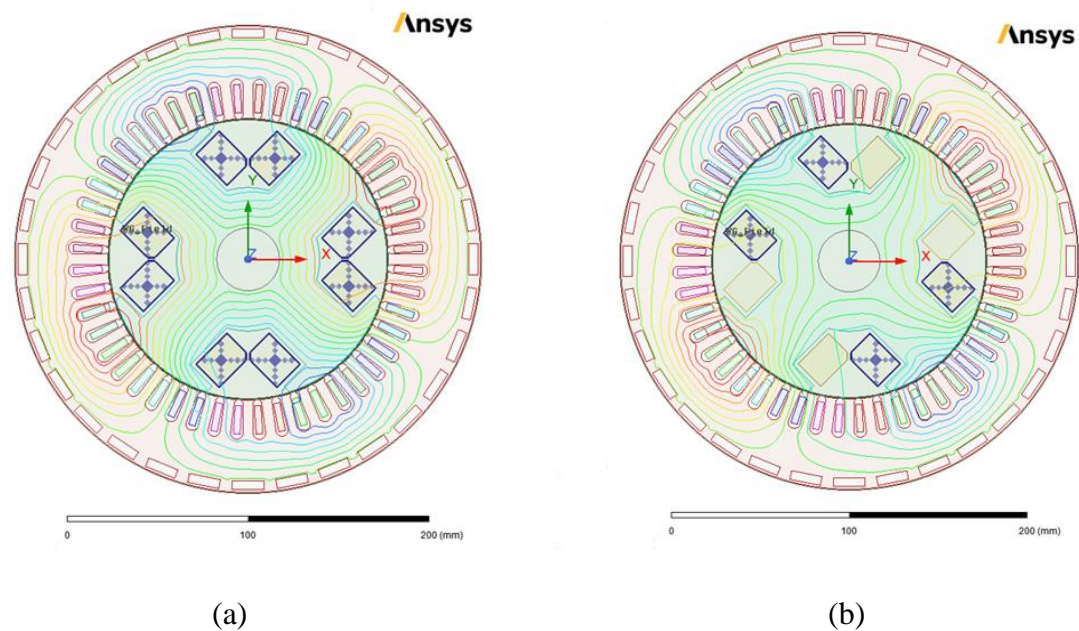


Fig. 5.3. Doubly excited rotor configuration. (a) Conventional rotor excitation with 4 poles. (b) De-excited rotor with 2 poles.

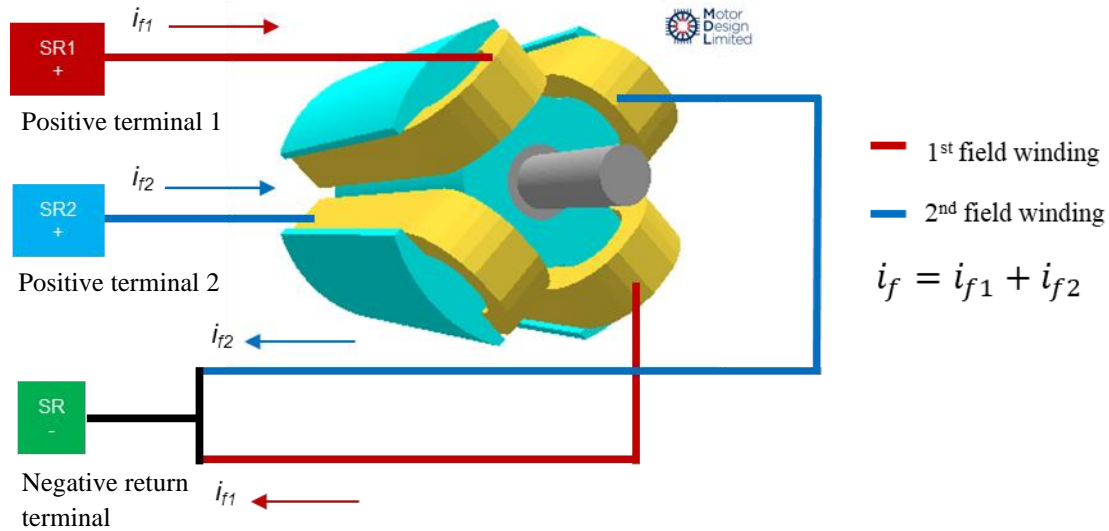


Fig. 5.4. Wound field synchronous machine with modified slip-ring assembly allowing selective rotor pole de-excitation.

The conventional wound field synchronous machine rotor is shown in Fig. 5.3 (a), where the shaded part shows the poles. As seen in the figure, in the first configuration, all four poles are excited through conventional brush and slip-ring assembly. Fig 5.3(b) shows the same machine with two poles de-excited, i.e., rotor windings only excite two of the poles. This de-excitation is not possible in the conventional design as there are fixed brushed and slip-rings assemblies. Therefore, this calls for a novel rotor winding configuration that allows selective rotor pole excitation. The rotor de-excitation strategy can be applied to any N-numbered pole WFSM while de-exciting any N-numbered poles. Depending on the number of poles of the WFSM, the design of the novel rotor winding configuration changes. This thesis focuses on a four-pole WFSM; hence only two of the rotor poles can be de-excited. The proposed novel rotor configuration design is shown in Fig. 5.4. As seen, there exist three sliprings (SR1+, SR2+, SR-) and three brushes assembly for transferring DC power to the rotor. The first pair of the rotor field winding is wound to two poles of the rotor. The path for the current in the first field winding is from SR1+ and SR-. The second pair of the rotor field winding is wound to the other two poles of the rotor. The path for the current in the second field winding is from SR2+ and SR-. It is to be noted that the return current path for both the field windings is SR-. The proposed

novel rotor winding configuration allows the motor control to selectively excite the rotor windings with the separate slip-rings assembly.

5.5 Proposed Converter Topology

With respect to the above-mentioned rotor configuration, there needs to be a converter that accommodates three sliprings and brush assembly for excitation and de-excitation. The conventional rotor excitation converters cannot be used as there exists only one pair of sliprings and brush assembly. Therefore, this thesis proposes two rotor excitation configurations topologies allowing selective rotor de-excitation control for WFSM, namely: (i) single-legged converter, and (ii) double-legged converter. The converter topology, voltage-current waveforms, and losses are discussed in the later subsections.

5.5.1 Single-Legged Converter Topology

This type of converter is similar to the conventional buck converter that is used to excite brushed/conductive excited WFSM. However, in the proposed topology, there exist two field windings going to the rotor poles separately from the mid-point of the converter leg through separate sliprings. As seen in Fig. 5.5, the first and second field windings are excited through the slip-rings pairs SR1+, SR- and SR2+, SR-.

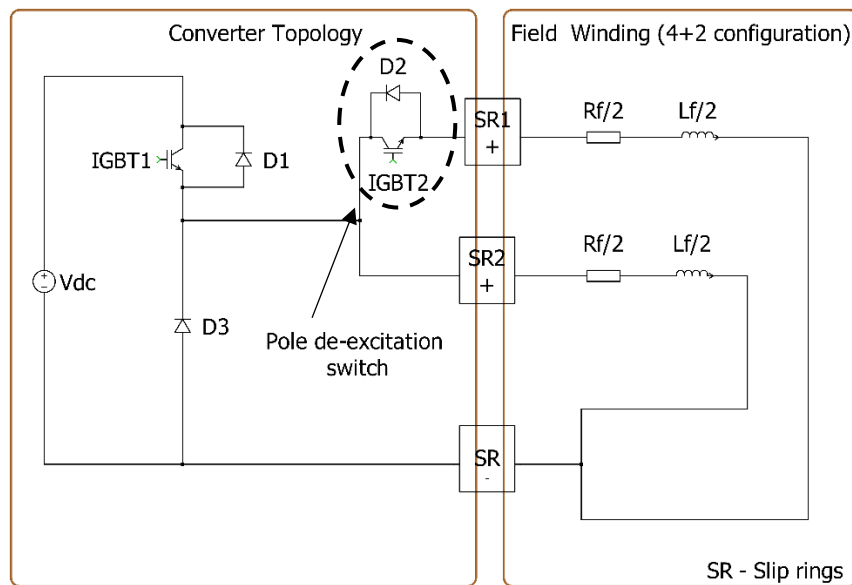


Fig. 5.5. Single-legged converter circuit topology.

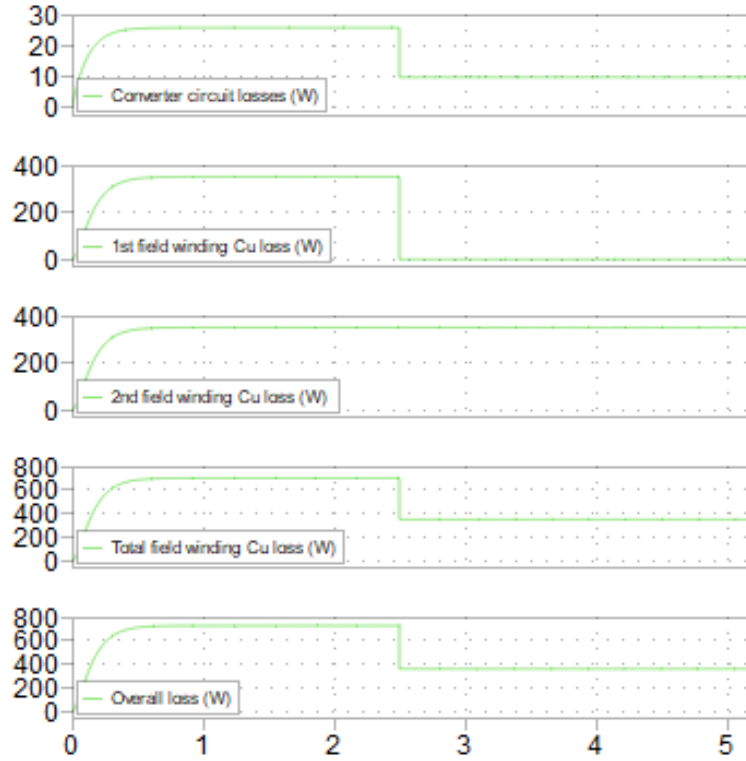


Fig. 5.6. Detailed Loss analysis of single-legged converter topology.

The field winding resistance and inductance of both the separate field windings are $R_f/2$ Ohm, and $L_f/2$ H since only half of the entire field windings are now wound to two separate pairs of rotor poles, as shown in Fig. 5.4. An extra IGBT, namely pole de-excitation switch is present on the first field winding. This extra switch controls the flow of rotor current into the field windings. The pole de-excitation switch is turned ON for four pole operations, and it is turned OFF for two pole operations. Since both the separate field windings are connected to a common mid-point on the converter leg, the IGBT carries twice the amount of original field current. Hence, the IGBT converter losses are doubled during the four-pole configuration. Fig. 5.6 shows the loss analysis of the proposed converter. The converter is initially operated in a four-pole mode and switched to a two-pole mode at $t=2.5$ sec. The algorithm that controls the switching of the pole de-excitation switch according to the torque-speed load point, will be discussed in the later section. During the four-pole operation of the converter, the converter losses and field winding copper losses are more compared to the converter operating in the two-pole configuration.

5.5.2 Double-Legged Converter Topology

As the name suggests, this type of converter has two legs with IGBTs and anti-parallel diodes. The two separate field windings going to the separate sets of rotor poles are connected to the mid-points of both the legs through SR1+ and SR2+ sliprings, as shown in Fig. 5.7. Similar to the single-legged converter, there exist three sliprings and three brush assembly in double-legged converter as well. The path for the field excitation current in the first and second field windings are through the pairs, SR1+, SR- and SR2+, SR-, respectively. The field winding resistance and inductance are $R_f/2$ Ohm, and $L_f/2$ H due to above discussed reason in the single-legged converter. The main difference in this type of converter is that there is no pole de-excitation switch present. Instead, there exists a separate additional leg sharing the same DC bus. For the four-pole configuration, both the field winding conducts current through separate legs. For the two-pole configuration, only one of the field windings conducts current while the second field winding remains OFF. However, in this type of converter, there exists an additional anti-parallel diode compared to the single-legged converter.

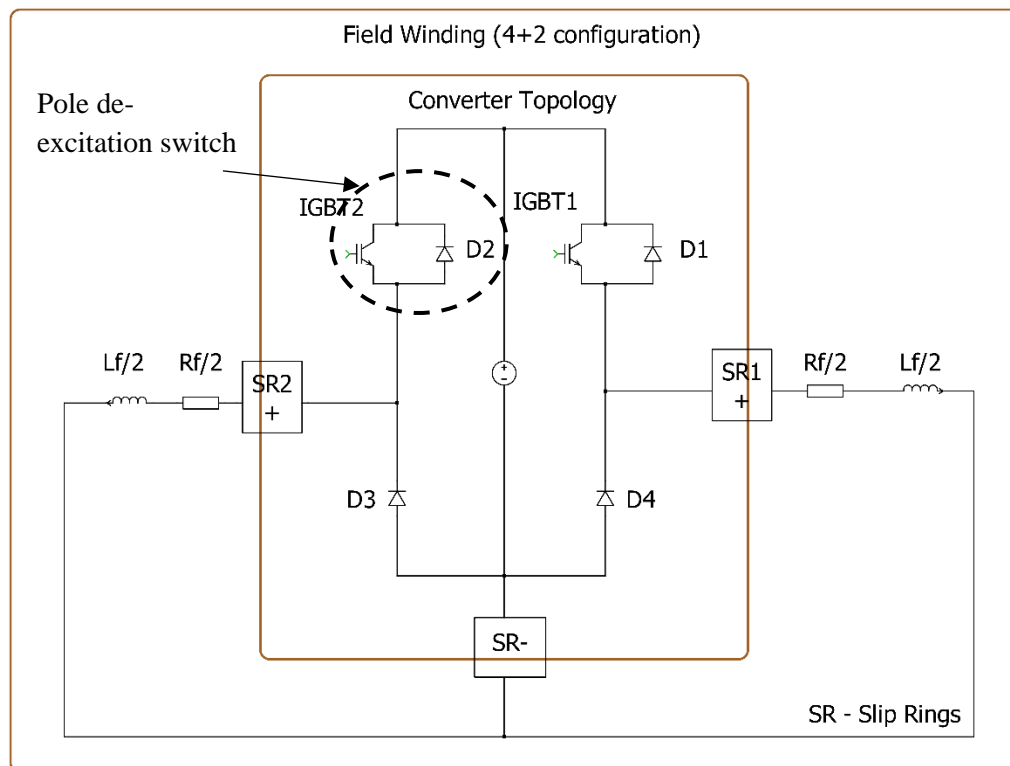


Fig. 5.7. Double-legged converter circuit topology.

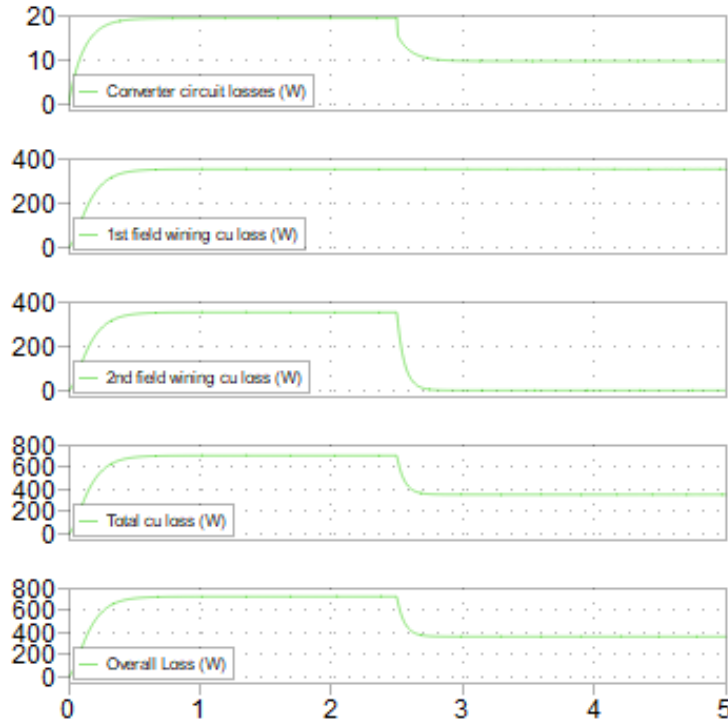


Fig. 5.8. Detailed Loss analysis of double-legged converter topology.

The converter losses are doubled during the four-pole operation, and the losses reduce eventually during the two poles operation. This is because only one of the two legs is functioning during the two-pole operation when compared to the four-pole configuration. This holds the same in the case of the field winding copper losses too. The field winding copper losses are double under the four-pole configuration and because halved during the two-pole operation. This is due to only one of the separate field windings conducting out of two field winding conductors. In detail, converter and field winding copper loss comparison among the proposed topologies are discussed in the next section.

5.5.3 Overall Performance Analysis Among the Proposed Topologies

Below shown Table 5.2 shows the in-detail comparison and discussion between the conventional, single-legged, and double-legged converters. Comparisons in the number of IGBTs, diodes, sliprings, and brushes, along with the converters and the field winding copper losses, are discussed for both the four-pole and two-pole configurations, respectively. The conventional converter topology is shown in Fig. 5.9 for comparison. From the various comparison, the following conclusions are drawn:

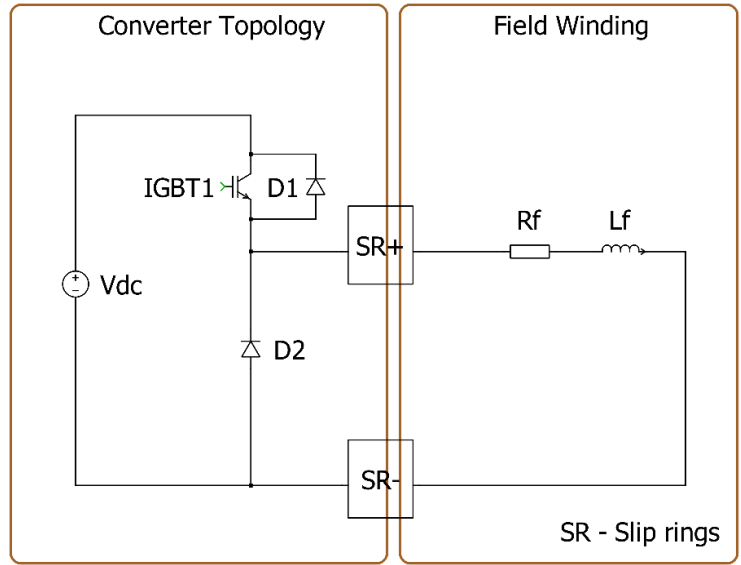


Fig. 5.9. Conventional conductive/brushed rotor excitation converter topology.

TABLE 5.2
OVERALL PERFORMANCE COMPARISON OF CONVERTER TOPOLOGIES AND LOSSES

| Topology | | Conventional Converter | Single-Legged Converter | Double-Legged Converter |
|-----------------------------|----------------|------------------------|--------------------------|--------------------------|
| Sliprings | | 2 | 3 | 3 |
| Brushes | | 2 | 3 | 3 |
| IGBT(s) | | 1 x (10 A) | 1 x (10 A) 1 x (20 A) | 1 x (10 A) 1 x (10 A) |
| Diode(s) | | 1 | 1 | 2 |
| Converter Losses (W) | 4 Pole | 9.3 | 25.67 | 19.24 |
| | 2 Poles | | 9.62 | 9.62 |
| Field Cu Losses (W) | 4 Pole | 700.1 | 700.4 | 700.4 |
| | 2 Poles | | 350.2 | 350.2 |
| Total Losses (W) | 4 Pole | 709.4 | 726.07 | 719.64 |
| | 2 Poles | | 359.82 | 359.82 |

- Additional sliprings and brush assembly are required for both single- and double-legged converters.

- The number of IGBTs is more in both the proposed topologies compared to the conventional converter. However, single-legged converters need a higher current-rated IGBT as it carries double the rated field winding current.
- The number of diodes is more in the double-legged converter compared to other types.
- Converter losses are always lower in the two-pole configuration compared to the four-pole configuration. It is observed that the single-legged converter has more converter losses as the IGBT carries double the rated field winding current.
- Field winding copper losses are the same for both the proposed converter as only one of the two separate fields winding carries current in the two-pole configuration.
- The overall losses in both the proposed converters in two-pole configurations are the same. However, during the four-pole configuration, the single-legged converter tends to have more overall losses.
- The single-legged converter is more economical compared to the double-legged converter. However, the double-legged converter tends to have lower overall losses.

5.6 Proposed Control Algorithm and Analysis of Seamless Transfer Between Multiple Torque-Speed Characteristics

5.6.1 Efficiency Map Generation for Offline Look-Up Tables

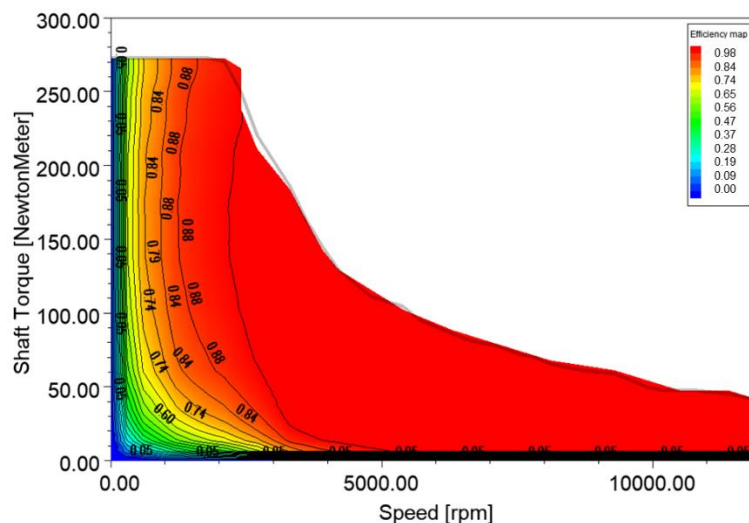


Fig. 5.10. Torque-speed and efficiency profiles for conventional WFSM.

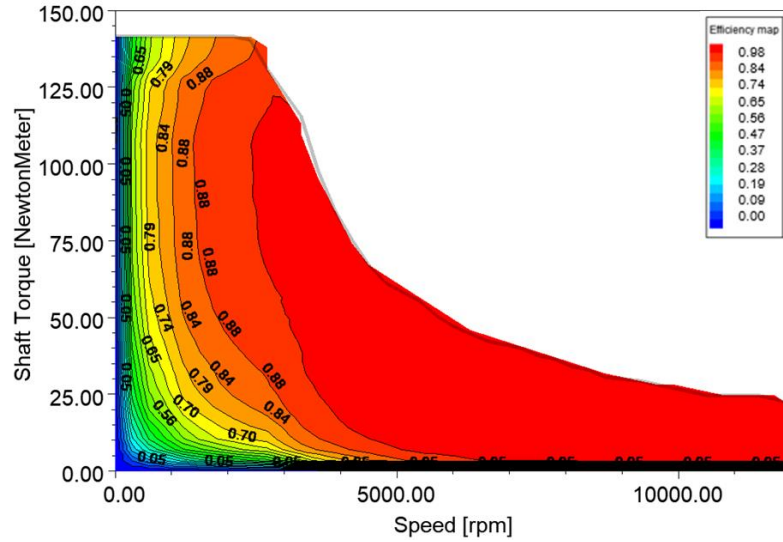


Fig. 5.11. Torque-speed and efficiency profiles for de-excited rotor WFSM.

As mentioned in the previous section, two WFSM FEA models, as shown in Fig. 5.3, are used to generate the torque-speed profiles. The conventional WFSM torque-speed profile, as seen in Fig. 5.10, has a maximum peak torque of 270 Nm and a base speed of 2,200 rpm. These simulations are run at a base speed on 325 V DC bus voltage. The de-excited WFSM has two poles de-excited, i.e., only two pairs of the rotor poles are excited, as shown in Fig. 5.3(b). As the rotor flux decreased because of the de-excitation, the maximum peak torque is decreased to 140 Nm, and the base speed remains the same as that of conventional WFSM as shown in Fig. 5.11. It is worthwhile to note that in the second case of rotor de-excitation, even if two poles out of four are de-excited, the WFSM does not completely behave as a two-pole WFSM. This is because the rotor's non-salient poles still provide a low reluctance path for the flux lines to complete a closed loop. Hence, a fringe amount of flux lines passes into the non-excited rotor poles' core and indirectly form a four-pole operation. During this operation, the rotor flux is greatly reduced, and this causes in reduction of core losses. This, in return, is beneficial as seen in terms of overall efficiency. Therefore, an intelligent novel motor control algorithm is required to switch between conventional and the proposed rotor winding configuration depending upon torque-speed load points. The novel control algorithm and efficiency improvement is discussed in the next section.

5.6.2 Proposed Control Algorithm for Seamless Transfer

Figure. 5.12 shows the flowchart of the novel proposed control algorithm. This algorithm controls the pole de-excitation switch in the single-legged converter and the IGBT2 in the double-legged converter. The novel control algorithm intelligently decides and switches between the configurations according to the load point. For a given WFSM, initially, offline FEA torque-speed and efficiency maps are generated in both conventional and de-excited rotor modes. This is very useful for the control algorithm to develop and implement a truth table based on the overall efficiency, maximum and base speeds of both the generated maps. The control algorithm compares the load torque and speed load points during the online operation and switches the control to rotor de-excitation mode if the efficiency in the two-pole mode is more than that of four-pole mode. If not, the control algorithm remains in the conventional four-pole configuration.

Figure. 5.13. shows the difference in the efficiencies between the conventional and the rotor de-excitation configurations. Efficiencies improvement ranging to 12% is seen under 100 Nm and the base speed. The improvement in efficiency is mainly contributed by the decrease in the core losses in the two-pole configuration.

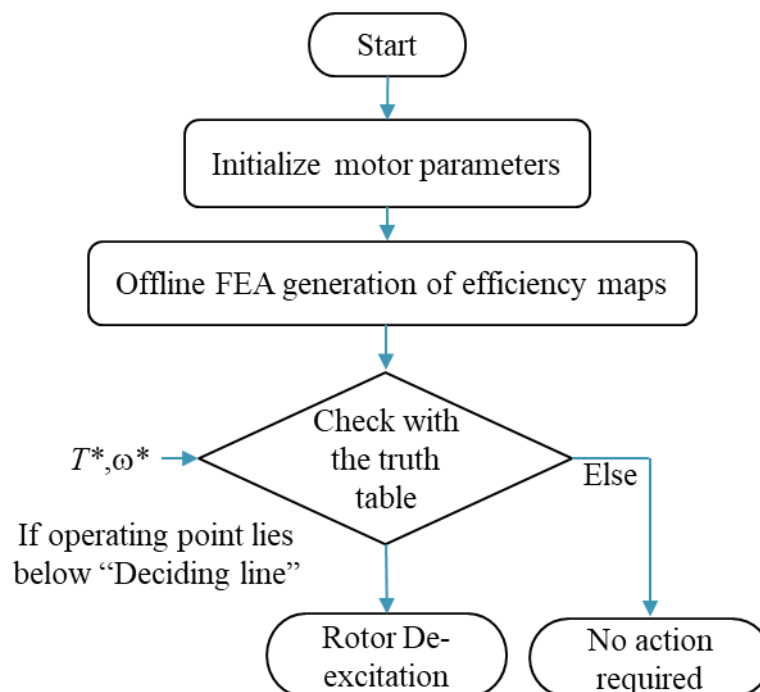


Fig. 5.12. Flowchart of the proposed control strategy for rotor de-excitation.

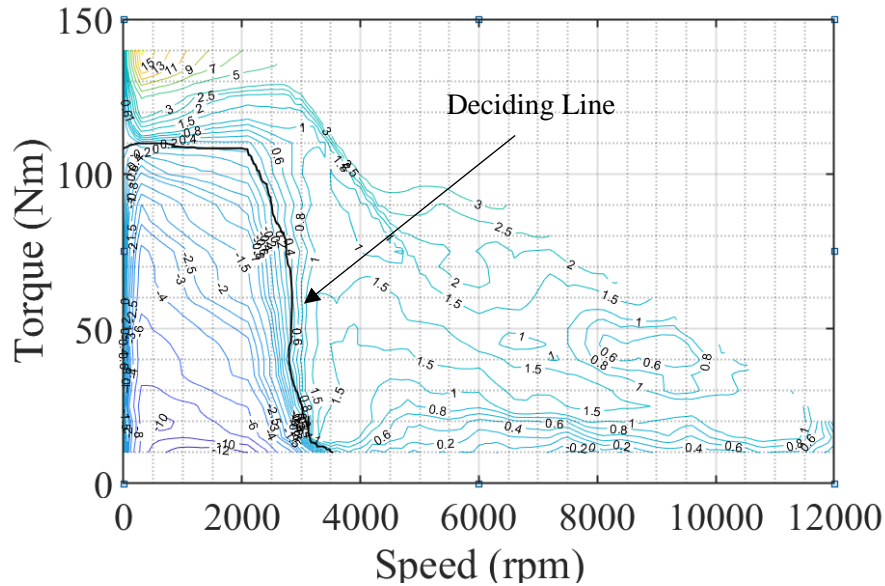


Fig. 5.13. Comparison of efficiencies in conventional and de-excited rotor configuration.

5.7 Conclusion

In this chapter, firstly, mathematical modeling of vehicle dynamics is developed and simulated to demonstrate the amount of tractive torque required for the vehicle to achieve a certain amount of drive cycle speed. Following the modeling, the motivation behind this chapter is briefly discussed in ETD's overall performance level. Then, two novel rotor excitation converter topologies are proposed for the rotor de-excitation configuration. It is seen that the single-legged converter is more economical compared to the double-legged converter. However, the double-legged converter is more economical compared to the single-legged converter. A novel control strategy is proposed in Section 5.6, and improvement in efficiencies is shown in Section 5.6.2.

5.8 Reference

- [1] Korta, Philip, "Multi-Objective Drive-Cycle Based Design Optimization of Permanent Magnet Synchronous Machines," (2018). *Electronic Theses and Dissertations*. 7535.
- [2] M. Ehsani, Y. Gao, S. E. Gay, and A. Emadi, *Modern Electric, Hybrid Electric, and Fuel Cell Vehicles*. NY, USA: CRC Press, 2004.

[3] EPA. (2022, Jan.). EPA Federal Test Procedure, [Online]. Available: <https://www.epa.gov/emission-standards-reference-guide/epa-federal-test-procedure-ftp>

CHAPTER 6

CONCLUSION AND FUTURE WORK

6.1 Conclusion

This thesis proposed a maximum overall system efficiency per ampere control for WFSM drives. The main objective of the thesis and the proposed control algorithm is towards improving energy efficiency of the electric vehicle. A brief summary of all the chapters is presented below.

Chapter 1 presents the current trend and soaring electric vehicles and its part manufacturing OEMs, mainly in Canada and across the world. This chapter also highlights the importance of transitioning from ICE vehicles to EV's. At the end of the chapter, the motivation, research objective, and contributions are outlined.

Chapter 2 introduces the mathematical modeling of WFSM, stator three-phase VSI inverters, various rotor excitation converters, and also extends modeling to calculate losses of various developed mathematical models. The simulation results of the inverter and the converter are presented.

Chapter 3 demonstrates the designing of the control of proportional-integral controllers for closed-loop current and speed control of WFSM. A comparison is made between conventional total- and rotor- loss minimization control methods. A maximum overall system efficiency per ampere control algorithm is proposed using brute-force algorithm. The performance is then compared to the conventional MTPA. From the comparison between the MTPA and the proposed algorithm, a significant amount of loss reduction is seen in the lower torque regions. This is because of the difference in the current distribution among the control methods.

Chapter 4 extends the work of Chapters 2 and 3 towards the implementation and validation of developed closed-loop controls. This includes building the required test rig using a real-time embedded controller, designing and experimental validation. The difference between simulation and experimental results is investigated.

Chapter 5 proposes a novel converter and control topology for a doubly excited wound field synchronous machine towards improving efficiency through rotor de-excitation. Two novel converter topologies are proposed, and an overall performance comparison among the proposed converters are shown. Finite element analysis results are shown, supporting the proposed method and topologies.

6.2 Future Work

The research work presented in this thesis can be extended to the following future work topics as shown below:

- The maximum overall system efficiency per ampere control can be extended by including losses of mechanical powertrain and chassis. A drive-cycle analysis is to be studied to investigate the advantages of the control algorithm during transients.
- Experimental prototyping of the proposed converter topologies in Chapter 5 to validate the converter and controls on the doubly excited wound field synchronous machine.

VITA AUCTORIS

NAME: Vamsi Krishna Kurramsetty

PLACE OF BIRTH: Chennai, Tamil Nadu, India

YEAR OF BIRTH: 1999

EDUCATION: Bachelor of Electrical and Electronics
Engineering - SASTRA Deemed University,
Thanjavur, India, 2020.

Sri Chaitanya Junior College, Vijayawada,
India, 2016.

Ratnam Gen Next School, Tirupati, India, 2014.

ProQuest Number: 30247606

INFORMATION TO ALL USERS

The quality and completeness of this reproduction is dependent on the quality and completeness of the copy made available to ProQuest.



Distributed by ProQuest LLC (2023).

Copyright of the Dissertation is held by the Author unless otherwise noted.

This work may be used in accordance with the terms of the Creative Commons license or other rights statement, as indicated in the copyright statement or in the metadata associated with this work. Unless otherwise specified in the copyright statement or the metadata, all rights are reserved by the copyright holder.

This work is protected against unauthorized copying under Title 17, United States Code and other applicable copyright laws.

Microform Edition where available © ProQuest LLC. No reproduction or digitization of the Microform Edition is authorized without permission of ProQuest LLC.

ProQuest LLC
789 East Eisenhower Parkway
P.O. Box 1346
Ann Arbor, MI 48106 - 1346 USA